Design and Implementation of a Rotary Fast Tool Servo for a Turning Machine

by

David Chih-Yan Ma

S.B., Massachusetts Institute of Technology (1996)

Submitted to the Department of Mechanical Engineering
in partial fulfillment of the requirements for the degree of

Master of Science in Mechanical Engineering

at the

MASSACHUSETTS INSTITUTE OF TECHNOLOGY

June 1998

Author .....
Department of Mechanical Engineering
May 8, 1998

Certified by .....
David L. Trumper
Rockwell International Associate Professor of Mechanical Engineering
Thesis Supervisor

Accepted by .....
Ain A. Sonin
Chairman, Department Committee on Graduate Students

Design and Implementation of a Rotary Fast Tool Servo for a Turning Machine

by

David Chih-Yan Ma

Submitted to the Department of Mechanical Engineering
on May 8, 1998, in partial fulfillment of the
requirements for the degree of
Master of Science in Mechanical Engineering

Abstract

In this thesis we describe the design and implementation of a rotary fast tool servo (RFTS) in a machine tool for turning ophthalmic lenses. To machine nonrotationally symmetric lenses, the cutting tool on the RFTS must move synchronously with the spindle rotation. Therefore, to cut a lens at high spindle speeds, the cutting tool must be capable of extremely high accelerations. In our design we mount the cutting tool at the end of a rotary arm. This allows us to achieve higher accelerations and lower vibrations than conventional fast tool servos. This thesis describes the development of the RFTS, including component selection and testing. We also detail the design and fabrication of the RFTS that is installed in a prototype turning machine.

Thesis Supervisor: David L. Trumper
Title: Rockwell International Associate Professor of Mechanical Engineering

Acknowledgments

I would like to thank Professor David Trumper for his guidance and support as my academic and research advisor these past five years. I have learned a great deal in his lab, because he has always given me the freedom to explore the parts of the project that have interested me the most. While at the same time, talking to him has always helped me see what parts of the project were the most important. I would also like to thank the Ph.D student on the project, Steve Ludwick. He was always willing to help me troubleshoot and his advice was always timely. He also very generously allowed me to work on some of the most interesting and exciting aspects of the project.

The other members of the project were also very helpful. With Dave Chargin, we built a box to stand the test of time. Yuka Miyake was always willing to lend a hand in whatever the project required. My Precision Motion Control labmates Mike Liebman, Robin Ritter, Pradeep Subrahmanyan, Paul Konkola, Sai-Bun Wong, Stephanie Gellar, Ming-Cheh Wang, and Natasha Chang helped create an atmosphere of mutual respect in the lab that was great to work in and I could always count on them for assistance.

Our administrative assistant, Maureen Lynch, helped everything run smoothly and provided wonderful food for hungry graduate students. From Fred Cote and the machine shop staff, I gained machine shop experience which served me well while designing parts for the project. When I look back, I am sure I will be even more grateful to have had hands on work this past two years. Professor Alex Slocum gave us some very sound advice about designing the rotary fast tool servo axis, which put us on the right track. Professor Tom Kurfess and his students at Georgia Tech have a long history in using Coordinate Measuring Machines for metrology. They helped confirm our measurements of the form error in the lenses, in Chapter 4. We also thank MicroE for their donation of a high-resolution laser encoder.

Finally and gratefully, I would like to thank my family and friends. My parents are responsible for a large part of who I am today. Good and bad, what they gave me allowed me to survive six years at MIT. Thanks Mom and Dad. Throughout my

undergraduate and graduate years, both my sister and I have changed, matured, and become accustomed to seeing each other infrequently. But her support has remained solid. Thanks Diana.

Each of my fondest memories at MIT has certain friends associated with them. These memories are how I will remember my time here. Thank you all.

Contents

List of Figures

List of Tables

Chapter 1

Introduction

The focus of this thesis is the design and implementation of a Rotary Fast Tool Servo (RFTS) axis for diamond turning of nonrotationally symmetric ophthalmic lenses. Over the last two years, we have built a novel prototype turning machine which places the cutting tool at the end of a rotating arm. A single point cutter on a rotary axis has several advantages over a conventional linear axis design. First, it permits much higher tool accelerations than previous ophthalmic lens turning machines. Second, reaction forces from accelerating the tool are kept low because the rotary inertia of the tool arm is low relative to the rest of the machine. Third, the axis is also a direct-drive system and is simpler to control because its dynamics are cleaner than a tool driven by a linear mechanism such as a ball screw. The research has taken place in Professor David Trumper's Precision Motion Control Laboratory at the Massachussets Institute of Technology, from the fall of 1997 to the spring of 1998. The research group also includes Stephen Ludwick, a Ph.D student at MIT, David Chargin, a S.M. student at MIT, and Yuka Miyake, an undergraduate student. The design and implementation of the RFTS axis has been a two-stage process. The first stage was to build a testbed that allowed us to test the performance of individual elements. In the second stage, we used the experience gained from building the testbed to design the RFTS axis for the prototype machine. A large portion of this thesis describes the criteria used for selecting the components during the design phase of the RFTS axis, along with the procedures for testing the hardware.

1.1 Motivation for the Research

Current methods for manufacturing ophthalmic lenses include grinding, turning, and milling. An overview of conventional lens manufacturing techniques is provided in [11] and [19]. Regardless of the specific process, all of the current manufacturing processes do not directly produce lenses that meet the required surface finish and form accuracy specifications. Therefore, all of the lenses undergo a lapping process to reach an optically clear surface finish and to reduce form error. The lapping procedure is a multi-stage process. In the first stages of the lapping process, water is injected between the cut lens and a hard lap with an abrasive pad. The hard lap, which is premachined to have the inverse shape of the lens's desired shape, and the lens are then oscillated with respect to one another to remove machining errors. These first stages remove approximately 150 μm of material. The final stages use a felt pad between the hard lap and the lens. This lapping process imparts the required surface finish, removing approximately 10 - 50 μm of material.

However, the lapping process itself may introduce form errors into the lenses. This is especially true of toric lenses, which are nonrotationally symmetric. An example of a toric lens is shown in Figure 1-1. When lapping lenses with nonspherical contours, material is inaccurately removed. This is because the geometric surface imparted by the relative motion of the lap and the lens does not match the lens's desired contour. Another disadvantage of the process is that a different hard lap is required for each possible lens prescription. This requires making, maintaining, and storing of thousands of laps at every production facility.

Ideally, a machining process would produce a lens with small enough form error to eliminate the need for a hard lap. The first advantage of such a machine would be to also eliminate storing and maintaining the hard laps, which would reduce the cost and size of the operation. In addition, any improvement in the lens's form error and surface finish during the initial machining reduces process time. Finally, lenses could be produced more accurately by avoiding the nondeterministic lapping process.

In considering the three manufacturing processes mentioned above, grinding is

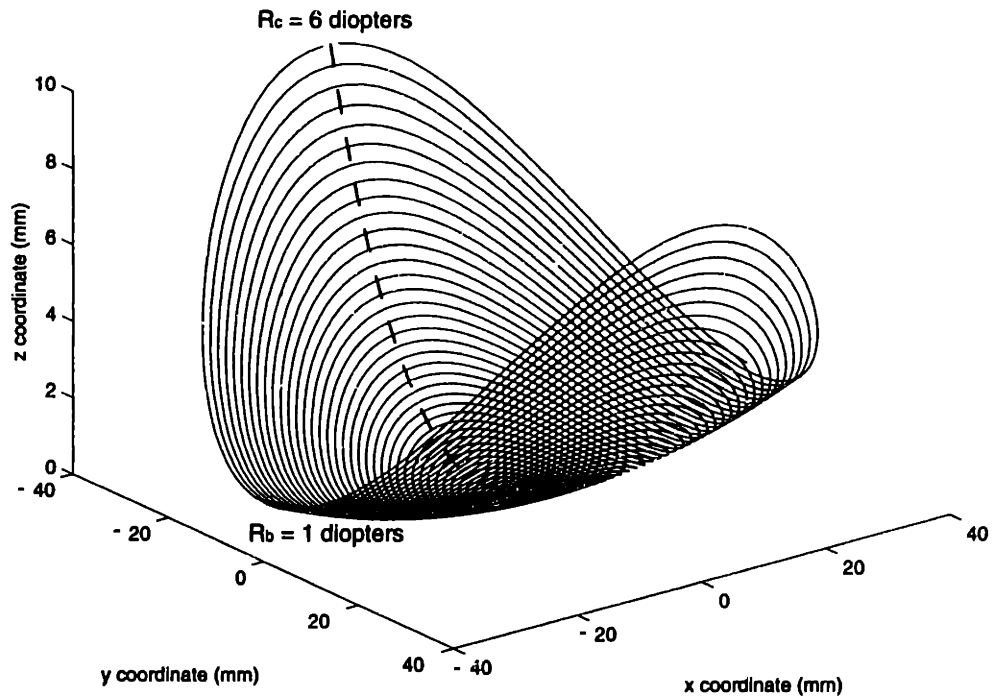

Figure 1-1: Contour of a toric lens.

usually feasible only for glass lenses. Currently, most of the ophthalmic industry has moved to using plastics such as CR39 and polycarbonate for making lenses. Of the two remaining processes, milling and turning, we decided to focus on turning for the new design. Theoretically, single point turning should produce a better surface finish and give better contouring accuracy than milling. Turning ophthalmic lenses is especially challenging because nonrotationally symmetric lenses need to be machined. This requires a fast axis with high bandwidth, often called a fast tool servo (FTS). The challenge in designing the FTS is that the axis's motion is required to be synchronous with spindle position [4]. Therefore, turning at high spindle speeds requires high accelerations from the FTS.

A picture of a lens turning machine is shown in Figure 1-2. Turning ophthalmic lenses requires three servo-controlled axes, a spindle, a cross slide, and a fast tool servo. The axes are laid out in a T configuration with the spindle mounted on a cross slide. In the picture, the spindle is bolted onto a carriage traveling on linear

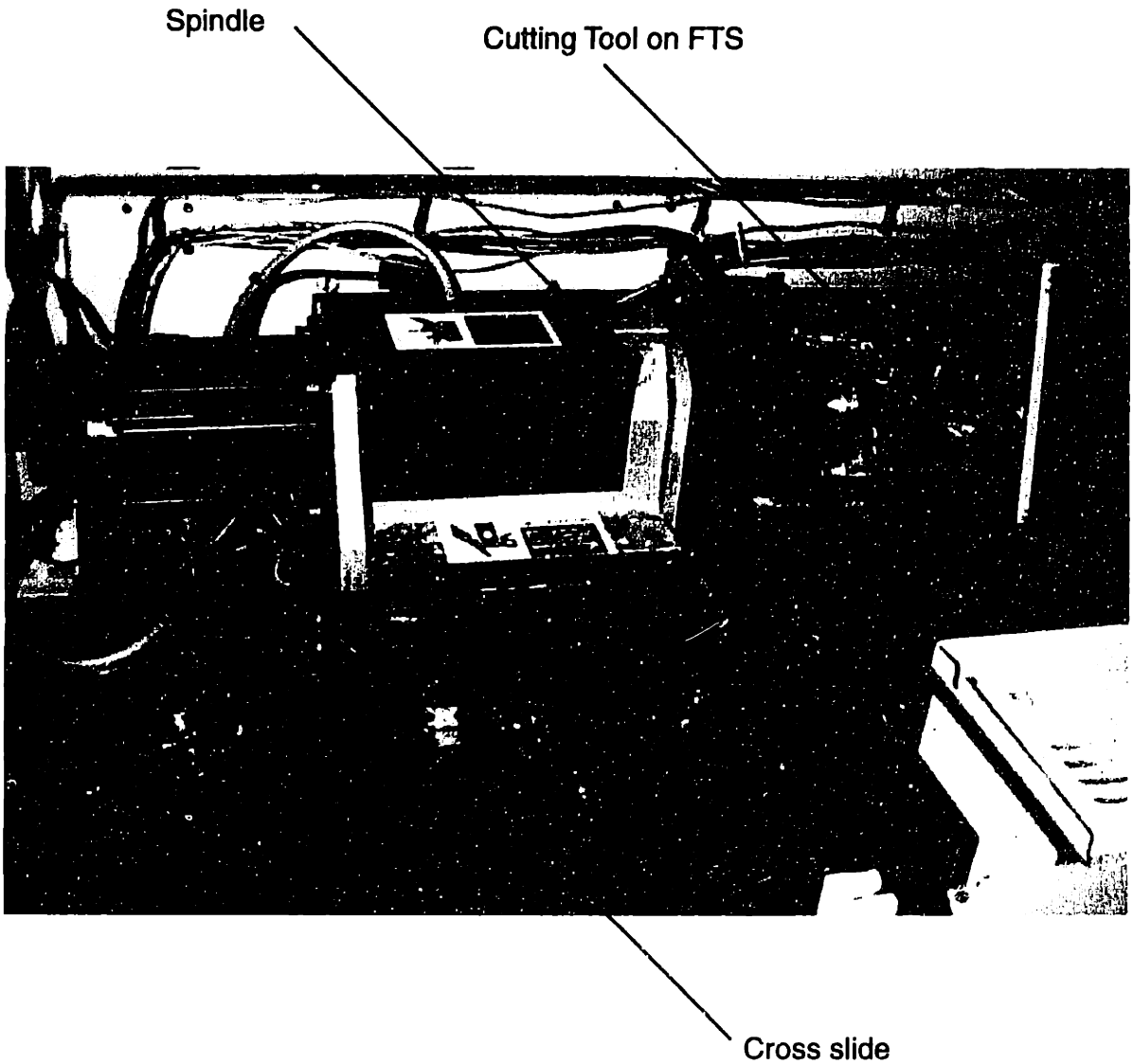

Figure 1-2: Picture of a Diamond Turning Machine.

guides, which is driven by a motor and ball screw. As in any turning operation, the spindle holds the workpiece, a plastic lens blank. The purpose of the cross slide is to move the spindle such that the cutting tool on the fast tool servo axis can cut along the face of the workpiece. The fast axis, which contours the lens, is another carriage riding on linear guides, driven by a ball screw and motor. A cutting tool is mounted on the front of the carriage. In the case of a linear FTS axis, the cross slide moves the spindle in a direction that is orthogonal with respect to the motion of the FTS.

A fast axis is an essential requirement for turning nonrotationally symmetric parts. For lenses that are spherical and rotationally symmetric, the contour height of the lens z depends only on the radial position r on the lens. However, for a toric surface the contour height z depends on r and the angular position θ, as shown Figure 1-1. Thus, the position of the cutting tool has to be synchronized to θ. As the tool cuts the lens, it oscillates with a fundamental frequency that is twice the spindle frequency. As an example, for a spindle speed of 3000 RPM, the tool oscillates at a fundamental frequency of 100 Hz. This high frequency trajectory leads to high acceleration requirements on the FTS.

There are many prior instances of using diamond turning to accurately turn optics. Among the most notable are the DTM's developed at Lawrence Livermore National Laboratory, including the LODTM and the BODTM, which machine mirrors for telescope optics [6] [20]. However, these machines target a different area of interest than our research. The LODTM has a machining accuracy of 28 nm (1.1 microinches), whereas our desired accuracies are on the order of 1 μm. Although not needed to achieve those accuracies, the high bandwidth FTS developed for the LODTM is a piezoelectric actuator. Its range of motion is $\pm$ 2.5 μm ($\pm$100 microinches). However, to turn ophthalmic lenses a FTS must have a range of approximately 20 to 30 mm. Closer to our particular application is the turning of contact lenses. For example, Rank Pneumo also uses a piezoelectric FTS, with a range of $\pm$0.2 mm, to turn contact lenses [4]. The common theme for these piezoelectric actuators is that they have high stiffnesses and high natural frequencies, which allow them to attain high bandwidths. At the same time, they also suffer from limited travel capabilities. If a longer range of

travel is desired, then another type of actuator has to be employed. Another example of a FTS is one designed at the Frauhofer-Institut fur Produktionstechnologie, IPT, in Aachen, Germany [23]. The fast tool servo is driven by a linear motor traveling on air bearings. The carriage mass is only 0.65 kg and is kept low by using synthetic fiber for the frame. It has a travel of 1.6 mm, an acceleration capability of 45 g, and servo bandwidth of 100 Hz. However, at that acceleration the reaction forces from the tool's acceleration become very significant, and leads to significant vibration in the machine base.

1.1.1 Design Parameters of our New Machine

The requirements of the new machine are that it should be able to:

1. Cut blanks up to 100 mm in diameter and 30 mm thick.
2. Form a toric surface described by,

$$z(x,y) = R_b - \sqrt{[R_b - R_c + \sqrt{(R_c^2 - y^2)}]^2 - x^2}, \tag{1.1}$$

where, $R_b = 26.5$ mm, $R_c = 17.6$ mm, and $x^2 + y^2 \leq 2500$ mm^2

3. Achieve a form accuracy of 1 μm over 10 mm of the toric surface described by the second requirement.
4. Achieve a surface roughness of $R_q = 0.2$ to 0.3 μm.
5. Cut the blank in less than 1 minute.
6. Have a tool cost to prepare each lens of less than \$ 0.02 per lens.

When designing the RFTS, several strategies to actuate the fast axis are possible [14]. A typical fast tool servo is driven by a mechanism such as a ball screw. Another option is a direct-drive fast axis in which the tool is driven directly by an actuator such as a linear motor. The advantage of the ball screw is that it is an established technology and inherently provides stiffness to the axis. However, it also complicates the dynamics of the system, which is now a mass being driven through a spring, representing the compliances of the bearings, the ball screw, the ball nut. The result is that the system may have a low resonant frequency that limits the bandwidth of

the fast axis. The advantage of a direct-drive axis is that it is cleaner dynamically, eliminating the mass-spring system. We would also eliminate the flexing of the ball screw, stiction in the mechanism, and the noise due to the recirculating balls in the nut. However, in going to a direct-drive solution, we would lose the stiffness inherently provided by the ball screw and must then rely on the servo loop to provide all the stiffness and disturbance rejection in the drive.

Another design consideration is whether to make a rotary fast tool servo or a linear fast tool servo. The machine described previously is an example of a linear fast tool servo. Whether driving a mechanism or directly driving the load, the motor has to move a carriage with significant mass. This severely limits the acceleration because of the amount of force the motor has to exert to accelerate the carriage. Also, the acceleration rating for most rolling element linear bearings is limited to 5 g. If we instead mount the tool on an arm driven by a rotary motor, most of the mass is placed near the axis of rotation. Now, the arm is lightest at the arm tip, where the high tangential accelerations are required. Also, the ratio of the carriage mass to machine mass is much greater than the ratio of the rotary inertia of the arm to the rotary inertia of the machine. This is because rotary inertia increases as the fourth power of radius of the rotating element. Therefore, reaction forces due to the tool's acceleration are also decreased, thereby decreasing the vibration of the machine during operation.

The drawback of the rotary actuator is that we must carefully design the cantilevered arm to be stiff as well as low in inertia. In addition, metrology is more difficult for the rotary axis. The essential angular position to be measured is the angular position of the tool mounted on the tip of the arm. However, for ease of mounting and to minimize the rotary inertia of the sensor, the sensor is most conveniently placed in line with the tool arm shaft. Therefore, we are actually measuring the rotation of the tool arm shaft, whose angular position does not necessarily correspond to that of the tool. Resolution is another issue. It is much easier to measure a one μrad rotation at the end of a 100 mm arm than at the base of the arm. Finally, toolpath generation for a linear fast tool servo is straightforward compared to the

toolpath generation for a rotary arm.

1.2 Summary of the Research

The design and implementation of the RFTS axis was a two-stage process. The first stage was to build a testbed to give us a physical system that closely represented the fast axis in the prototype machine. This allowed us to address the broader issues of the design. For example, would precision ball bearings have the necessary resolution and stiffness or would we have to use air bearings or hydrostatic bearings for the prototype machine? What would be the limitations in the mechanical design? For example, in what range of frequencies would the mechanical resonances lie? What type of control architecture should we implement? The testbed allowed us to test the performance of different components such as the bearings, the flexible coupling between the motor shaft and tool arm, and different arm designs. The primary reason for first building a testbed rather than implementing these ideas directly in a prototype machine is that it allowed us to decouple selecting the best components from packaging considerations.

Using the experience gained from working on the testbed, we then designed the RFTS axis for the prototype machine. During this stage of the design, the main issues were packaging the components and designing and fabricating the bearing structure. For the testbed, we wanted flexibility in locating the components relative to one another, in case we had to change parts. However, for the final design we wanted to integrate the separate components into one structure, which would help us locate and reference components. We also wanted to insure that the final design was structurally solid, which lead us to casting the structure rather than using a bolted structure or weldment.

1.3 Layout of the Thesis

The remainder of the thesis is structured as follows. Chapter 2 gives a brief background on ophthalmics and an overview of the prototype turning machine. Chapter 3 details the criteria for selecting the servo motor, the flexible coupling, the bearings for the RFTS axis, and the rotary sensor. We also describe the benchmarking tests performed on the hardware selected. Chapter 4 describes measuring the error in current ophthalmic lenses to determine the accuracy requirements of the prototype machine. In Chapter 5, we detail the different control algorithms implemented on the RFTS. Finally, in Chapter 6 we discuss the current status of the RFTS axis and make suggestions for future work.

Chapter 2

Overview of the Diamond Turning Machine

In order to better understand the lens fabrication process, we begin this chapter with a short description of ophthalmic lens design terminology. This gives us the context to understand the functional requirements for turning ophthalmic lenses. We then give a general overview of the RFTS and the prototype lens turning machine.

2.1 Ophthalmic Lenses

A number of references cover the topic of ophthalmic lens design more thoroughly, [15] in particular, and also in [11] [19]. Here, we provide some basics to understand the terminology in the ophthalmic industry to motivate the design of the prototype machine. Figure 2-1 shows an example of a lens designed to correct myopia, commonly known as nearsightedness. If the eye lens is working properly, it focuses rays from a distant object coming into the eye on the retina to form a clear image. The distance from the eye lens to the retina is known as the focal length of the eye lens. The inverse of the focal length is known as the power of the lens. Optical power is measured in units of diopters $\left(\frac{1}{\mathrm{m}}\right)$. For example, a lens with a focal length of 0.5 m has an optical power of 2 diopters. When a person has myopia, the eye lens has too much positive power and focuses the rays in front of the retina, which blurs the image. To correct

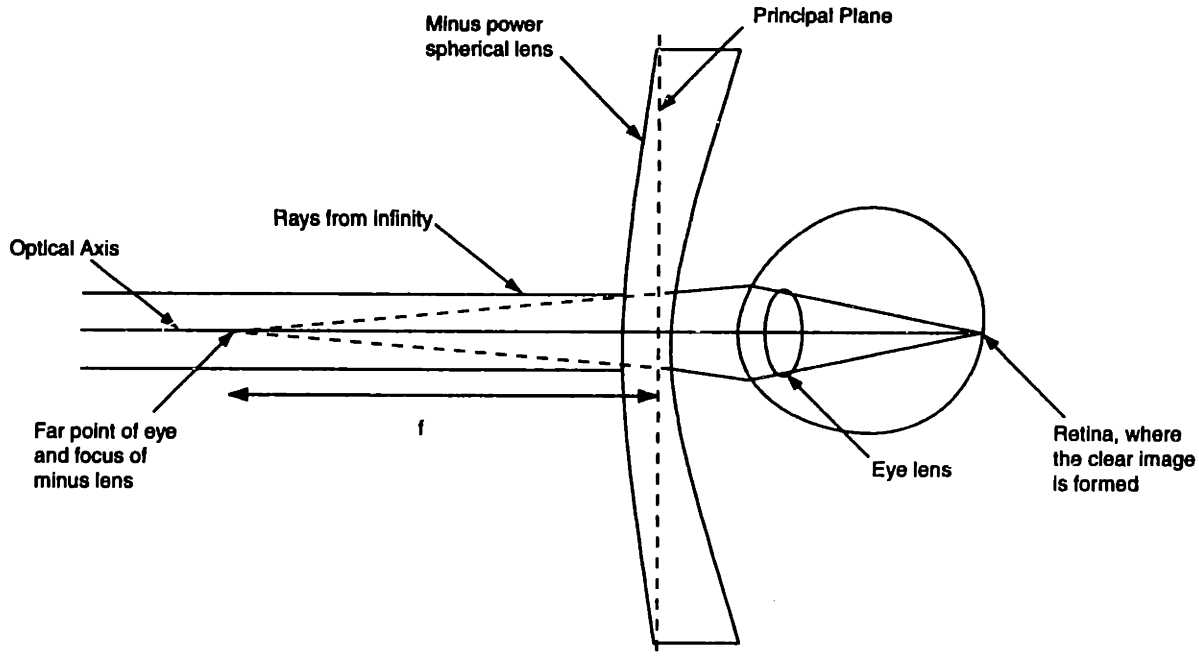

Figure 2-1: Correcting myopia, adapted from [11].

this, a negative power lens is placed in front of the eye. The negative power lens diverges the rays and cancels the excess positive power of the eye lens, as shown in Figure 2-1.

The important parameter to decide is the focal length f of the ophthalmic lens. The definition of the focal point of a lens is the point on the optical axis where rays coming from infinity intersect the optical axis. In Figure 2-1, the point of intersection is actually in front of the lens. Thus, the lens has a negative power. The definition of the focal length is the distance from the principal plane to the focal point. The principal plane is the plane where the extensions of the rays entering the lens and the rays emerging from the lens intersect. Since the distance from the eye lens to the ophthalmic lens is small, we can ignore it for our discussion. If the eye cannot focus an object farther than f, also known as the far point of the eye, then the focal length of the negative power lens should be the same distance. For example, if a eye could not focus on an object past 0.25 m, then a -4 diopter lens would be required to correct the nearsightedness of the eye.

The power of a ophthalmic lens P, the inverse of f, is a function of the thickness of the lens, the index of refraction of the lens N, which depends on the material of

the lens, and the radius of curvature R. For one surface the power P is

$$P = \frac{N-1}{R}. \tag{2.1}$$

To standardize lens manufacturing, the opthalmic industry has adopted a standard called tool power. The standard assumes a certain index of refraction and defines a radius of curvature R, given only the power of the lens which is desired [1]. This relation is given by

$$R = 530/P, \tag{2.2}$$

where R is in millimeters. If we neglect the thickness of the lens, valid for a thin lens, the power of the lens is approximated by

$$P = P_1 + P_2, \tag{2.3}$$

where P_1 and P_2 are the two surface powers of a single lens. The surface powers P_1 and P_2 have corresponding radii of curvature R_1 and R_2 found by eq. 2.2. For our application, the front curve R_1 is molded, and the back curve R_2 is cut to the desired surface power.

Another eye defect that ophthalmic lenses correct is astigmatism. In this case, the cornea is nonrotationally symmetric and a toric lens with two radii of curvature is required to correct the defect. The fact that the lens is nonrotationally symmetric complicates the manufacturing of the lens. Hence, toric lenses are difficult to make quickly and accurately. The mathematical description for a toric is,

$$z(x,y) = R_b - \sqrt{[R_b - R_c + \sqrt{(R_c^2 - y^2)}]^2 - x^2}, \tag{2.4}$$

where R_b is the base curve and R_c is the cross curve. A toric lens with $R_b = 26.5$ mm, $R_c = 17.6$ mm, and $x^2 + y^2 \leq 2500$ mm^2 is the test lens the turning machine must be able to cut. Figure 2-2 shows a toric surface for a 1 X 6 diopter lens with an

[1] ANSI standard Z80.1-1995

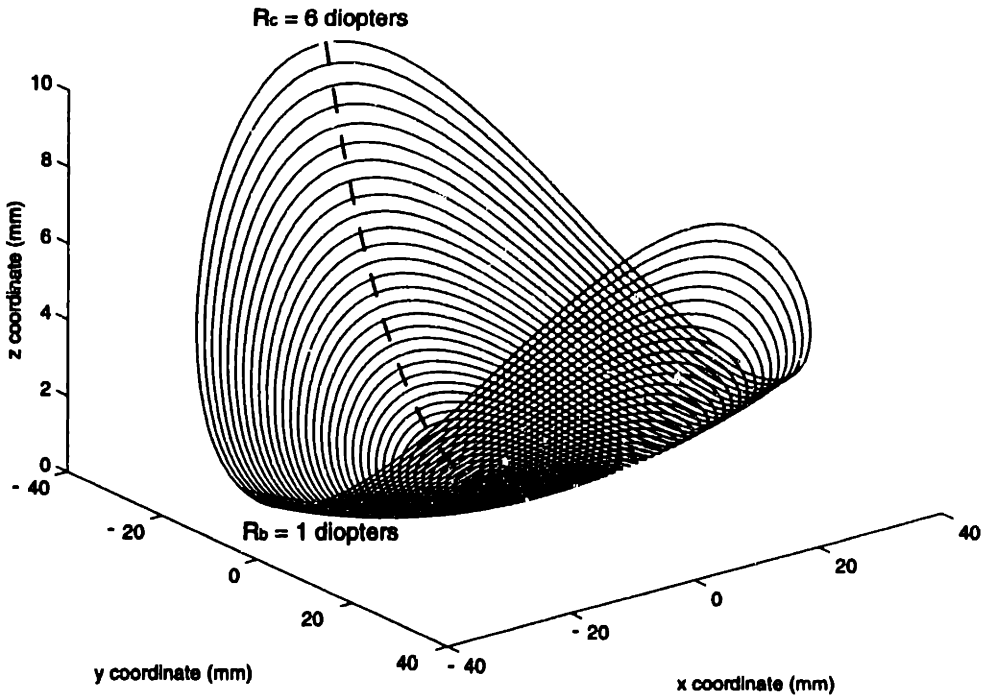

Figure 2-2: Contour of a 1X6 toric lens.

80 mm diameter. Clearly the surface is nonrotationally symmetric. The variation in height, for a given radius, increases as the difference between the cross and base powers increases. Toric lenses are often defined by their cylinder power, the difference between the cross and base powers, $P_c - P_b$.

2.1.1 Functional Requirements of the Lens Turning Machine.

Depending on the contour of the lens to be cut, a number of roughing passes are first done to machine the blank close to the desired shape. Then, one or two finishing passes are done to remove surface damage from the roughing passes and to decrease the form error. To further reduce form error, after machining the lens is typically lapped with a hard lap, which is the inverse shape of the lens. First, the lap is covered with an abrasive pad. Next, it is rotated over the lens with an abrasive slurry flooding the lap and the lens. To achieve an optically clear surface finish, the hard lap is fitted with a felt pad and the lapping process is repeated with a finer abrasive slurry.

One key goal of the new turning machine is to cut the lenses with enough accuracy to eliminate the need for hard laps. The target for form accuracy is to cut within 1 μm of the desired contour over 10 mm. In addition, we want a final surface finish of 0.2 to 0.3 μm R_q. [2] With the increase in cutting accuracy, it is possible that the hard laps could be replaced with a conformable or soft lap. Currently, a different hard lap is needed for each prescription. This leads to the high cost of storing and maintaining thousands of hard laps. A conformable lap could be used on all the lenses because it would take the shape of the lens that it is lapping. Another requirement is to start and finish the lens-making process on a blank in under one minute. Cutting closer to the final shape will also aid this goal by reducing the overall polishing time.

Turning a nonrotationally symmetric lens at high spindle speeds places strict performance requirements on the motor that actuates the rotary arm of the RFTS. As discussed earlier, the height variation at a given radius on a toric lens increases as the cylinder power increases. This implies cutting most lenses requires extremely high tool accelerations. An original assumption was that a significant number of lenses being cut were high cylinder power lenses. However, detailed analysis of the cutting paths and the accelerations required to cut the entire spectrum of ophthalmic lenses showed that this is not the case [14]. For a large number of prescriptions, the RFTS's required acceleration is relatively modest. For example, with a 3000 RPM maximum spindle speed, a 20 g machine can cut 90% of the lenses at the maximum spindle speed. This is because the majority of lenses being cut are under two diopters of cylinder power. According to [7], approximately 90% of lens prescriptions are under 2 diopters. Table 2.1 shows the profile height z of a lens with a given power at a variable radius R. For an 8X10 toric lens at a radius $R = 50$ mm, $z = 22.8$ and 35.4 along the base and cross curves, respectively. Therefore, the variation in height $\Delta z = 12.6$ mm. This is also the distance that a small radius tool on a linear axis must travel.

In terms of cutting forces, the tangential and infeed cutting forces differ depending on the type of material being cut [14]. Two types of plastics typically used are

[2] The surface finish represented by R_q is the RMS average.

Diopter	Curvature (mm)	Profile Height @ Radius of (mm)				
		10	20	30	40	50
2.0	265.0	0.2	0.8	1.7	3.0	4.8
4.0	132.5	0.4	1.5	3.4	6.2	9.8
6.0	88.3	0.6	2.3	5.3	9.6	15.5
8.0	66.3	0.8	3.1	7.2	13.4	22.8
10.0	53.0	1.0	3.9	9.3	18.2	35.4
12.0	44.2	1.1	4.8	11.8	25.4	
14.0	37.9	1.3	5.7	14.8		
16.0	33.1	1.5	6.7	19.1		
18.0	29.4	1.8	7.8			
19.0	27.9	1.9	8.4			
20.0	26.5	2.0	9.1			
22.0	24.1	2.2	10.7			
24.0	22.1	2.4	12.7			
26.0	20.4	2.6	16.4			
28.0	18.9	2.9				
30.0	17.7	3.1				

Table 2.1: Profile height of lens for a given radius.

CR39 and polycarbonate. Cutting forces are lighter when turning CR39 because the material is more brittle and fractures when cut. A cutting depth of 1 mm in CR39 produces a cutting force of approximately 10 N in the tangential (downward) direction on the tool. Polycarbonate lenses are tougher and have a higher index of refraction, which make them better for lightweight lenses. However, one of the disadvantages of manufacturing polycarbonate lenses is that the cutting forces during machining are higher. For a 2 mm depth of cut and a feedrate of 400μm/rev, cutting force studies show that forces reach 200 N and 25 N in the tangential and infeed directions, respectively. A 2 mm cut is considered to be a roughing pass, where the primary objective is to quickly machine the lens close to the final shape. For finishing passes, we are more concerned with cutting accuracy and tool deflection becomes more of a concern. Therefore, to reduce the cutting forces we can move the cross slide at a slower feedrate or turn the spindle faster.

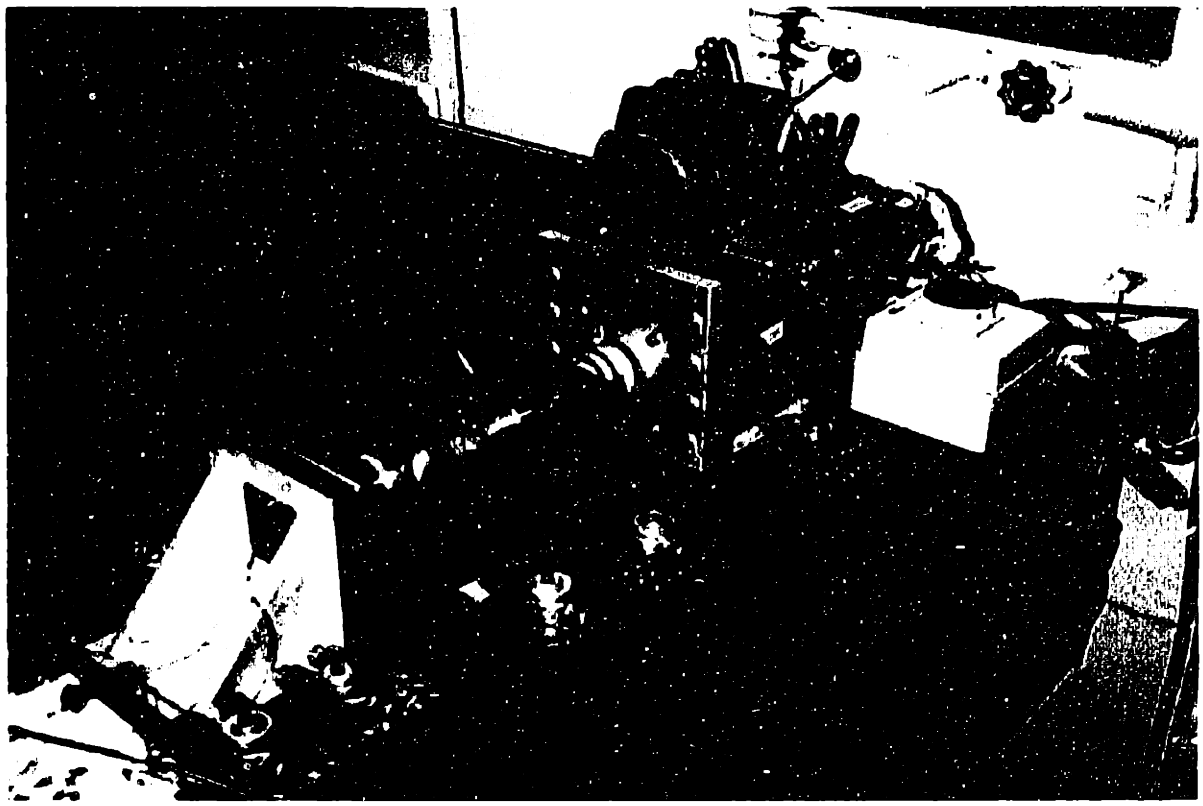

Figure 2-3: Picture of the rotary fast tool servo axis testbed.

2.2 Description of the DTM

2.2.1 Rotary Fast Tool Servo Testbed

Figure 2-3 shows a picture of the testbed. To provide a sense of scale, the tapped holes on the optical table are spaced 1" apart. The main elements of the testbed are the servo motor, the flexible coupling which connects the motor to the rotary tool arm shaft, the bearing housing, the tool arm, and the rotary sensor. The servo motor is an Aerotech BM 1400, 3.1 hp, 9.6 Nm continuous torque, DC Brushless motor mounted on a cast iron angle bracket[3]. The power amplifier is an Aerotech BA 30, 15 Amp continuous current, 4080 Watt servo amplifier. The tool arm shaft driven by the motor is a surface-hardened steel shaft, approximately 10 inches long, with a nominal diameter of 20 mm. The tool arm, onto which the cutting tool is bolted, clamps onto the shaft. A Zero-Max SC-050 flexible coupling joins the tool arm shaft

[3]Aerotech, Inc., 101-T Zeta Dr., Pittsburgh, PA 15238-2897, (412)963-7470

to the motor shaft [4]. A cast iron bearing block houses two duplex sets of Barden 204HDL, angular contact, ABEC-9, ball bearings, which are the bearings for the tool arm shaft [5]. Angular position feedback of the shaft is provided by a JDK Controls 6015-2004-30 potentiometer, which is mounted on a second cast iron angle [6]. Another flexible coupling, a Renbrandt R20, connects the tool arm shaft to the potentiometer shaft [7].

The digital control algorithm is implemented by a Tiger 31/IP DSP from DSP Research [8]. The processor is a 48 MHz, Texas Instruments TMS320C31 processor. The I/O is handled by Industry Packs, IP's, which are selected separately and added onto the DSP board. A Greenspring IP-DAC provides six, 12 bit Digital-to-Analog converters, and a Greenspring IP-HiRes provides four, 16 bit Analog-to-Digital Converters [9]. The host computer is a 50 MHz, Gateway 2000, 486DX2.

Essentially, the testbed has all the components of the rotary fast tool servo axis. However, the advantage of first building the testbed is that we do not have to be extremely careful with packaging while we benchmark the components. Laying the testbed down on an optical table also gives us flexibility to replace parts such as the flexible coupling and the sensor. In addition, it allows us to test control algorithms and control hardware, such as the DSP board, in an environment that closely resembles the final RFTS axis. In chapter 3, we describe the tests to benchmark the components in the testbed.

2.2.2 Description of the Prototype RFTS Axis

Figure 2-4 shows a drawing of the second-generation prototype RFTS axis. The second-generation design integrates the function of the testbed's main elements into one structure. The monolithic bearing structure is a casting with the bearing bores

[4]Zero-Max Inc., 13200 Sixth Ave., N., Minneapolis, MN 55441-5509, (800)533-1731
[5]The Barden Corporation, 200-T Park Ave., Danbury, CT 06813, (203)744-2211
[6]JDK Controls Inc., 424-T Crown Point Cir., Grass Valley, CA 95945 (530)273-4608
[7]Renbrandt Inc., 659 Massachusetts Ave., Boston, MA 02118 USA (781)370-3539
[8]DSP Research, Inc., 1095 East Duane Ave., Sunnyvale, CA 94086, (408) 773-1042
[9]Greenspring Computers, 1204 O'Brien Drive, Menlo Park, CA 94025, (415)327-1200

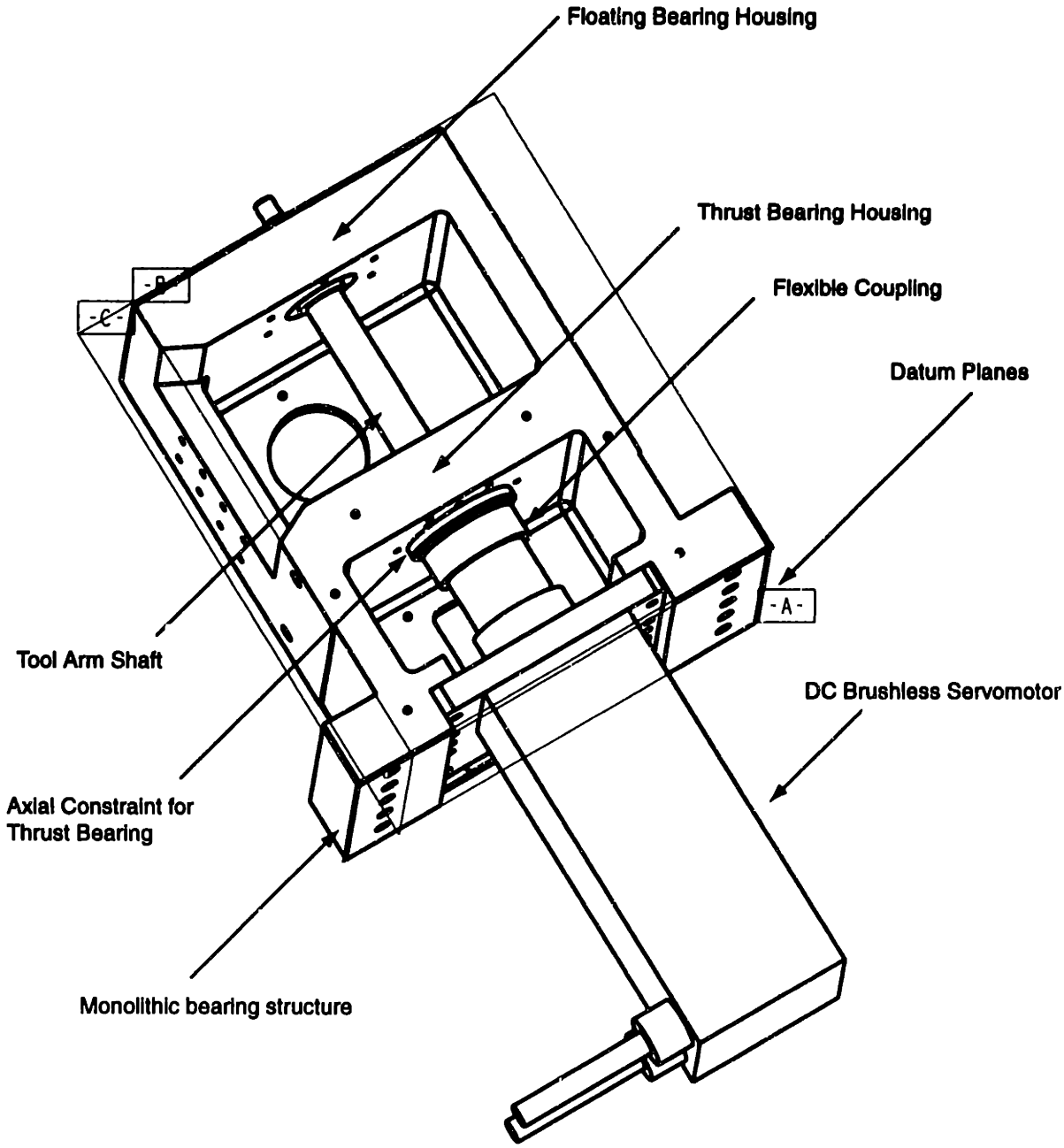

Figure 2-4: Drawing of the second-generation rotary fast tool servo axis.

machined directly into it. Rather than being mounted on a separate angle iron as in the testbed, the servo motor now bolts directly into the bearing structure. In terms of functionality, it is similar to the original design. However, in certain aspects, the second-generation design is a significant improvement over the testbed design. One improvement is that we can grind datum planes onto the bearing structure and then reference all the features with respect to these datums. In Figure 2-4, the three datum plans A, B, and C are shown. Now, we can specify to what tolerance the tool arm shaft is to be square with respect to the machine base. In this case, using a surface plate provided by Moore Tool as a machine base is a tremendous aid, because we can be sure that the base is flat to a high degree of precision. Another advantage is that the bearing structure is a monolithic piece. Structurally, it should be stiffer and better damped that the previous bearing structure, which was bolted together. In addition, all of the alignments in the structure are set and will not creep over time. In chapter 4, we describe the mechanical design in further detail.

As before, the bearings are duplex ABEC-9 bearings mounted back-to-back inside each bore. One difference is that the new bearings have a slightly larger inner bore diameter, 25 mm, to accommodate a slightly larger tool shaft diameter. This should increase the system's torsional stiffness. In chapter 3, we address the issue of torsional stiffness in the context of dealing with system resonances. The duplex set of bearings in the lower housing act as the thrust bearing for the tool arm shaft. A shoulder in the lower bearing housing axially constrains the bearings' outer races on one side, and a clamp on the underside of the housing constrains the thrust bearings on the opposite side. In the upper bearing housing, the fit on the bearings' outer races is looser. This allows the bearings to "float", permitting thermal expansion of the shaft. The bearing design is also explained in more detail in chapter 3. Figure 2-5 shows a picture of the RFTS axis before being bolted to the machine base.

2.2.3 Description of the Prototype DTM

Figures 2-6 and 2-7 show a picture of the prototype DTM and a drawing of the machine's layout, respectively. The spindle, cross slide, and the RFTS axis are

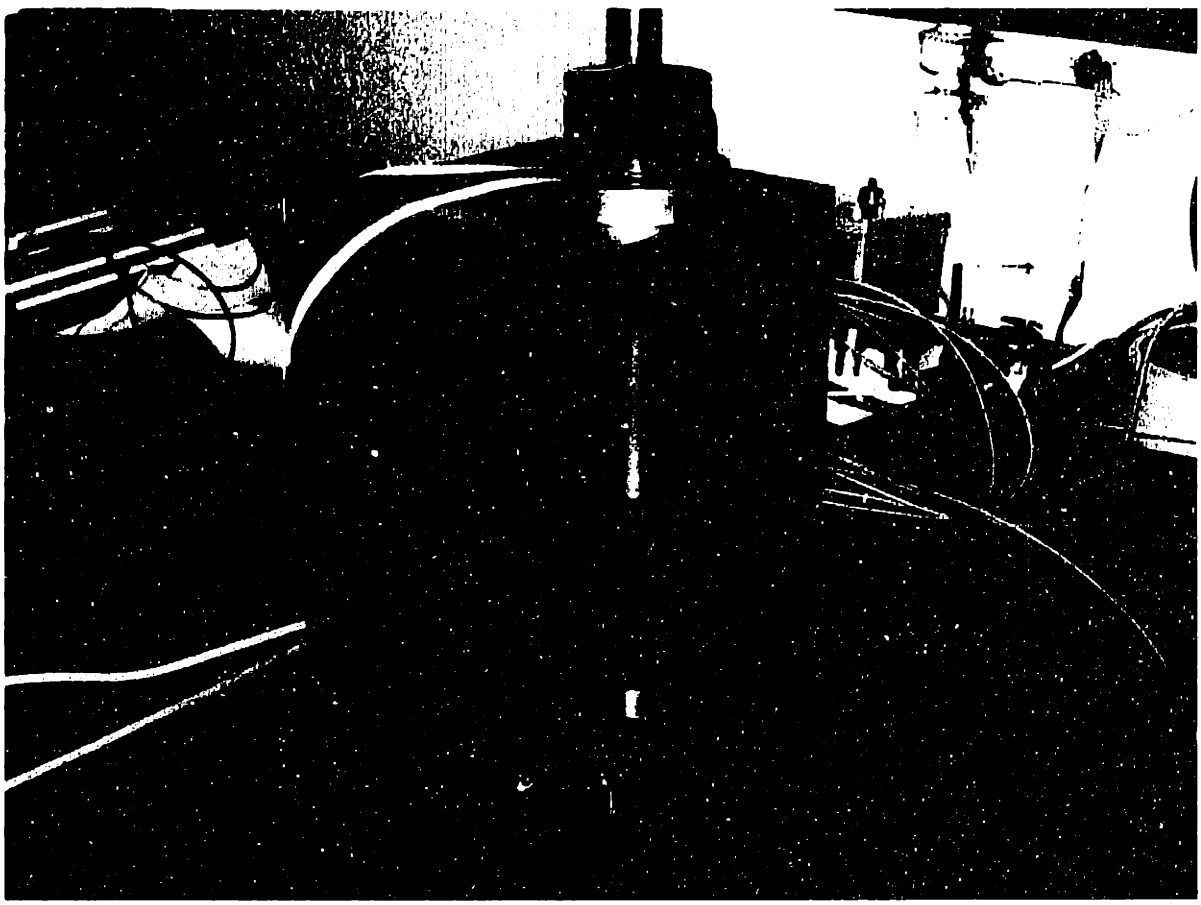

Figure 2-5: Picture of the second-generation rotary fast tool servo axis.

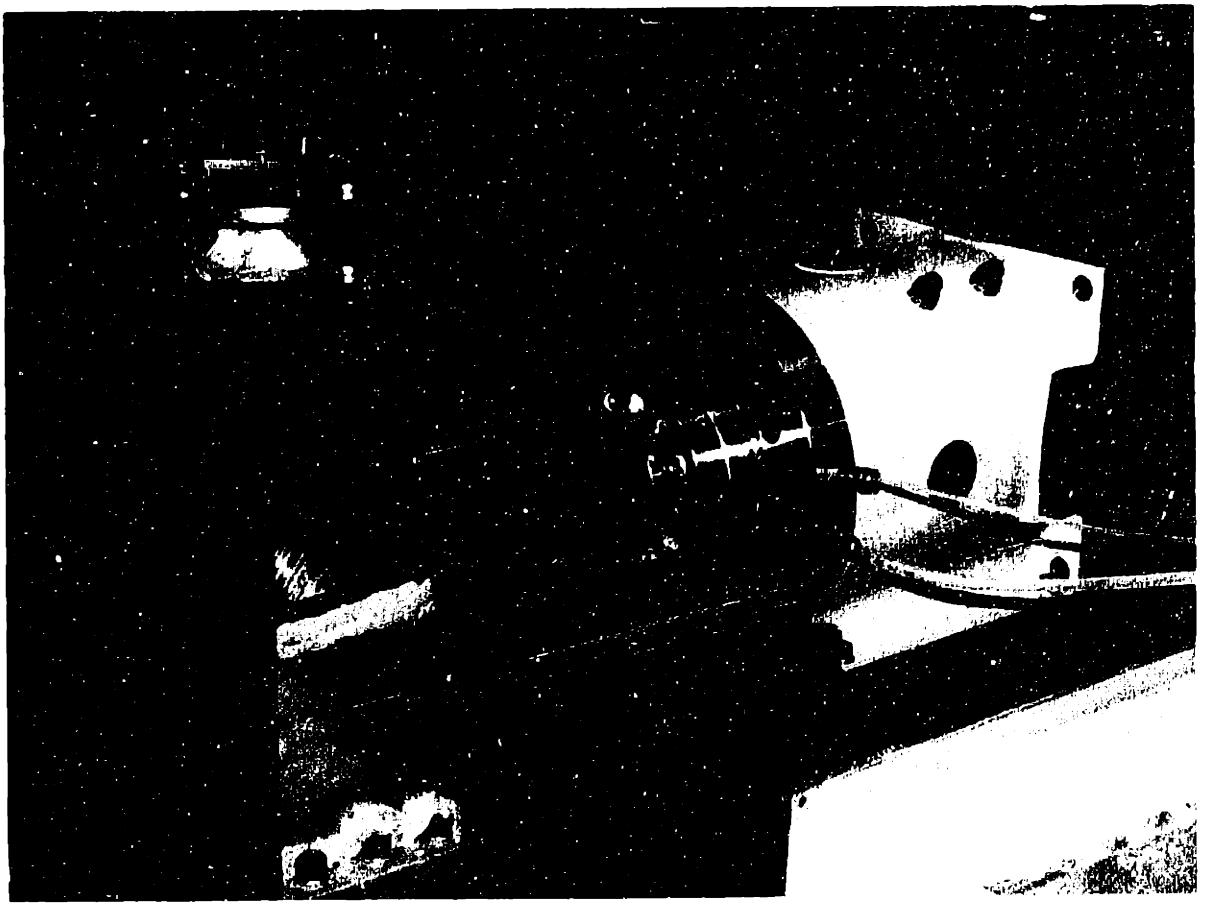

Figure 2-6: Picture of the prototype Diamond Turning Machine.

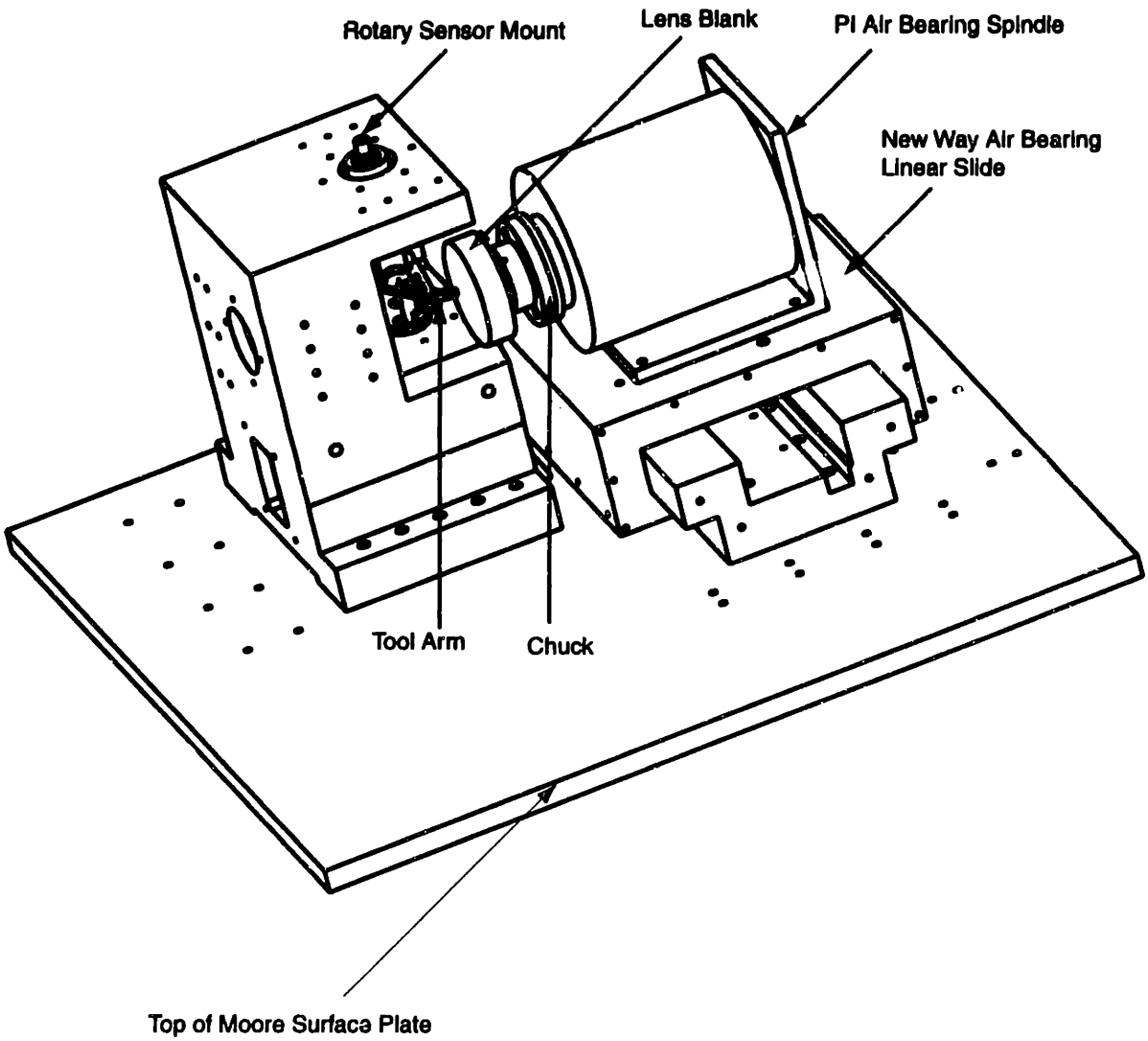

Figure 2-7: Drawing of the prototype Diamond Turning Machine.

bolted down to a modified surface plate supplied by Moore Tool Company [10]. The spindle is a 4R Twinmount air bearing spindle from Professional Instruments [11]. It has a maximum speed of 10,000 RPM and error motions in the radial and axial directions of less than 25 nm (1 microinch). Spindle position is measured by a 10,000 count encoder. The cross slide is a porous graphite air bearing cross slide made by New Way Machine components [12]. An Anorad LEB-S4 linear motor drives the cross slide carriage [13]. A Sony SH-10, glass-scale linear encoder with a resolution of 0.1 μm measures the position of the cross slide [14]. The spindle and cross slide for the prototype machine have extremely low error motions, which make them over-designed for our prototype machine. However, it makes sense to make these two axes as "perfect" as possible, because the bulk of the research will take place on the third axis, the RFTS axis. Therefore, we want the other two axes to be more than good enough so that we can readily determine the errors in the RFTS axis.

[10]Moore Tool Company, 800 Union Ave., PO Box 4088, Bridgeport, CT 06607-0088, (203) 367-0418

[11]Professional Instruments Co., Inc., 4605 Hwy. 7, Minneapolis, MN 55416, (612)933-1222

[12]New Way Machine Components, Inc., 4009-I Market Street, Aston, PA 19014, (800)394-1046.

[13]Anorad Corp., 110 Oser Ave., Hauppauge, NY 11788, (516)231-1995

[14]Sony Magnescale Inc, Toyo Building, 9-17, Nishigotanda 3-chome, Shinagawa-ku, Tokyo, 141 Japan, Phone: 81-3-3490-9841

Chapter 3

Mechanical Design and Component Selection

In this chapter we lay out the design criteria and other factors for choosing the different components of the rotary fast tool servo axis. We also describe the tests done to benchmark the components, verifying their performance. The components to be tested are the servo motor, the tool arm shaft bearings, and the flexible coupling between the servo motor and the tool arm shaft. In addition, we compare commercially available rotary sensors and describe the laser encoder chosen. With the data from working on the testbed, we are then able to finalize the design for the RFTS axis.

3.1 Motor Selection

3.1.1 Functional Requirements of the RFTS Axis Motor

The required torque output of the RFTS motor depends on many factors, including maximum speed of the spindle, the feedrate of the cross slide, the tool's depth of cut, and the system inertia. With all these parameters variable depending on the final machine configuration, we try to lay out a general methodology for selecting a rotary motor to drive the RFTS. The important parameters for selecting the motor are,

- Adequate torque to accelerate the tool when following cutting path trajecto-

ries in the presence of cutting forces. For a 100 mm tool arm, the estimated acceleration required is 20 g at the tool tip.

- The voltage and power requirements to drive the RFTS should not surpass the ratings of the motor or amplifier.

Simulated cutting paths have shown that, assuming a maximum spindle speed of 3000 RPM, a RFTS with an acceleration of 20 g (200 m/s^2) can cut 90% of all the prescriptions at the maximum spindle speed. A 40 g (400 m/s^2) machine can cut 95% of all the prescriptions at the same maximum spindle speed [14]. To select a motor for the rotary fast tool servo axis, we begin by calculating the required torque output of the motor. In these calculations we assume that the radial length r from the tool arm axis to the tool edge is 100 mm. The inertia of the system J_T is the sum of the motor armature, the tool arm shaft, the flexible coupling, and the tool arm inertias. For ease of calculation, we assume a system inertia of 2×10^{-3} kg-m^2. The estimated inertia of the current RFTS axis is somewhat less than this, 1.67×10^{-3} kg-m^2, but is also expected to increase as we modify the tool arm design. As an estimate, 2×10^{-3} kg-m^2 is a reasonable prediction for the final tool arm design. The motor's required torque T includes the acceleration torque T_A and also the load torque caused by the infeed cutting forces T_L

$$T = T_A + T_L. \tag{3.1}$$

The necessary angular acceleration α to produce a tangential acceleration a at the tool is simply

$$\alpha = \frac{a}{r} = \frac{200}{0.1} = 2000 \text{ rad/s}^2. \tag{3.2}$$

With a system inertia J_T of 2×10^{-3} kg-m^2, the torque T_A necessary to accelerate it at 2000 rad/s^2 is

$$T_A = J_T \alpha = 2 \times 10^{-3} \cdot 2000 = 4 \text{ Nm}. \tag{3.3}$$

To estimate the load torque of the motor, we take the example discussed earlier of turning polycarbonate at a cutting depth of 2 mm. The infeed cutting force F_C in

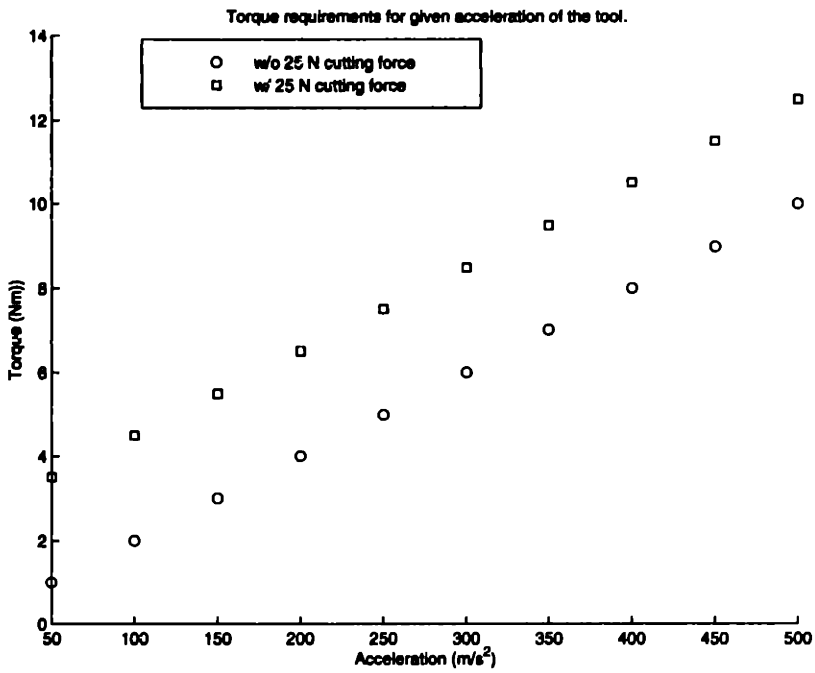

Figure 3-1: Torque requirement for given acceleration.

that case is 25 N, and the load torque T_L is thus

$$T_L = rF_c = 0.1 \cdot 25 = 2.5 \text{ N}. \tag{3.4}$$

This yields a total torque requirement of $4 + 2.5 = 6.5$ Nm. Figure 3-1 shows the motor's required torque output, calculated for a range of accelerations, with and without a 25 N infeed cutting force.

Currently, we are using an Aerotech BM1400, DC brushless motor, which was selected at the beginning of the project. The motor has performed well in our tests and we plan to continue using it to drive the RFTS. The BM1400 has a power rating of 3 Hp (2200 Watts), and a continuous torque rating of 9.6 Nm. As found earlier, a 20 g machine requires a torque output of only 6.5 Nm, but the continuous torque rating of the Aerotech motor is much higher. Thus this motor has the torque capability to accelerate the tool at almost 50 g without cutting forces, and 35 g assuming a heavy infeed cutting force of 25 N. Although the current motor may be oversized, some degree of over-design in the prototype RFTS axis is necessary to be conservative in

meeting our requirements. Using a higher-rated motor also gives us the option of cutting a higher percentage of prescriptions at the maximum spindle speed, which decreases process time.

3.1.2 Selecting a Motor

Before selecting the Aerotech motor, we conducted a survey of motors from commercial vendors. Since it is difficult to review all the motor manufacturers, we select some of the well-known companies and outline a methodology to choose between their motors. Servomotors we consider for this application are DC brushless motors, DC brushed motors, and direct drive torquer motors. Choosing a suitable motor is nontrivial because of the unusual requirements of the RFTS axis. The oscillatory trajectory of the tool requires high accelerations when cutting a toric lens, but relatively low rotational speed of the tool arm, on the order of 10.5 rad/s (100 RPM).

One of the motor's primary requirements is to have enough torque capacity to accelerate the tool. At first, direct-drive torquers seem to be a reasonable choice to meet our requirements. Compumotor makes high-performance direct-drive motors with continuous torque ratings of up to 200 Nm [1]. Some systems also have encoder feedback with resolutions of 1,024,000 counts/revolution, which is ideal for a direct-drive system with the tool arm shaft integrated into the motor. However, in terms of torque-to-inertia ratio, their acceleration capabilities are much lower than DC brushless motors. For example, the armature inertia of the Aerotech BM 1400 is 5.6×10^{-4} kg-m^2. This gives a torque-to-inertia ratio, i.e. the angular acceleration of the rotor inertia by the continuous torque rating of the motor, of 17777 rad/s^2. The Compumotor DR 1015B has a continuous torque rating of 10 Nm and a rotor inertia of 2.1×10^{-2} kg-m^2. This gives a torque-to-inertia ratio of only 476 rad/s^2. Also, direct-drive torquers are speed limited. The DR 1015B has a rated speed of only 2 rad/s (19 RPM), which is too slow for our application.

In Figure 3-2 we plot the continuous torque rating as a function of armature

[1] Compumotor Div. Parker Hannifin Corp., 5500-T Business Park Dr., Rohnert Park, CA 94928-7902, (800)358-9070

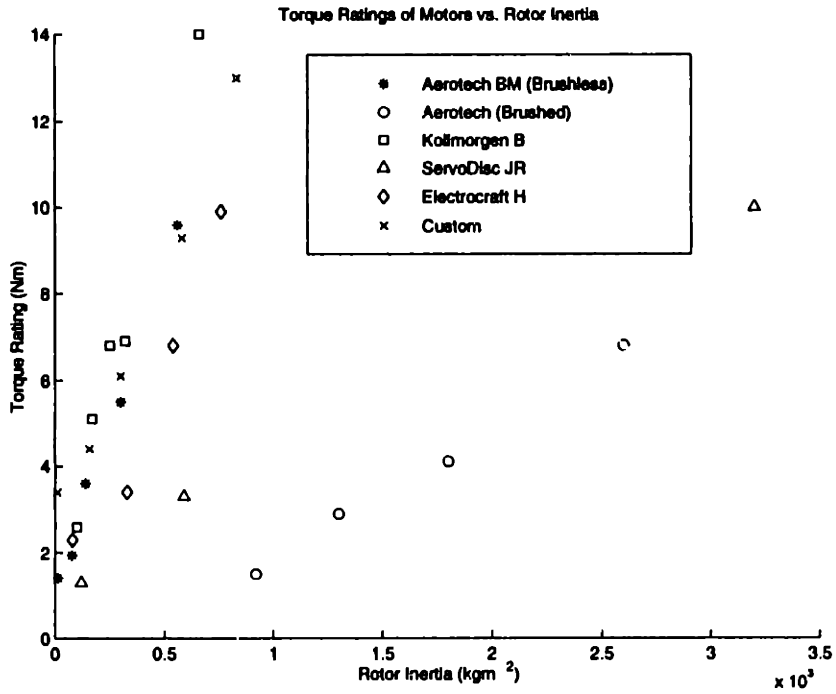

Figure 3-2: Comparison of torque-to-inertia ratio of motors from different manufacturers.

inertia for a range of DC brushless motors from Aerotech, Kollmorgen, Electrocraft and Custom. For comparison, we also plot the torque-to-inertia ratio of Aerotech brushed DC motors and Kollmorgen ServoDisc brushed motors [2] [3] [4]. ServoDisc motors have ironless armatures, and thus extremely low inductances, and higher torque-to-inertia ratios than normal brushed DC motors. From Figure 3-2, we see that because of their low rotor inertias, DC brushless motors have much higher acceleration capabilities than brushed DC motors, including the ServoDisc motors. In general, Kollmorgen motors have the highest continuous torque ratings for given rotor inertias. Electrocraft motors have the lowest torque ratings for given inertias. Aerotech and Custom DC brushless motors fall between the first two.

Table 3.1 compares the characteristics of brushless DC servomotors from the motor manufacturers with comparable torque ratings and rotor inertias to the Aerotech BM1400. Table 3.2 lists the torque-to-inertia ratios of the motors calculated by

[2]Kollmorgen Motion Technologies Group, 201 Rock Rd., Radford, VA 24141(800) 777-3786
[3]Custom Servo Motors Inc., 214 N. Valley, New Ulm, MN 56073, (507)354-1616
[4]Electro-Craft, 6950 Washington Ave. So., Eden Prairie, MN 55344, (800) 328-3983

Motor Type	Continuous Torque (Nm)	Peak Torque (Nm)	Power (Watts)	Km (Nm/amp)	J ($kg - m^2$)	L (mH)	R (ohms)
Aerotech BM1400	9.6	24	2330	0.74 (RMS)	5.6 E-4	1.7	0.5
Aerotech 1960	6.8	31.7	1160	0.7	2.6 E-3	7.1	0.8
Kollmorgen B-404A	13.8	35.9	2000	2.31 (RMS)	6.56E-4	102	4.1
Kollmorgen B-404C	13.9	35.3	5400	0.66 (RMS)	6.56E-4	8.4	0.34
ServoDisc JR24M4CH	10.2	82.3	3188	.41	3.2E-3	.045	0.31
Electrocraft H-4075	9.9	19.8	3110	0.74	6.8E-4	5.4	0.9
Custom MPM1143FRM-A	13.1	45.7	3400	0.71	8.3E-4	1.1	0.13

Table 3.1: DC Servomotors

Motor	Torque-to-Inertia Ratio (rad/s^2)
Aerotech BM1400	17142
Aerotech 1960	2615
Kollmorgen B-404A	21036
Kollmorgen B-404C	21189
ServoDisc JR24M4CH	3187
Electrocraft H-4075	14558
Custom MPM1143FRM-A	15783

Table 3.2: Torque-to-inertia ratios

dividing the continuous torque rating by the rotor inertia. Notice that the brushed DC motors have lower torque-to-inertia ratios compared to the brushless DC motors. Among the brushless DC motors with similar rotor inertias, Kollmorgen has the highest performance motor. The B-404C has the highest torque-to-inertia ratio, 21189 rad/s^2, while the Electrocraft H-4075 has the lowest, 14558 rad/s^2. To put this difference into perspective, for a system inertia of 2.0×10^{-3}kg-m^2 and a 100 mm tool arm, a tool driven by the Kollmorgen motor would have a maximum acceleration of 65 g, while the Electrocraft motor could accelerate the same system at 50 g.

However, other factors need to be considered when selecting the motor. For example, we must also analyze the voltage and power requirements to drive the motors. Earlier, we estimated that to accelerate the RFTS at 20 g in the presence of cutting forces requires a torque $T = 6.5$ Nm. Using this metric, we can compare the motors' voltage and power requirements, as well as their heat dissipation. We first make the assumption that all the DC brushless motors have approximately the same inertia. Thus, the total inertia J_T and the torque output T are the same in all cases. Another assumption is that the acceleration profile of the tool is perfectly sinusoidal when

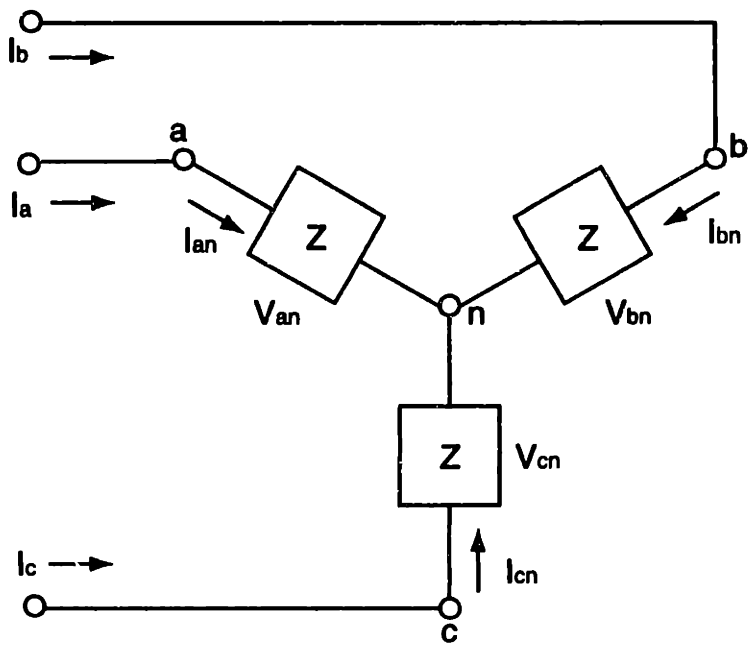

Figure 3-3: Three-phase circuit diagram for a WYE connected motor.

cutting a toric lens, and that the frequency is equal to twice the spindle frequency. The true acceleration will have higher harmonics of the spindle frequency, but we are interested only in the overall amplitude. A sinusoidal acceleration also implies a sinusoidal current. Therefore, we assume the current to be

$$i = A\sin(\omega t), \tag{3.5}$$

where $A = T/K_t$ is the amplitude of the current required to create a torque T. Here, K_t is the torque sensitivity constant given in Nm/Amp. Note that some manufacturers give their K_t in terms of RMS Amps, where

$$K_t = \frac{\text{Nm}}{\text{Amp}_{\text{RMS}}\sqrt{2}} = \frac{\text{Nm}}{\text{Amp}}. \tag{3.6}$$

To find the voltage and power requirements of the DC brushless motors, we have to consider the fact that the motors have three phases. Figure 3-3 shows the circuit diagram for a three-phase wye connected motor. The three phases are labeled a, b, and c. The phase-voltages are V_{an}, V_{bn}, and V_{cn}. Similarly, the phase currents are I_{an}, I_{bn} and I_{cn}. By inspection we can see that $I_a = I_{an}$, $I_b = I_{bn}$, and $I_c = I_{cn}$.

Note that all voltages and currenst are RMS. The complex impedance in each phase is represented by Z. Taking phase a for example, the complex impedance can be modeled as the phase resistance R_a in series with the inductance L_a of the phase

$$Z_a = R_a + j\omega L_a. \tag{3.7}$$

Table 3.1 lists the line-to-line resistance and inductance, which are twice the phase resistance and inductance. Since the current profile is sinusoidal, we calculate the voltage and power requirements of the motor by analyzing the motor as a steady-state AC circuit. A helpful, basic reference on AC circuits and three-phase circuits is [17]. In order make this analysis, we make several assumptions. By assuming the current profile is steady-state, we are taking a snapshot in time and modeling the current as a perfect sinusoid with constant amplitude and frequency. In the real case, the current profile is not a perfect sinusoid and the amplitude is changing as the acceleration profile of tool changes. However, we are interested in the general voltage and power requirements of the motor. Therefore, we make this assumption to simplify our analysis. Also, the current through the three phases of the motor is position dependent. As the rotor turns, the currents in the phases vary sinusoidally and are 120° apart. Another assumption that we make in our snapshot is that rotor is in a position where no current is in phase c. In this situation, the current I_a is equal and opposite to I_b

$$I_a = -I_b = \frac{T}{K_t\sqrt{2}}, \tag{3.8}$$

where we have divided the peak current by $\sqrt{2}$ to obtain I_a and I_b, the RMS currents. Since I_a and I_b are equal in magnitude, we can refer to the current in the two phases as I. If the angular excursion of the arm is small, and our motor is operating about this point, we assume that no current is in phase c throughout the commutation. The assumption is valid provided the angular excursion of the tool arm is small enough that very little current is in phase c. This implies that the current given by eq. 3.5 runs entirely through phases a and b. Now, we are looking at a special case where the three phase circuit can be modeled as phase a in series with phase b. While we

make many assumptions in this analysis, the voltage and power requirements we find should be indicative of the true voltage and power requirements. The line-to-line voltage RMS V_l to drive the motor is

$$V_l = IZ_l. \tag{3.9}$$

where Z_l is the magnitude of the complex line-to-line impedance given by

$$Z_l = \sqrt{R_l^2 + (\omega L_l)^2}, \tag{3.10}$$

where R_l and L_l are the line-to-line resistances and inductances, respectively. The effects of Back EMF is ignored here, but will be analyzed later. The power P in the motor is

$$P = I^2 Z_l. \tag{3.11}$$

We should note that the power P is the complex power and includes active power and reactive power. Reactive power is the power stored in the inductance of the circuit and is not actually consumed. However, when sizing the power amplifier, reactive power still needs to be considered. To distinguish it from power consumed, measured in watts, we state the complex power in units of volt-amperes (VA). In addition, we can see that the impedance ωL from the inductance of the motor armature is a large factor in determining the voltage and power requirements of the motor. For the brushed DC motors, the analysis is the same because the motors are single phase.

To compare the motors, we can look at their capacity to follow high acceleration, high frequency trajectories. Figure 3-4 shows the motors' RMS voltage and power requirements for a torque output of 6.5 Nm, as a function of tool frequency f_T. We can see there is significant variation in the voltage and power required to drive the motors. This is primarily due to the differences in the motors' inductances. Frequencies of 50, 100, and 200 Hz correspond to spindle speeds of 1500, 3000, and 6000 RPM, respectively. For f_T = 100 Hz, the Kollmorgen B-404A (KollA) requires a line-to-line voltage V_l = 178 V and a power output P = 500 VA to drive the motor. If

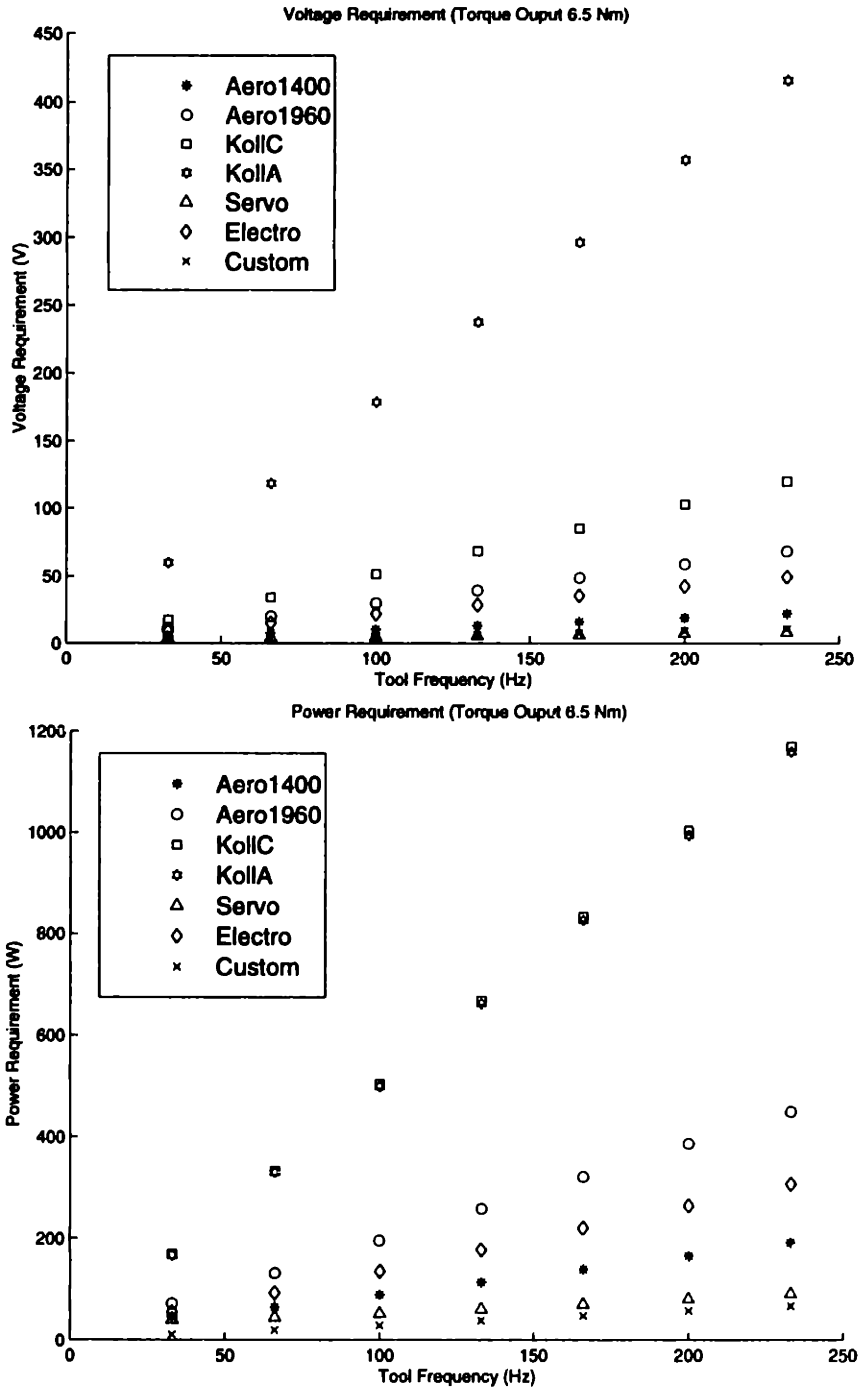

Figure 3-4: Comparison of RMS voltage and power necessary to drive motors as a function of tool frequency, at a torque output of 6.5 Nm.

f_T = 166Hz, then V_l = 296 V and P = 826 VA. Therefore, for our application the impedance of driving a motor with a high inductance can be the largest load on the amplifier. For reference, the Aerotech BA 30 amplifier has a DC bus voltage of 230 V (RMS), a continuous current rating of 15 A, and a continuous power rating of 4080 Watts. With V_l = 296 V for f_T = 166 Hz, the Kollmorgen motor would already saturate the amplifier. On the other end of the spectrum, for f_T = 100 Hz the Custom servo motor requires V_l = 5 V and P = 30 VA. If we increase f_T to 166 Hz, the Custom servo motor still needs only V_l = 8 V and P = 48 VA to drive the motor. For the same tool frequencies, the Aerotech motor (Aero1400) also has low voltage and power requirements. In this case, V_l = 10 V and P = 89 VA, for f_T = 100 Hz, and V_l = 16 V and P = 139 VA, for f_T = 166 Hz.

To see what the voltage and power requirements are for higher accelerations, we can reanalyze the motors at a higher torque output. The Aerotech BM1400 has a continuous torque rating of 9.6 Nm. According to Figure 3-1, this corresponds to an acceleration capability of 35 g in the presence of a 25 N cutting force. Figure 3-5 recalculates the motors' voltage and power requirements for a torque output of 9.5 Nm. Again, at high tool frequencies, the power required by the Kollmorgen motors can easily saturate the power amplifier. For f_T = 200 Hz, V_l = 522 V and P = 2125 VA, which also exceeds the continuous power rating of motor. The Custom and Aerotech motors appear to be the best capable of handling high acceleration, high frequency trajectories. For a spindle frequency of 6000 RPM (f_T = 200 Hz), V_l = 13 V and P = 124 VA for the Custom servo motor. In the case of the Aerotech motor, when f_T = 200 Hz, V_l = 28 V and P = 354 VA.

Heat dissipation is another issue in selecting a motor. In general, the less heat generated by the motor during operation the better. The amount of power consumed P_C by the motor is given by

$$P_C = I^2 R_l, \tag{3.12}$$

The consumed power is now given in units of watts to distinguish it from complex power. Table 3.3 compares the motors' power consumption P_C for torque outputs of

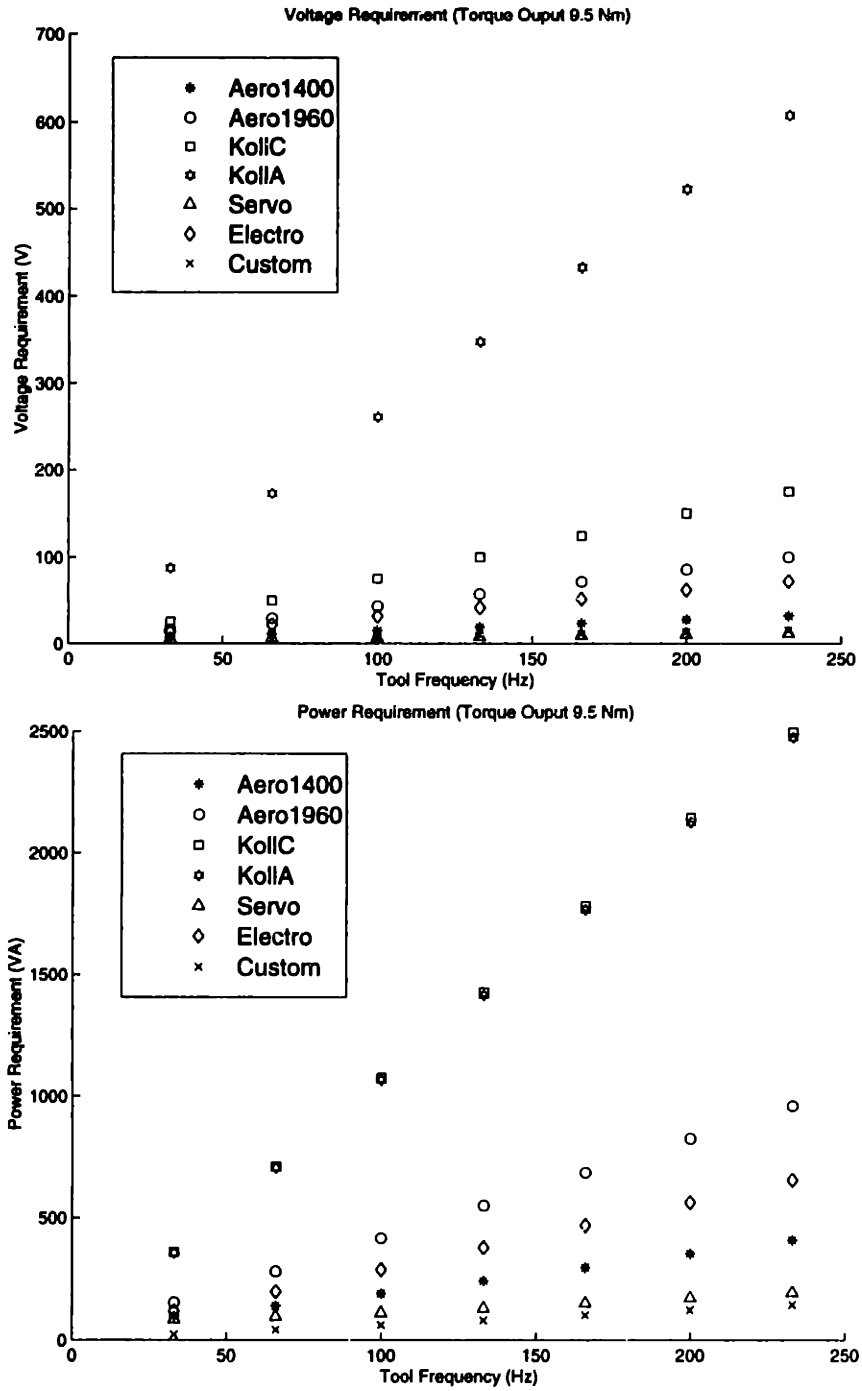

Figure 3-5: Comparison of RMS voltage and power necessary to drive motors as a function of tool frequency, at a torque output of 9.5 Nm.

Motor	Torque (Nm)	$I^2_{aRMS}R_a$	Torque (Nm)	$I^2_{aRMS}R_a$
Aerotech BM1400	6.5	27.28	9.5	58.27
Kollmorgen B-404A	6.5	22.95	9.5	49.03
Kollmorgen B-404C	6.5	23.32	9.5	49.81
Electrocraft H-4075	6.5	25.05	9.5	53.51
Custom MPM1143FRM-A	6.5	3.93	9.5	8.40

Table 3.3: Power consumed by the motors.

6.5 Nm and 9.5 Nm. Most of the motors generate approximately the same amount of heat; $P_C = 22.95$ W to 27.28 W for a torque output of 6.5 Nm. The exception is the Custom servo motor, $P_C = 3.93$ W. This is because its resistance R_l is only 0.13 Ω.

Earlier, when we were looking at the torque-to-inertia ratio of the motors, the Kollmorgen motors, which had the highest torque-to-inertia ratios, seemed like the best choice of motors. However, after analyzing their voltage and power requirements, we see that the high inductance of their motor armatures limits their ability to follow high frequency trjectories. Primarily because of their low inductances, the Custom and Aerotech motors are better candidates to drive the RFTS. In terms of having extremely low inductance and low winding resistance, the Custom Servo motor appears to be the best choice of the motors reviewed. The Aerotech motor, which we have already purchased, has relatively low inductance, but the heat it generates during operation is not lower than that of the other motors. However, the Aerotech motor has a higher torque-to-inertia ratio than the Custom motor, 17142 rad/s^2 compared to 15783 rad/s^2, and so is a compromise between high torque-to-inertia ratio and low voltage and power requirements.

The one other voltage load that we have not yet considered is the back EMF load. Considering the rotational speed of the tool arm when cutting a typical lens, the load on the amplifier from the back EMF generated is small compared to the inductive load of the motor. For example, consider again cutting an 8X10 lens, where the height variation at a lens radius of 50 mm is 12.6 mm. The tool speed varies throughout the cutting trajectory as it cuts along the radius of the lens, so we are only approximating the tool speed. To estimate the tool speed, we again assume a purely sinusoidal tool trajectory. In addition, we assume a linear axis, which is valid

for small angle excursions. The position, velocity, and acceleration of the tool are

$$x = B\sin(\omega t), \tag{3.13}$$

$$\dot{x} = B\omega\cos(\omega t), \tag{3.14}$$

$$\ddot{x} = -B\omega^2\sin(\omega t), \tag{3.15}$$

where B is 6.32 mm for the 8x10 lens described above, and ω is the tool frequency, which corresponds to twice the spindle frequency. The peak velocities and peak accelerations are $B\omega$ and $B\omega^2$, respectively. For an RFTS with an acceleration capability of 200 m/s^2

$$\omega = \sqrt{\frac{200}{0.00632}} = 179 \text{ rad/s}. \tag{3.16}$$

The peak velocity is

$$B\omega = 0.00632 \cdot 179 = 1.1 \text{ m/s}. \tag{3.17}$$

For a 100 mm arm, this corresponds to a rotational speed of 105 RPM. The back EMF constant K_B for the Aerotech BM1400 is 62 V/kRPM. Therefore, the voltage load in this case is

$$62 \cdot 0.105 = 5.9 \text{ V}, \tag{3.18}$$

and thus is insignificant.

3.2 Testing the Motor

To test if the motor can perform as predicted in the previous section, we do a simple benchmarking of the motor by implementing analog position control. The goal of this benchmarking is to test if the inductance of the motor limits our acceleration capability during high frequency trajectories. A schematic of the test is shown in Figure 3-6. The BA30 power amplifier performs two functions in velocity control mode, commutating the motor's three phases using hall effect sensors and closing the velocity loop. In the amplifier, the velocity signal is derived from motor's encoder, which has 1000 counts/revolution. Tuning the velocity loop requires changing the

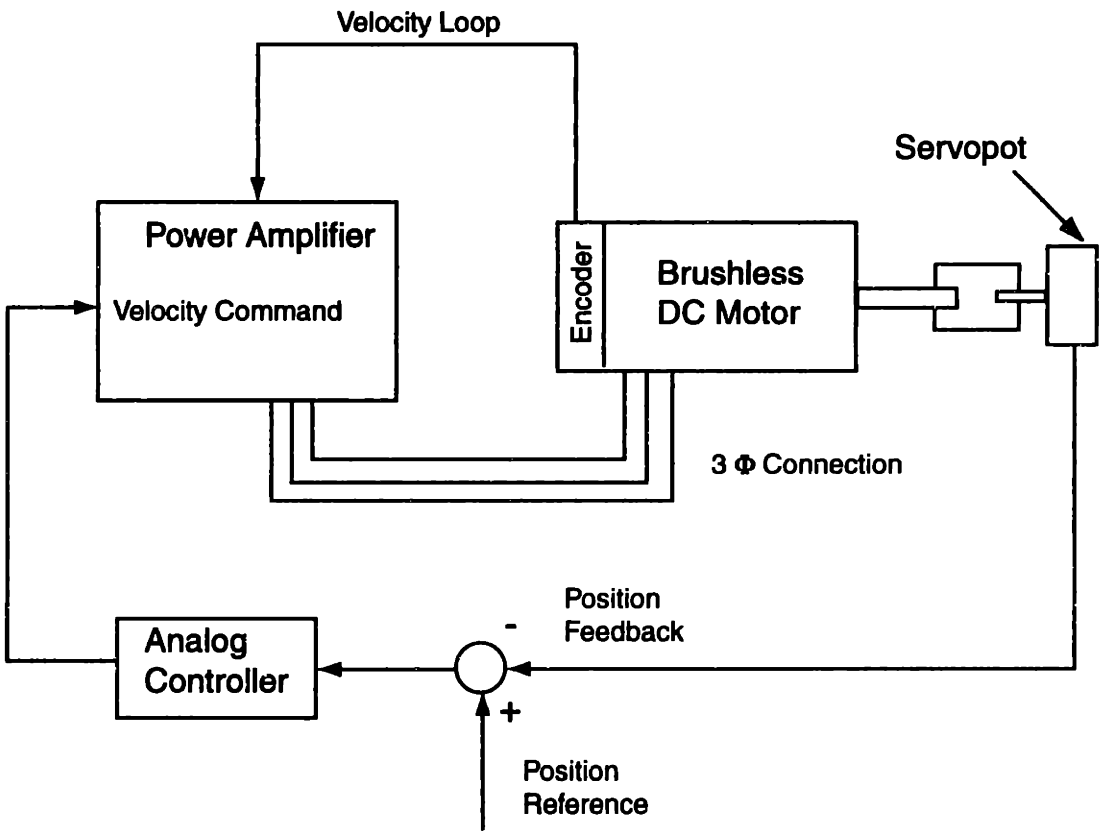

Figure 3-6: Setup used to benchmark the motor.

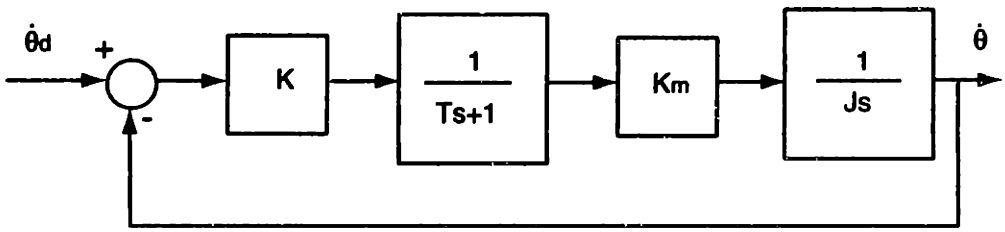

Figure 3-7: Block diagram of the velocity loop.

gains of the potentiometers on the amplifier. Figure 3-7 shows a block diagram of the velocity loop. This is a standard model of a motor under velocity control. The first gain K is the adjustable potentiometer gain of the amplifier. In our test, we are tuning the velocity loop solely by adjusting the potentiometer gain. The current loop $\frac{1}{Ts+1}$ is modeled as a first-order lag. Also, K_m is the torque constant of the motor, and J is the inertia of the system. The commanded and actual velocities are $\dot{\theta}_d$ and $\dot{\theta}$, respectively. Although the inductance of motor's phases is hidden inside the current loop and is not shown explicitly, it still determines the saturation point of the motor and the amplifier and hence the torque limit. The motor is connected to the position sensor, a JDK potentiometer, via a flexible coupling. The outer position loop is closed by a simple analog controller.

As a first step towards designing the analog controller, we first model the velocity loop closed by the power amplifier. To simplify the modeling process we can omit any rotational damping B of the motor. The loop transmission transfer function $G_v(s)$ is then

$$G_v(s) = \frac{KK_m}{Js(Ts+1)}. \tag{3.19}$$

The closed-loop transfer function for the velocity loop G_{vc} is then

$$G_{vc}(s) = \frac{\dot{\theta}}{\dot{\theta}_d} = \frac{G_v(s)}{1+G_v(s)} = \frac{\frac{KK_m}{JT}}{s^2 + \frac{1}{T}s + \frac{KK_m}{JT}}. \tag{3.20}$$

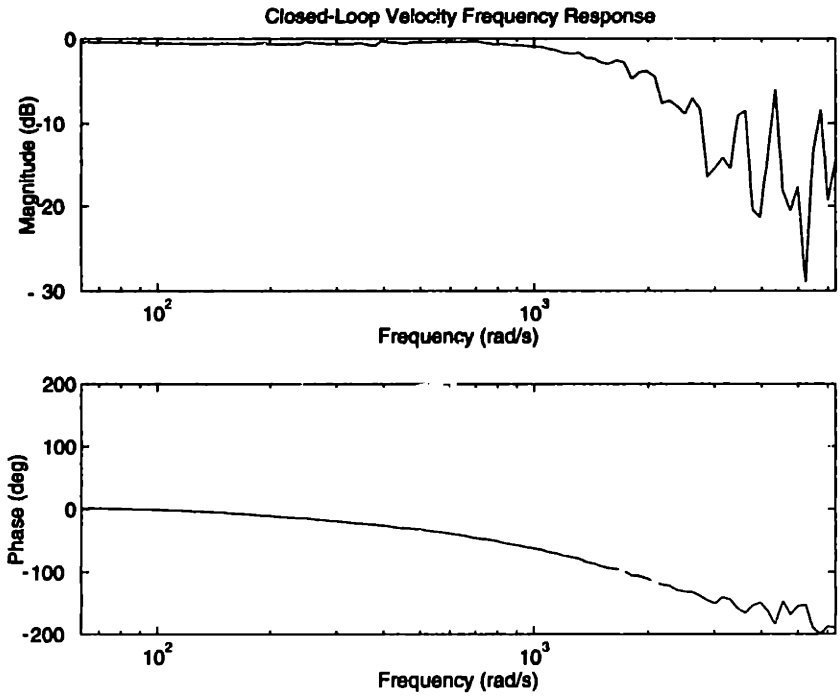

Figure 3-8: Measured frequency response of velocity loop after tuning.

We can now fit this to the generalized form of a second order system

$$G_{vc}(s) = \frac{\omega_n^2}{s^2 + 2\zeta\omega_n + \omega_n^2}, \tag{3.21}$$

where ω_n is the natural frequency of the system and ζ is the damping ratio. Figure 3-8 shows the measured frequency response of the velocity loop after tuning. The bandwidth of the velocity loop is approximately 1900 rad/s (300 Hz).

3.2.1 Tuning the Analog Controller.

Once the velocity loop is tuned, we can fit a model to the system and design a controller for the position loop. We use an analog controller for the initial testing because it can be implemented quickly. Figure 3-9 shows a block diagram of the position loop. $G_c(s)$ is the controller and θ_d and θ are the desired and actual positions, respectively. The loop transmission transfer function for the position loop $G_p(s)$ is simply

$$G_p(s) = \frac{G_c(s)G_{vc}(s)}{s} = \frac{G_c(s)\omega_n^2}{s(s^2 + 2\zeta\omega_n + \omega_n^2)}. \tag{3.22}$$

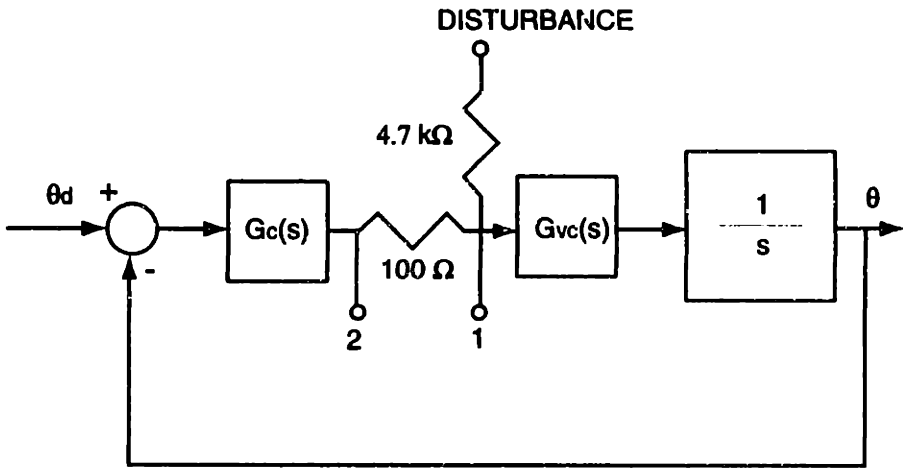

Figure 3-9: Block diagram of the position loop.

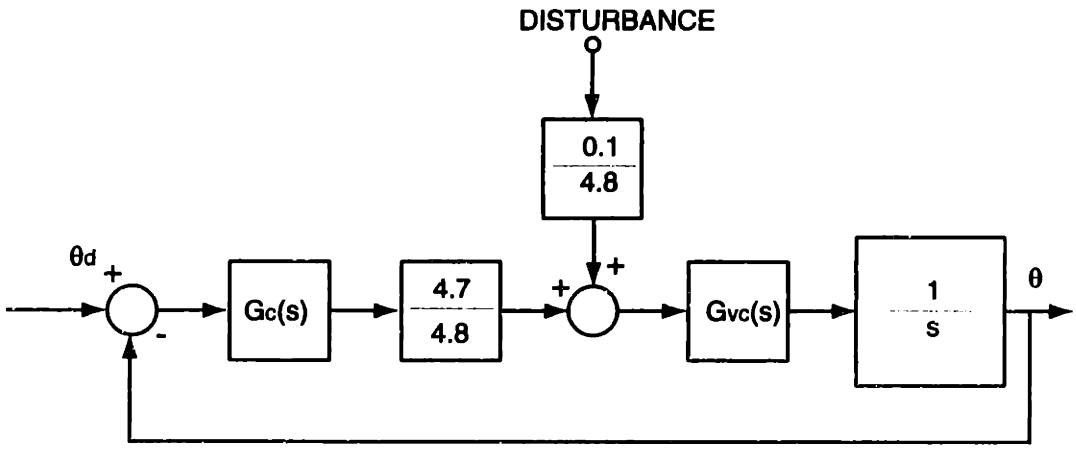

Figure 3-10: Block diagram of equivalent position loop, showing the effect of the summing junction used to break the position loop.

We are now treating the entire velocity loop $G_{vc}(s)$ as a separate block whose form we derived earlier. To fit a model to this block we start by breaking the position loop, building a summing junction, grounding the command input θ_d, and injecting a disturbance as shown in Figure 3-9. When modeling the summing junction, we assume that the output impedance of $G_c(s)$ is low and the input impedance of the amplifier G_{vc} is high. The equivalent block diagram is shown in Figure 3-10. By measuring the frequency response between points 1 and 2 as shown in Figure 3-9, we now have the negative of the loop transmission response of the position loop $G_p(s)$.

Our goal is to obtain a model of the loop transmission transfer function $G_p(s)$ which has the inner velocity loop G_{vc} inside it. To do this, several frequency responses

of the position loop $G_p(s)$ are taken while the motor is under proportional control, where $G_c(s)$ in eq. 3.22 is simply equal to a gain K_p. By varying the gain K_p, we are changing one parameter in the position loop, the crossover point. The magnitude of the response scales proportionally with the gain, but the phase of the frequency response remains the same. Assuming $G_p(s)$ is in the form given by eq. 3.22 we can predict the frequency response of $G_p(s)$ assuming $G_c = K_p$. The experimentally measured points of $G_p(j\omega)$ are expressed as

$$G_p(j\omega) = \mathrm{Re}(\omega) + j\mathrm{Im}(\omega), \tag{3.23}$$

where $\mathrm{Re}(w)$ and $\mathrm{Im}(\omega)$ are the real and imaginary parts of $G_p(j\omega)$, respectively. The magnitude of $G_p(j\omega)$ is

$$|G_p(\omega)|^2 = (\mathrm{Re}(\omega))^2 + (\mathrm{Im}(\omega))^2. \tag{3.24}$$

The phase of $\phi(w)$ is

$$\phi_p(w) = \tan^{-1}\frac{\mathrm{Re}(\omega)}{\mathrm{Im}(\omega)}. \tag{3.25}$$

The predicted frequency response $G_p(j\omega)_P$ can be found from eq. 3.22. For a frequency ω we can compare the predicted phase $\phi_p(\omega)_P$ with the measured phase $\phi_p(\omega)_M$. Then we can perform a Least Squares Fit by minimizing $\sum(\phi_p(\omega)_P - \phi_p(\omega)_M)^2$. Thus, we find the ζ and ω_n that minimizes the sum of the squared errors. For this, we write a routine in Matlab to conduct a simplex search to find ζ and ω_n. Using proportional gains K_p of 0.5, 1 and 1.5, the average of the three Least Squares Fits predicted ω_n and ζ to be 305 Hz and 0.91, respectively. Note that ω_n should be close to the bandwidth of the velocity loop found earlier to be approximately 300 Hz in Figure 3-8. A damping ratio of 0.91 indicates a fairly well-damped system which is also consistent with Figure 3-8. Figure 3-11 shows predicted frequency response of $G_p(s)$ plotted against the measured loop transmission frequency response for a controller gain $K_p = 1$. Note that the phase of the measured frequency response has been shifted by 180° to take out the phase shift from the subtraction in

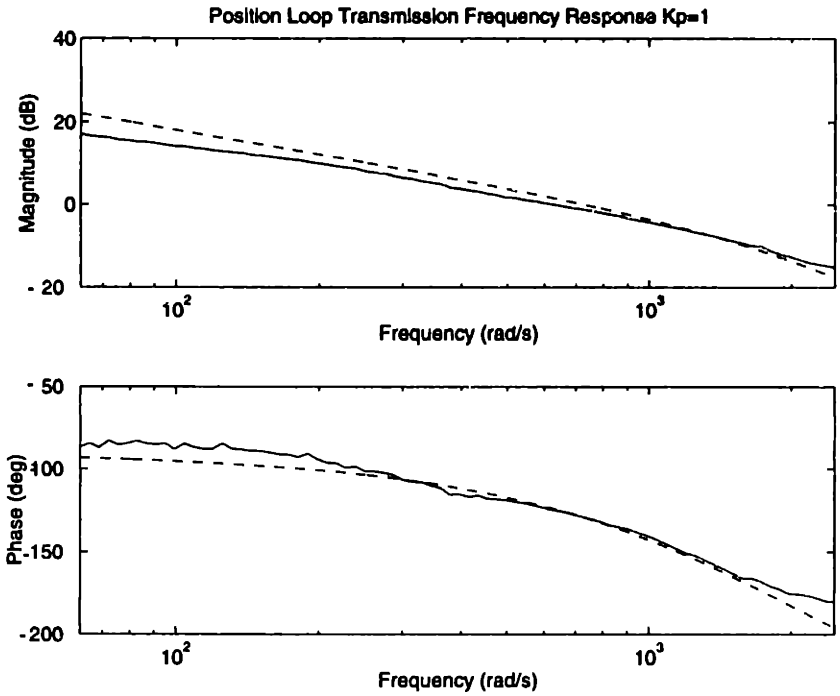

Figure 3-11: Predicted and measured loop transmission frequency responses.

the summing junction.

After modeling the dynamics of the motor, we can now design a phase-lead compensator to test the attainable bandwidth of the position loop. A standard reference for designing a phase-lead compensator is [12]. For the phase-lead compensator, $G_c(s)$ in eq. 3.22 becomes

$$G_c(s) = K_D \frac{T_i s + 1}{\alpha T_i s + 1}. \tag{3.26}$$

Here, $-1/T_i$ is the zero location of the phase-lead compensator and $-1/\alpha T_i$ is the pole location. Figure 3-12 shows the analog circuits used for the phase-lead compensation. For the subtracter circuit, $R_1 = R_2 = R_3 = R_4 = 1k\Omega$. For the lead compensation circuit, $K_D = \frac{R_f}{R_1 + R_2}$, $T_i = R_1 C$, and $\alpha = \frac{R_2}{R_1 + R_2}$. For the inverting amplifier we set the gain to unity, $R_{F2} = R_3$.

Setting the crossover frequency of the loop transmission frequency response at 200 Hz, the uncompensated system would have a phase margin (PM) of 30°. If we want the system to have a PM of 65°, the additional phase needed Φ_{max} is 35° at the crossover frequency. To obtain this phase margin the distance between the zero and

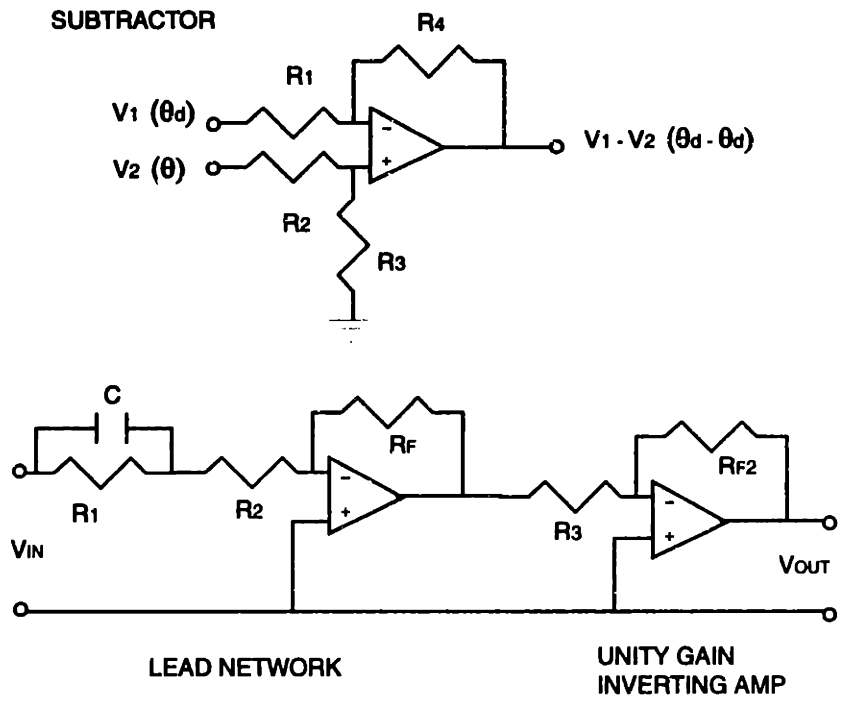

Figure 3-12: Analog circuit for phase lead compensation.

the pole of the lead compensator, represented by α is

$$\alpha = \frac{1 - sin(\Phi_{max})}{1 + sin(\Phi_{max})} = 0.27. \tag{3.27}$$

The maximum phase lead will occur at

$$\omega = \frac{1}{\sqrt{\alpha} T_i}. \tag{3.28}$$

This sets the break-point associated with the zero of the phase-lead compensator to be at 668 rad/s (106 Hz) and the breakpoint associated with the pole to be at 2470 rad/s (393 Hz). With a gain K_D of 1.1, we expect the crossover frequency ω_c to be at 1275 rad/s (203 Hz) with a PM of 61° . Implementing this controller on the testbed, the position loop transmission frequency response crosses over at 1193 rad/s (190 Hz) with a PM of 68° . The predicted and experimentally determined frequency responses are plotted in Figure 3-13. Figure 3-14 shows the closed-loop frequency response of the position loop.

The closed-loop frequency response, which shows the motor's response to a swept-

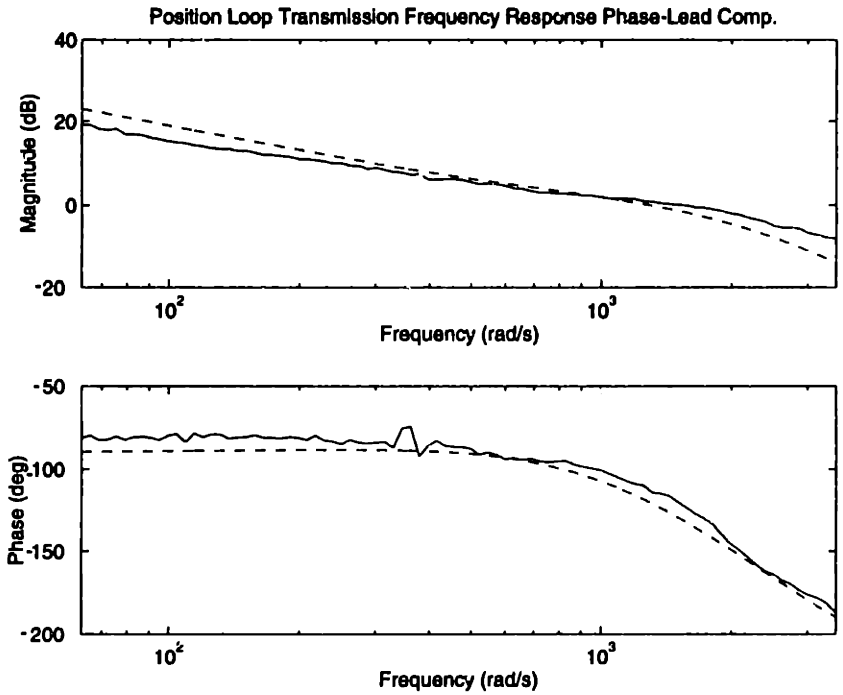

Figure 3-13: Phase Lead Compensation Predicted vs. Experimental responses.

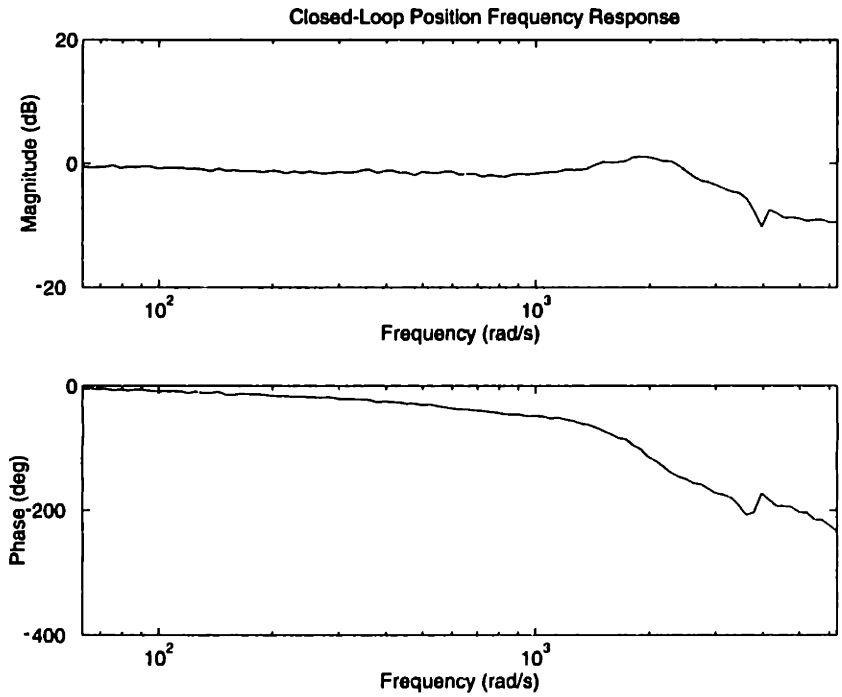

Figure 3-14: Closed-loop position frequency response.

sine test, indicates how well the motor can follow high frequency trajectories. To obtain the closed-loop frequency response, the motor is commanded to track a swept-sine command whose amplitude corresponds to a given angular excursion of the servopot. In this test, the motor is accelerating its own armature and the flexible coupling connecting the motor shaft to the servopot. Therefore, the system inertia J_T is approximately 7×10^{-4} kg-m^2. The voltage output of the servopot is ± 5 V over 340°. With a peak amplitude 5 mV, the sinewave commands a ± 0.003 rad angular excursion of the servopot. From Figure 3-14, we can see the bandwidth of the position loop is better than 2000 rad/s (318 Hz). At 2000 rad/s, the magnitude of the frequency response is approximately 1 dB. Although it is phase-shifted, the motor is still tracking the commanded sinewave. To estimate the torque output and angular acceleration of the motor, we assume that the motor is tracking a sinewave with an amplitude of 0.003 rad and a frequency of 1885 rad/s (300 Hz.) Following an analysis similar to eq. 3.15, the peak angular acceleration $\ddot{\theta}_{\text{peak}}$ is

$$\ddot{\theta}_{peak} = \theta_A \omega^2 = 0.003 \cdot 1885^2 = 10,660 \text{ rad/s}^2. \tag{3.29}$$

The torque to accelerate the system inertia T is

$$T = J_T \cdot \ddot{\theta}_{\text{peak}} = 7 \times 10^{-4} \cdot 10660 = 7.5 \text{ Nm}. \tag{3.30}$$

Thus, the current supplied by the amplifier is

$$i = \frac{T}{K_t} = \frac{7.5}{0.52} = 14.3 \text{ A}, \tag{3.31}$$

where $K_t = 0.52$ Nm/Amp is the torque constant for the Aerotech motor. If we think of the 300 Hz sinewave as a cutting trajectory, a fundamental tool frequency of 300 Hz corresponds to a spindle speed of 9000 RPM. Therefore, the test shows that the inductance of the armature does not prevent large torque or current outputs at high tool frequencies.

3.3 Rotary Bearing Selection and Testing

For many rolling element bearing applications, the main design specifications are the load ratings and the speed limit of the bearings. These factors determine the bearing's running life. However, as we showed in the previous section, the rotational speed of the tool arm shaft during operation is relatively low compared to the rotational speeds of typical machine tool spindles. Our operating speeds are on the order of 100 RPM, while precision ball bearings are rated to run at 1000's of RPM. Also, the highest cutting forces in the vertical direction are 200 N, which is well under the load ratings for a typical high performance bearing. For the bearings of the RFTS axis the main criteria are,

- Submicron radial and axial error motions of the bearings.
- Submicron deflection of the bearings under cutting force loads.
- Capable of resolving rotations on the order of 1 μrad.

These design considerations all have implications on the cutting accuracy of the tool. One unknown was whether or not conventional rolling element bearings could meet the requirements for our application. To answer this question, we use rolling element bearings in the RFTS testbed. The advantage of using rolling element bearings is that they are a standard technology and have little development time associated with them. If the bearings cannot meet the specifications, then the second-generation RFTS has to be built with fluid-static bearings. Presumably, the design of fluid-static bearings is more complex, more time-consuming and includes higher manufacturing costs than purchasing off-the-shelf rolling element bearings. For example, the maker of the motorized air bearing spindle used in the prototype machine, Professional Instruments, sells a BLOCK-HEAD 4R Air Bearing Spindle. It has extremely small error motions of less than 25 nm (1 microinch)in the axial and radial error directions. It is also stiff enough for our application with axial and radial stiffnesses of 120 N/μm and 360 N/μm, respectively. However, this performance comes at a high

price. Also, this bearing has a significantly higher rotary inertia than the equivalent rolling element solution.

3.3.1 Bearing selection and design.

There are many manufacturers of precision rolling element bearings including Torrington-Fafnir, Barden, NSK, and SKF [5] [6] [7] [8]. In selecting the bearings to use, Slocum's, "Precision Machine Design" [16] and Harris's "Rolling Bearing Analysis" [9] are very informative. Of the bearing manufacturers, I find that NSK and Barden provide the most complete application information. In addition, Barden usually has the desired bearings in stock. As a generalization, rolling element bearings come in two forms, ball bearings and roller bearings. Ball bearings are usually made more accurately because it is easier to make a perfect sphere than a perfect cylinder. However, for heavy loads roller bearings may be the only choice. For our application, the loads are not high enough to require them.

Figure 3-15 shows a cross-section of the tool arm shaft bearings. The bearings used are Barden 205HDL, which are angular contact ball bearings rated at ABEC 9 tolerances. These bearings have a contact angle of 15° and a light axial preload of 15 lbs. Two bearings are mounted in a back-to-back arrangement on each end of the tool arm shaft. In this arrangement, the contact lines converge outside the bearings. Another arrangement is to mount them face-to-face, where the contact lines converge inside the bearing. The back-to-back configuration is more common because it has more stiffness against moments exerted by the shaft. At the shaft end coupled to the servomotor, an axial clamp and a shoulder in the bearing bore constrain the outer races of the bearings in the axial direction. Thus, this set of bearings also act as the thrust bearings. On the other shaft end, the outer races of the bearings are unconstrained in the axial direction, which allows for shaft deformation from thermal effects. By letting one set of bearings "float", the shaft is not overconstrained.

[5]The Barden Corporation, 200-T Park Ave., Danbury, CT 06813, (203)744-2211
[6]NSK Corp., 3861-A Research Park Dr., Ann Arbor, MI 48106, (734)761-9500
[7]Fafnir Bearings, The Torrington Co., P.O. Box 1008, Torrington, CT 06790-1008, (800) 854-0175.
[8]SKF Motion Technologies, 1530 Valley Center Pky., Bethlehem, PA 18017, (800)423-6874

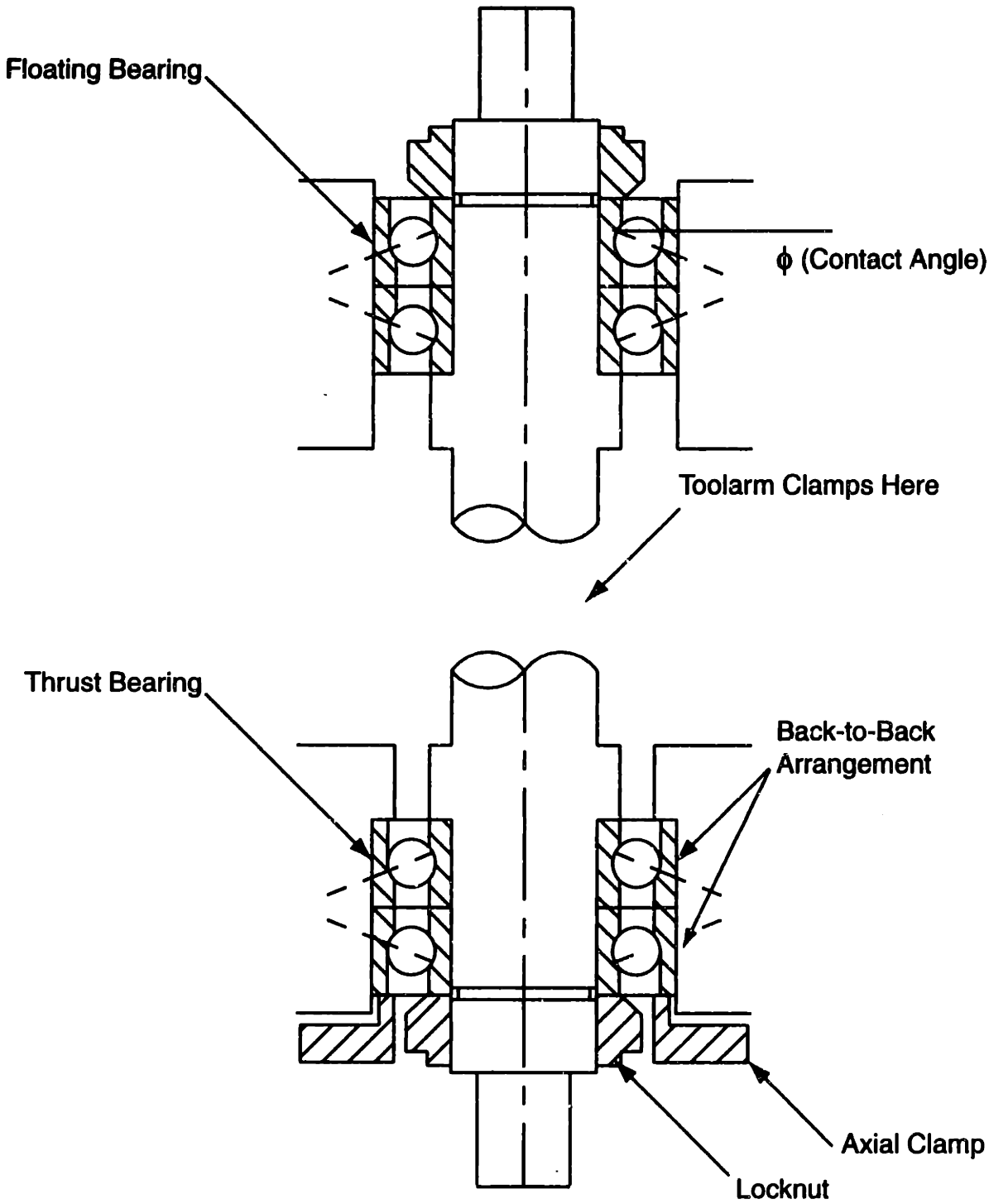

Figure 3-15: Cross-section of the bearing design.

Bearing Bore 18-30 mm	Bore Diameter (+.0000 to ...)	Raceway Radial Runout	Squareness of face	Raceway Axial Runout	Duplex Width (+.000 to ...)	Parallelism
	-.0002	.0001	.00005	.0001	-.01	.00005

Table 3.4: Inner ring tolerances of Series 200 ABEC 9 bearing, in thousandths of an inch. (Barden)

Preloading of the bearings is accomplished by clamping the inner races against the shoulders on the shaft by Bearhug locknuts, made by Whittet Higgins [9]. These locknuts are ground to ensure the squareness of the locknut face. Another feature of the locknuts is that they are self-locking. The threads deform when tightened to insure that they will not lose clamping force during operation.

In terms of load capacity, the Barden 205HDL bearings have radial, axial, and dynamic load capacities of 9963 N (2214 lbs), 9166 N (2037 lbs), and 14773 N (3283 lbs), respectively. Without preload and lubricated with grease, the bearings can be run at a maximum speed of 32,000 RPM. With a light preload, the maximum speed is 24,000 RPM. Preload increases the friction inside the bearing, decreasing the maximum operating speed. However, as shown before, for our application the speed of the tool arm shaft is on the order of 100 RPM. Also, the 100's of Newton loads we expect to see during cutting are much lower than the load ratings of the bearings.

Precision ball bearings are separated into different classes and given an ABEC number depending on the accuracy of the bearing manufacture. The higher the ABEC number, the more accurately the bearing's components have been manufactured. Typical machine tools use ABEC 5 bearings and precision spindles use ABEC 7 or 9 bearings. Table 3.4 shows ABMA Standard 4 and 20 and the ISO Standard 15 for an ABEC 9 bearing. Of particular interest to us are the tolerances for the radial and axial runouts, which cause error motions as the shaft rotates. According to the specifications, we should expect to see approximately 2.5 μm (0.0001 in) of error motion in the radial and axial directions over one revolution of the shaft. At first glance, these error motions appear to be too large to meet our requirement for sub-

[9]Whittet-Higgins Company, 35 Higginson Ave., P.O. Box 8, Central Falls, RI 02863, (800) 709-8790

micron error motions, especially considering that a fluid-static bearing could give us error motions of less than 25 nm. However, the angular excursion of the tool arm will be a small fraction of a full rotation. Therefore, the error motions within the functional range of the arm should be acceptable. We will discuss this in greater detail when we describe the testing of the bearings later in the chapter.

Back-to-back angular contact bearings are preloaded by clamping their inner races together. In our design, this is accomplished by press-fitting the bearings flush with the shoulders on the shaft and then tightening the locknuts. During manufacture, some defined amount of the inner race is ground away so that there is a gap between the inner races of the duplex set when the bearings are first assembled. The amount of the inner race that is ground away sets the magnitude of the axial preload. When this gap is closed by tightening the locknuts, the contact angle between the ball bearings and the races is established. For the 205 HDL bearing, light, medium, and heavy preloads for a 15° contact angle correspond to axial preloads of 67.5 N (15 lbs), 180 N (40 lbs) , and 360 N (80 lbs), respectively.

Preloading the bearings is extremely important because it closes radial and axial play between the balls and the races, increases the bearings' stiffness, and prevents skidding under high acceleration. Accuracy and resolution increases initially with preload for these reasons. However, as preload increases so does ball deflection, which reduces accuracy. Friction also increases, which decreases resolution. Typically, medium to heavy preloads are used for machine tools, where the loads on the bearings may be great enough that the bearings could easily lose preload. For our application, the most important requirement is high accuracy during the finishing cut of the lens, where we can take a shallow depth of cut to keep the cutting forces low. Therefore, we choose the lightest preload setting of the bearings, to insure any play in the bearings is eliminated and that accuracy and resolution are not sacrificed more than necessary.

Bearing fits are also extremely important. If the fit of the bearing inside the bearing bore is too loose, then the play between the two will lead to error motions during operation. Conversely, if there is too much interference between the bearing

and the housing, then forcing the bearings into the bore may warp the outer race and increase ball deformation and friction in the bearing. In extreme cases, excessive interference fits lead to premature failure. As noted in Table 3.4, the tolerance on the OD of the bearing bore is +0.0000 to -0.0002. Each bearing manufacturer will have slightly different specifications for the bearing bore diameter, but the thrust bearing should have a positive interference fit, and the floating bearing should have a running fit to allow for the outer race to move axially, to allow for thermal expansion. Neither bore should be so large that the outer race of the bearing will have clearance to wobble inside the bore. The Barden 205HDL has an OD of 52 mm (2.0472"). For the thrust bearing, we specify a fit of 2.0472 ± 0.0001", and for the floating bearing we specify a fit of 2.0475 ± 0.0001". A similar situation exists in the case of the shaft. There should be slight interference fits between the inner race of the bearing and the shaft to guarantee that there is no play between the two. Unlike the housing fits, the shaft fit can be the same for the thrust and floating bearings, because we do not desire any shaft movement with respect to the inner bearing race. The bore diameter of the 205HDL is 25 mm or 0.9843", and we specify fits of 0.9843 ± 0.0001 for both bearing seats.

3.3.2 Radial and Axial Error Motion of the Bearings

The techniques we use to measure the error motions of the bearings follow those given for measuring the error motion in spindles [1], [8], [18]. One of the difficulties of measuring the error motions of a rotary axis is separating the error motions of the axis from imperfections of the target. This separation can be done by using a technique called reversal. The basic procedure is shown in Figure 3-16. First, the sensor is fixed on a target. Then, the spindle is rotated a number of times and the runout of the spindle is recorded. The sensor measurement $V_1(\theta)$ contains the error motions of the spindle $E(\theta)$ plus the imperfections of the target $I(\theta)$.

$$V_1(\theta) = I(\theta) + E(\theta). \tag{3.32}$$

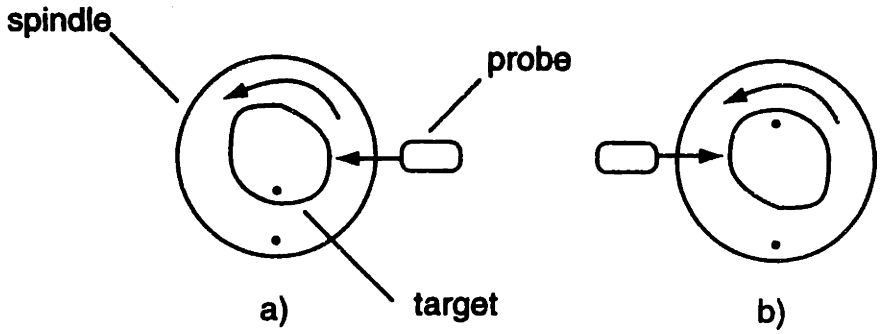

Figure 3-16: Demonstration of reversal, from [18].

Next, the target is rotated with respect to the spindle axis by 180° and the sensor is placed on the other side of the spindle. Now, the sensor measurement $V_2(\theta)$ includes the imperfections of the target $I(\theta)$ minus the error motion $E(\theta)$ of the spindle

$$V_2(\theta) = I(\theta) - E(\theta). \tag{3.33}$$

Subtracting $V_1(\theta)$ from $V_2(\theta)$ and dividing by two we obtain

$$\frac{V_1(\theta) - V_2(\theta)}{2} = E(\theta), \tag{3.34}$$

and we have separated the error motion of the rotary axis from the imperfections of the target.

In our test, we use the toolholder shaft as the target for the sensor, an ADE capacitance probe [10]. The index pulse of an 1100 count encoder attached to one end of the shaft marks the beginning and end of each revolution. After ten revolutions of the shaft, the shaft is rotated 180° with respect to the encoder shaft. Then, the sensor is placed on the opposite side, and the shaft is rotated another ten revolutions. Figure 3-17 shows a trace of the toolholder shaft's radial error motion over ten revolutions, after subtracting out the target error using eq. 3.34. Figure 3-18 shows the same trace as a polar plot. The peak radial error motion is approximately 0.8 μm. This is well within Barden's 2.5 μm specification for the radial error motion of the bearings.

[10] ADE Technologies Inc., 1525 McCandless Dr., Milpitas, CA 95035, (408) 935-4816

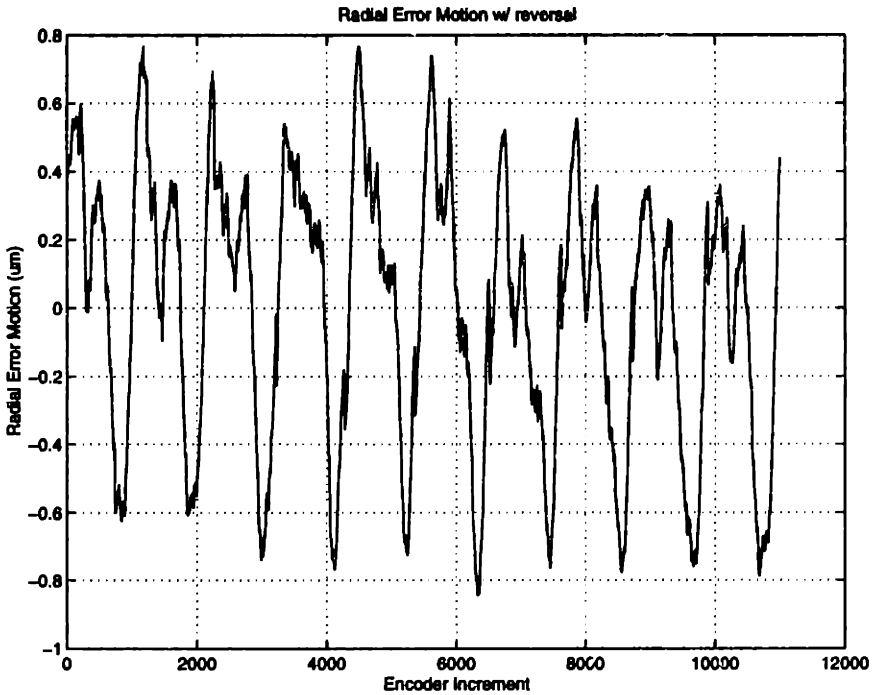

Figure 3-17: Trace of the radial error motion, after subtracting target error.

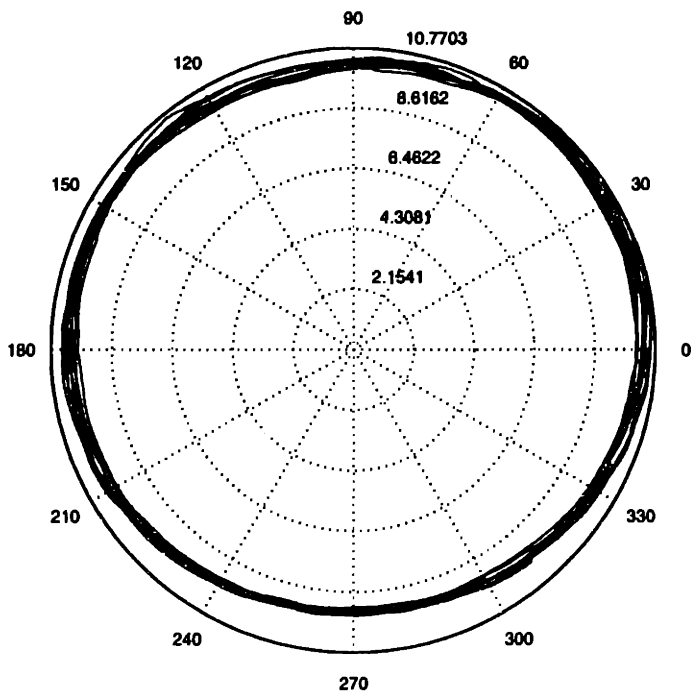

Figure 3-18: Polar plot of the radial error motion, after subtracting target error.

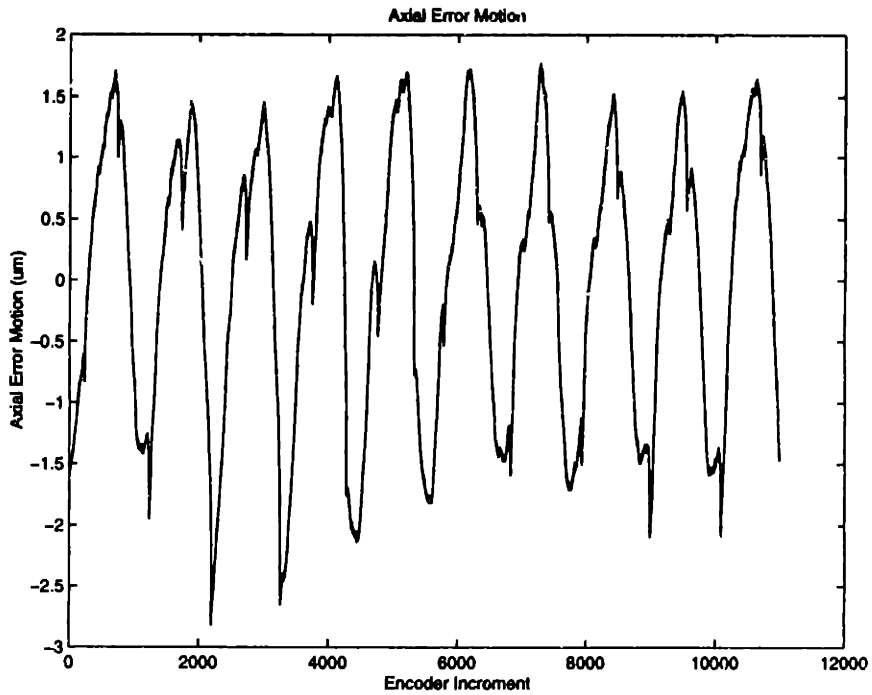

Figure 3-19: Trace of the axial error motion.

The sensor target for measuring the axial error motion of the bearings is a gageball mounted on a wobble plate, attached to the end of the tool arm shaft. The wobble plate is a kinematic mount for the gageball which clamps to the tool holder shaft via a flange. By adjusting the wobble plate, the gageball's axis of revolution can be moved to coincide with the tool holder shaft's axis of revolution. Figure 3-19 shows a trace of the toolholder shaft's axial error motion over ten revolutions, and Figure 3-20 shows the same trace as a polar plot. The peak axial error motion is approximately 2.8 μm. This is slightly larger than Barden's 2.5 μm specification for the axial error motion of the bearings. However, it is close enough to still be believable. While the axial error motion appears to be worse than the radial error motion, both are believed to be acceptable for our application. Consider again cutting an 8X10 toric lens where the linear travel of the tip is 1.26 cm. For a 100 mm arm, the angular travel is 0.126 rad, which corresponds to 2.0% of a full revolution. Thus, our working range occupies a fraction of the error motion trace for one revolution. In this case, 2% of the peak-to-peak radial and axial error motions would be, 0.03 μm and 0.1 μm, respectively. In addition, for most lenses, the axial errors are not in a particularly

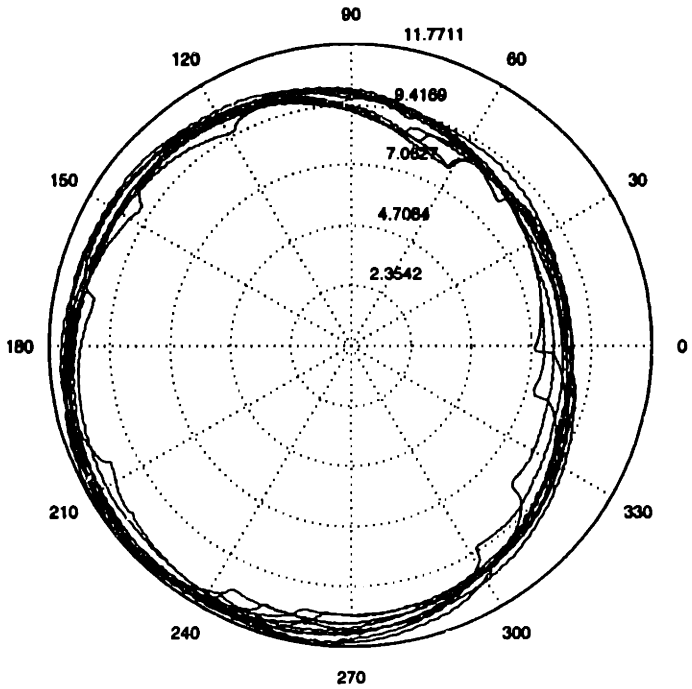

Figure 3-20: Polar plot of the axial error motion

sensitive direction.

3.3.3 Stiffness of the Bearings

During cutting, there is a significant vertical force exerted on the tool arm bearings, requiring the bearings to act as thrust bearings as well as radial bearings. As stated earlier, a heavy cut in polycarbonate generates a 200 N of force in the vertical direction. As shown in Figure 3-15, the line of contact between the races and the balls for an angular contact bearing is an angle ϕ from a plane orthogonal to the axis of rotation. The contact angle can be varied depending on the application. The greater the angle, the more thrust load the bearing can tolerate. For example, Barden angular contact spindle bearings have contact angles of 15° or 25°. Ball screw support bearings, which must handle large thrust loads, have a 45° contact angle.

The relation between bearing deflection and load is nonlinear because the contact area of the ball bearings varies with load. Unloaded, the bearing has the least stiffness because only a small portion of the ball is supporting the load. As the load increases and more of the ball bearing comes into contact with the races, the bearing's stiffness

also increases. To obtain stiffness estimates, not many sources give information on how to calculate the deflection of bearings as a function of load. In particular, bearing manufacturers do not usually provide information on how to calculate bearing stiffness. Again, [9] is very useful and we use the relations between bearing deflection and load developed there.

For an angular contact bearing, the radial deflection δ_r and axial deflection δ_a in millimeters, are

$$\delta_a = \frac{0.00044}{\sin\alpha}\left(\frac{Q^2}{D}\right)^{1/3} \tag{3.35}$$

$$\delta_r = \frac{0.00044}{\cos\alpha}\left(\frac{Q^2}{D}\right)^{1/3}. \tag{3.36}$$

The rolling element loads from an axial load Q_a and a radial load Q_r are

$$Q_a = \frac{F_a}{Z\sin\alpha} \tag{3.37}$$

$$Q_r = \frac{4.37F_r}{Z\cos\alpha} \tag{3.38}$$

- F_a Pure Axial Load
- F_r Pure Radial Load
- D Nominal Rolling Element Diameter
- α Contact Angle
- Z Number of balls

Note the nonlinear relationship between deflection and applied load, $\delta \propto Q^{2/3}$. Also, a pure axial force F_a loads all the balls equally, and the inner race shift due to the thrust load equals the deflection of the balls. However, a pure radial force loads the balls in the bearing unequally. This leads to an uneven load distribution, and the deflection of each ball bearing depends on its angular position from the applied radial load. To find the maximum rolling element load exerted requires an integral solution that sums all the rolling element loads. This is also covered in [9]. An easier rule of thumb as given in eq. 3.38, valid for pure radial loads and zero clearance

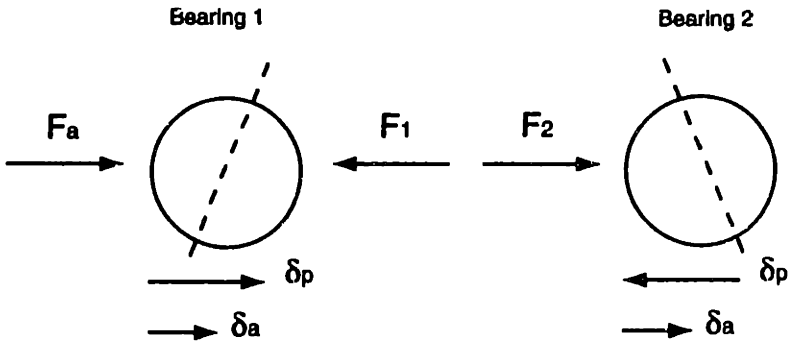

Figure 3-21: Effect of a thrust load on preloaded angular contact bearings.

between the bearing outer race and the bearing bore, is used. These relations for bearing deflections are approximate because under actual loading conditions, the contact angle changes as a function of load. However, they are sufficient to give us an estimate of the bearing stiffnesses. Figure 3-21 shows the effect of preloading angular contact bearings and then loading them with a thrust force. An axial preload F_p (not shown in the figure) on the bearings, causes a preload deflection δ_p of the ball bearings. This can be thought of as the new equilibrium point of the ball bearings. Now, we need to calculate δ_a the deflection on both bearings from an additional load F_a. From geometry, the deflections δ_1 and δ_2 of bearing 1 and bearing 2 are

$$\delta_1 = \delta_p + \delta_a, \tag{3.39}$$

$$\delta_2 = \delta_p - \delta_a. \tag{3.40}$$

A thrust force in the direction shown in Figure 3-21 further loads bearing 1 and at the same time acts to unload bearing 2. Balancing the forces, we see that

$$F_a = F_1 - F_2, \tag{3.41}$$

where F_1 and F_2 are the load forces on bearing 1 and bearing 2, respectively. To find δ_a resulting from F_a we follow these steps:

1. Find the deflection δ_p from the preload force F_p from eqs. 3.35 and 3.37.

2. We assume a value for δ_a and from eqs. 3.39 and 3.40 find δ_1 and δ_2.

3. Combining eqs. 3.35 and 3.37, we can solve for the load force F_i on the bearing when it is deformed by an amount δ_i,

$$F_i = D^{1/2} Z (\sin\alpha)^{5/2} \left(\frac{\delta_i}{0.00044} \right)^{3/2}. \tag{3.42}$$

With eq. 3.42 we can solve for F_1 and F_2.

4. Finally, from eq. 3.41 we can solve for the axial load force F_a.

Radial loads do not act to unload the preload of the bearings. Also, both the thrust and floating bearings act to resist radial loads. Therefore, any applied radial loads F_r will be divided by four, the number of angular contact bearings. To calculate the deflection δ_r from a pure radial force we follow these steps:

1. We again start from the equilibrium where the balls are preloaded, and the rolling element load from eq. 3.37 is Q_p. The radial deflection δ_r from the preload can be found from eq. 3.36.

2. From eq. 3.38 the rolling element load Q_r from a radial load force F_r can be found.

3. The total rolling element load is now $Q_p + Q_r$, and eq. 3.36 can be used to find the total deflection.

3.3.4 Testing bearing stiffness

Bearing catalogs typically show a plot of axial and radial deflection versus load for one of their bearings. To see how accurately we can predict bearing deflection as a function of force, we compare the actual deflections found by the bearing manufacturer and compare them to the deflections we predict using the procedure detailed in the previous section. Barden gives the deflection vs. load curve for their 114HDB bearings. These are ball bearings with a 15° contact angle, a bore size of 70 mm, and a ball complement of 18, 12.5 mm diameter balls. Light, medium, and heavy preloads

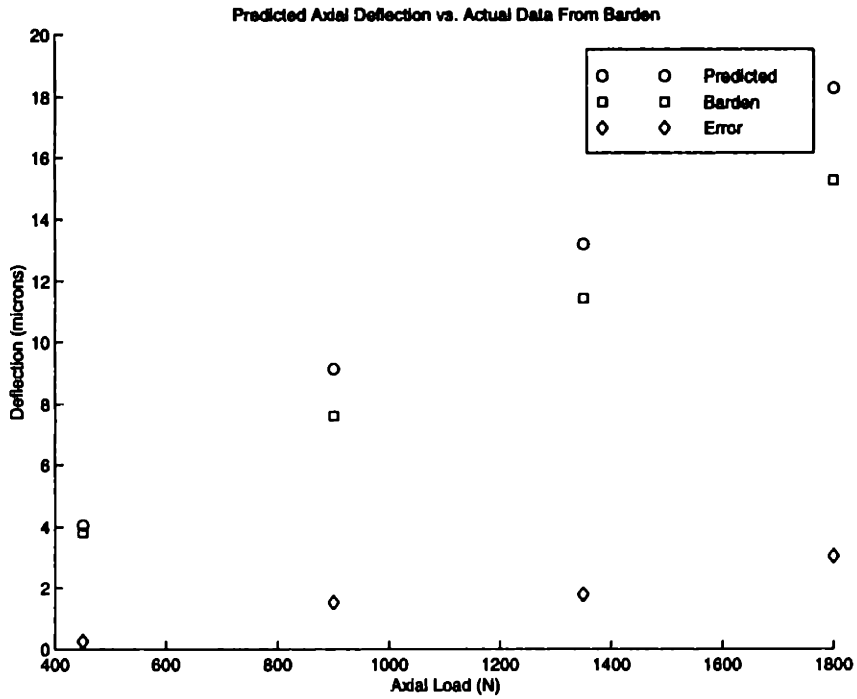

Figure 3-22: Axial deflection of the HDB114 bearings.

are 65, 160, and 320 lbs., respectively. Figures 3-22 and 3-23 shows the actual deflections from axial and radial loads of 450 (100), 900 (200), 1350 (300), and 1800 N (400 lbs), for back-to-back bearings with medium preload, taken from the Barden's experimentally determined stiffness curves. Also shown are the deflections predicted from the techniques outlined in the previous section. Keeping in mind that we are using equations that approximate bearing deflections and comparing them to experimental data, the agreement between the predicted and actual deflections is fairly good. The

Axial Load (lb.)	Predicted (in.)	Barden (in.)	Error	% Error
100	0.00016	0.00015	0.00001	7
200	0.00036	0.0003	0.00006	20
300	0.00052	0.00045	0.00007	16
400	.00072	0.0006	0.00012	20
Radial Load	Predicted (in.)	Barden (in.)	Error	% Error
100	0.00005	0.00003	0.00002	67
200	0.00009	0.00006	0.00003	50
300	0.00013	0.0001	0.00003	30
400	0.00017	0.00013	0.00004	31

Table 3.5: Comparison of actual and predicted deflection for the Barden 114HDB bearing.

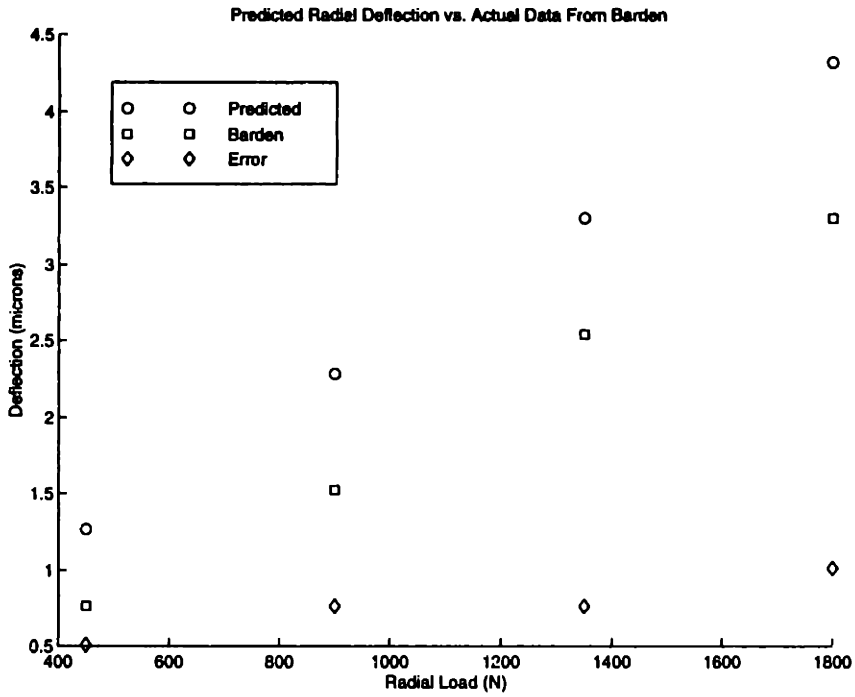

Figure 3-23: Radial deflection of the HDB114 bearings.

error between the actual and predicted deflections for axial loading is no greater than 20%. For radial loading, the largest error is higher, 67%, because overall deflections are much lower. More importantly, the slopes of the curves, which correspond to bearing stiffness, are very close. In other words, we are able to predict how much the bearing will deflect after the initial preload. As a quick means of estimating bearing deflection and stiffness, the method outlined above appears to be valid.

To determine whether ball bearings had the required stiffness for our application, the axial stiffness of the testbed bearings, Barden 204HDL, were tested. These are angular contact bearings with a contact angle of 15° and 10, 5/16" diameter balls. The preload levels are 67.5 (15), 40 (180), and 360 N (80 lbs.). Figure 3-24 shows the calculated deflection of the thrust bearings as a function of applied axial load. When one of the bearings in the back-to-back arrangement loses preload, the other bearing resists all of the thrust load. The deflection curve then has the same characteristics as an unpreloaded bearing. A general rule of thumb is that the bearing will lose preload when the applied axial load is three times greater than the preload. This metric is cited in Barden's bearing catalog, and is also found to be true in our calculations.

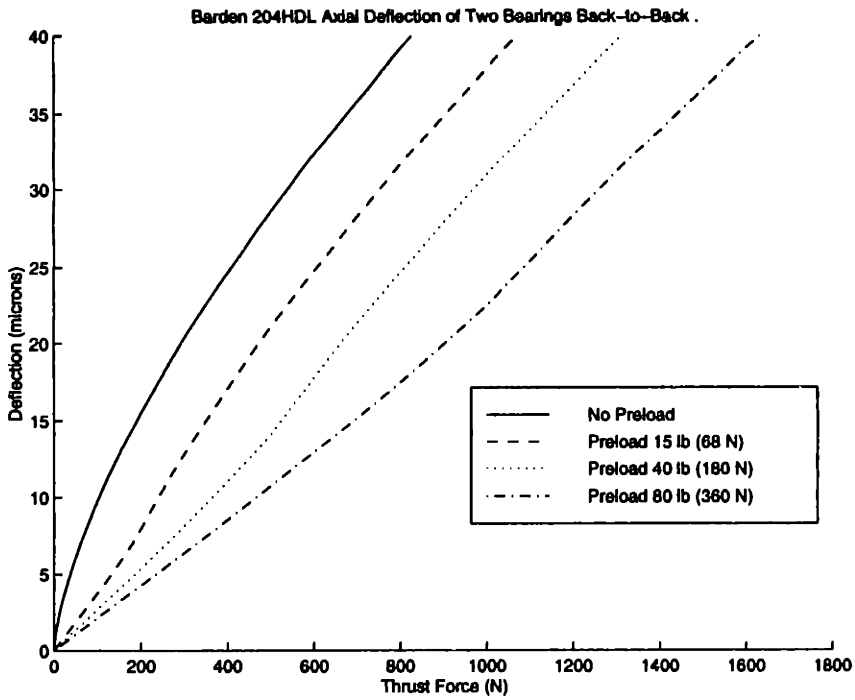

Figure 3-24: Axial deflection vs. load force.

The point of unloading for each level of preloading can be seen in Figure 3-24. The deflection curve for the unpreloaded bearing starts very steeply as an axial load is applied. As we mentioned before, this is because the contact area between the ball bearings and the races is very small. As more load is applied, the deflection curve levels off and additional loading causes less deflection. Hence, one of the benefits of preloading is that the initial deformation of the ball bearings loads the balls such that their deflection curve starts past the initial knee, where the balls are extremely compliant. Although the relationship between deflection and load is nonlinear, after the bearings are preloaded, the relationship between deflection and load has a reasonably constant slope, until one of the bearings loses preload.

Figure 3-25 shows the deflection curve of the thrust bearing over a smaller range of loads. As mentioned previously, we expect the largest vertical forces in our application to be approximately 200 N. From this graph, we can more easily extrapolate the expected stiffness of the thrust bearing in its operating range. Over a range of 0 to 100 N, the approximate axial stiffness of a bearing with no, light, medium, and heavy preloads is 10, 25, 36, 50 N/μm, respectively. We have specified a light preload, but

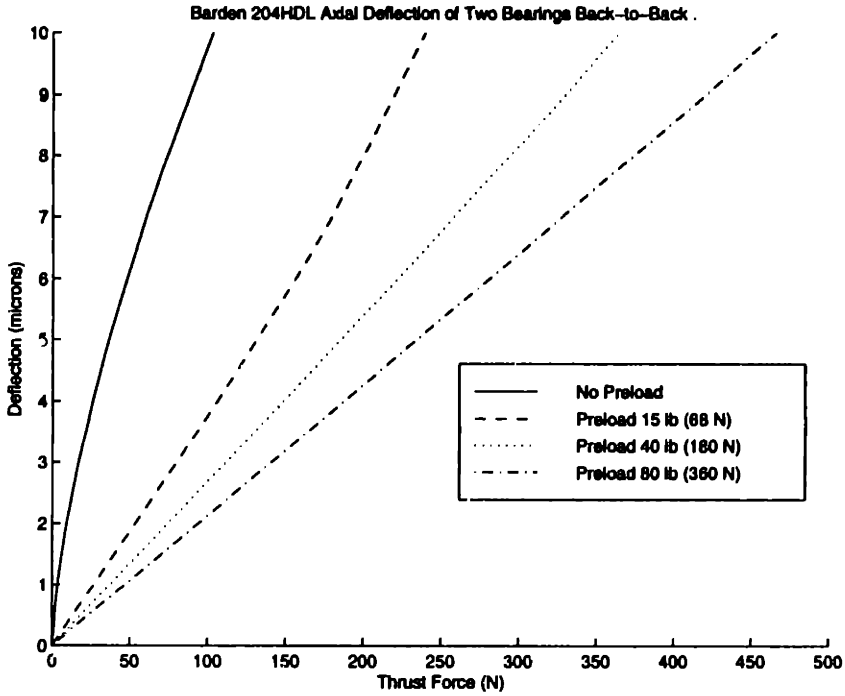

Figure 3-25: Axial deflection vs. load force, closeup.

interference fits will probably increase the preload.

Figure 3-26 shows the deflection curves for a radial load. In the range of 0 to 100 N, the approximate radial stiffness of the bearings with no, light, medium, and heavy preloads is 140, 210, 260, and 310 N/μm, respectively. The radial stiffness of the bearings is much higher for two reasons. First, the contact angle of the bearing is only 15°. Thus, the line of contact running through the bearings is more aligned to resist radial loads. Second, all four bearings are contributing to the stiffness of the system.

To test the axial stiffness of the bearings, we mount the bearing housing vertically and load the bearings by placing weights on one end of the shaft. The other end of shaft, with the wobble plate attached to it, is used as the target for an ADE capacitance probe, which records the displacement of the shaft from the load. For loads of 22.5 N (5 lbs.), 45 N (10 lbs.), and 67.5 N (15 lbs.) the axial displacement is shown in Figure 3-27. In the range of our load forces, which correspond to loads seen from light roughing passes in polycarbonate, the static stiffness of the bearings is approximately 90 N/μm. Finishing passes will load the bearings more lightly. For

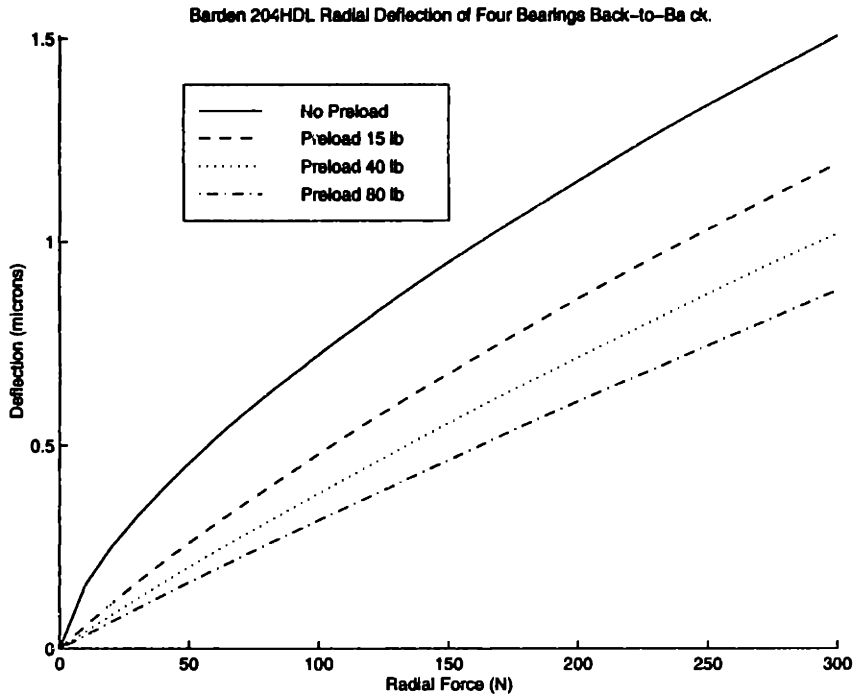

Figure 3-26: Radial deflection vs. load force.

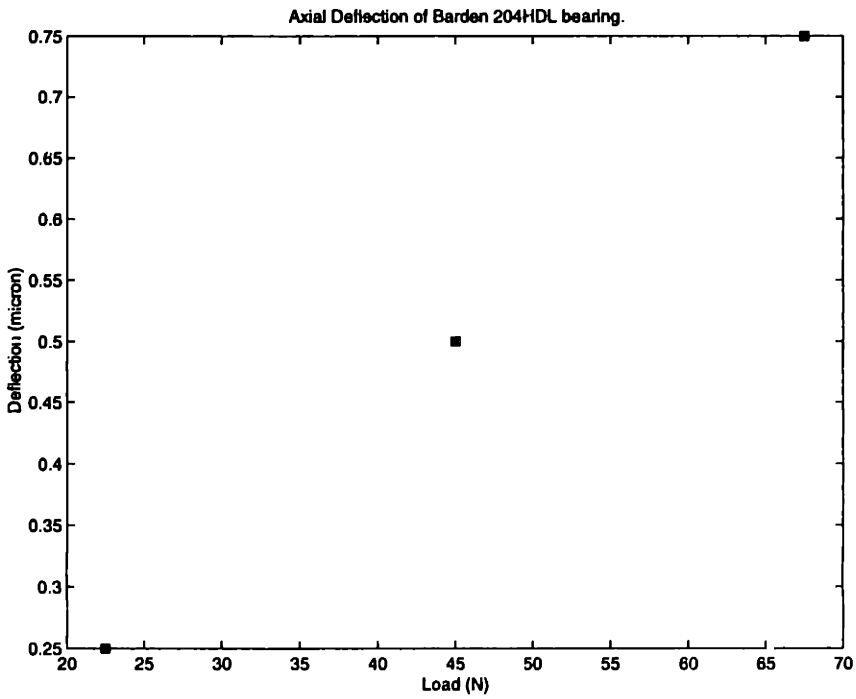

Figure 3-27: Experimental axial deflections from static loading.

light and medium preloaded bearings, we predicted axial stiffnesses of 25 and 36 N/μm. As mentioned before, while we have specified a light preload, we also expect the interference fits on the tool arm shaft and bearing housing to increase the preload of the bearings. However, the actual stiffness is still approximately twice the axial stiffness for medium preloaded bearings. One reason for this might be that the loading is light enough that the fit on the floating bearings keeps them in place for thrust loads. Thus, they share in carrying the load in this experiment.

3.3.5 Resolution of the Bearings

The resolution limit of the rotary fast tool servo is a combination of many factors, including static friction in the bearings, positioning noise as a result of A/D, and D/A quantization, and other system noise. Therefore, a test of the achievable resolution of the bearings is not a test of the positioning resolution of the fast tool servo. However, it is an indication of whether the bearings will be the limiting factor of achievable resolution. To determine the resolution of the bearings used in the testbed, we have the tool arm shaft track a square wave under closed-loop control. As we decrease the amplitude of the square wave, at a certain point the torque commanded by the controller is not enough to overcome static friction in the bearings. To close the loop, an analog phase-lead controller with a bandwidth of 60 Hz is used. By using an analog controller, we eliminate A/D and D/A quantization. The input to the system, a square wave with a frequency of 4 Hz, is supplied by a function generator. When measuring the angular position of the toolholder shaft, the signal given by the servopot is prefiltered by a 5 Hz lowpass filter and then amplified by a Tektronix differential amplifier [11]. Figure 3-28 shows a series of 20 μrad steps, which corresponds to 2 μm of linear motion at the end of a 100 mm arm. The deviation in position is on the order of 2.5 μrad, which corresponds to 0.25 μm at the tooltip. Currently, the limiting factor of this test appears to be the resolution of the servopot, which should be improved when we install a high resolution encoder.

[11] Tektronix Inc., P.O. Box 500, Mail Stop 63-814, Beaverton, OR 97077, (503) 627-7111

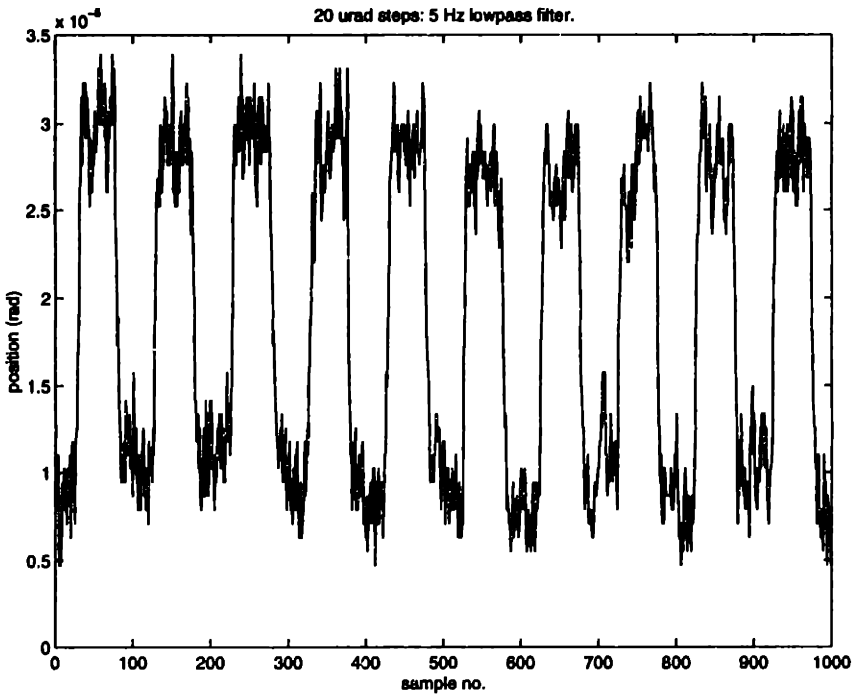

Figure 3-28: Output of servopot showing 20 μrad steps.

3.4 Flexible Coupling Selection

Finding a suitable flexible coupling to join the motor and the tool arm shaft has been more difficult than expected. The requirements for the coupling are,

- Place the torsional mode of resonance in the axis above 1 kHz.
- Allow minor misalignment of the tool arm shaft with respect to the motor shaft.

The second requirement is obvious for the flexible coupling. The bearings for the tool arm shaft are much stiffer than the bearings for the motor shaft, and a solid coupling between the motor and tool arm shafts would be impose an overconstraint and eventually cause the motor bearings to fail. The first requirement is much more difficult to satisfy. Many of the commercial flexible couplings surveyed do not have adequate torsional stiffness for our application. Typical couplings include one piece helical couplings, couplings with bellows, and couplings with rigid pieces joined by flexible springs. In general, one piece helical couplings are the least stiff, while torsional stiffnesses quoted for bellows couplings are the highest. As we hope to achieve

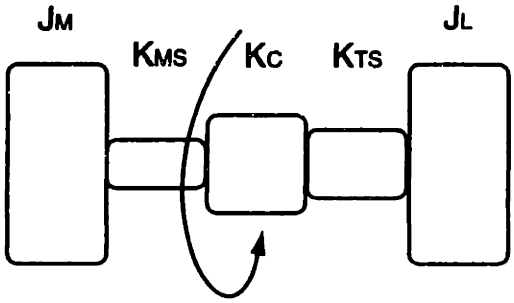

Figure 3-29: Model of the distributed compliances in the RFTS axis.

very high bandwidths on the RFTS axis, resonances at low frequencies have to be avoided.

Figure 3-29 shows a model of the distributed compliances in the system. In essence, we are modeling the system as two rotational inertias coupled by three torsional springs in series. In Figure 3-29, J_M and J_L are the inertias of the motor and the load, respectively. The load inertia includes the inertias of the coupling, the tool arm shaft, and the tool arm. The three torsional springs are K_{MS}, K_C, and K_{TS}, the stiffnesses of the motor shaft, the flexible coupling, and the tool shaft, respectively. The compliance of the motor shaft comes from the free length of the shaft starting from the motor armature and ending at the flexible coupling. Since we cannot measure this directly, we assume a length of 1 inch. Likewise, the compliance of the tool arm shaft starts at the flexible coupling and ends where the tool arm is clamped to the shaft. This length is approximately 2 inches. The stiffness, the inverse of the compliance, of a uniform shaft in Nm/rad is

$$K = \frac{T}{\theta} = \frac{JG}{L}, \tag{3.43}$$

where $J = \frac{\pi}{2} r^4$, is the rotary inertia of the free length L, and G is the shear modulus of the material, which is approximately 80 GPa for steel. The total equivalent stiffness K_T can be found by

$$\frac{1}{K_T} = \frac{1}{K_{MS}} + \frac{1}{K_C} + \frac{1}{K_{TS}}. \tag{3.44}$$

Now, the resonant frequency of the axis f_n in Hz is

$$f_n = \frac{1}{2\pi}\sqrt{\frac{K_T(J_M + J_L)}{J_M J_L}} \tag{3.45}$$

While working on the testbed, we are using a ZeroMax SC-050 flexible coupling with a stiffness K_C of 20,000 Nm/rad and an inertia of 1.42E-4 kg-m^2 [12]. ZeroMax couplings are basically three aluminum cylinders separated by metal discs. The two shafts to be joined fit into the two outer cylinders. The metal discs flex to allow some misalignment of the shafts, but are rigid in torsion. The Aerotech motor shaft has a 0.75" diameter. Assuming a free length of 1", $K_{MS} = 40,296$ Nm/rad. For the testbed, the tool arm shaft has a diameter of 0.75". Assuming a free length of 2", $K_{TS} = 20148$ Nm/rad. Substituting into eq. 3.44, $K_T = 8035$ Nm/rad. In our series of tests, the load was the tool arm shaft and the flexible couplings, including the coupling joining the tool arm shaft to the servopot. The estimated load inertia $J_L = 3 \times 10^{-4}$ kg-m^2. From Table 3.1, the Aerotech motor has an inertia $J_M = 5.6 \times 10^{-4}$. Therefore from eq. 3.45, $f_n = 1018$ Hz. However, f_n is also expected to drop to 807 Hz when we add the tool arm, which adds an inertia of 4.14×10^{-4} kg-m^2 to J_L.

This expected resonance is lower than what was specified in our design parameters for the coupling, because at first we underestimated the compliance of the motor shaft and tool arm shaft. Even still, when measured the stiffness of the ZeroMax coupling is much less than what is quoted. Figure 3-30 shows the power spectral density of the tool arm position when the torsional mode of resonance is excited. The frequency of the resonance is 482 Hz, which is significantly lower than our prediction of 1018 Hz. To increase the stiffness of the coupling we remove the middle cylinder, effectively leaving just the two cylinders into which the shafts are inserted and the metal discs in between. This appeared to help significantly and our resonance is moved up to 826 Hz, as shown in Figure 3-31. However, the coupling still does not perform as well as expected.

[12] Zero-Max, Inc., 13200 Sixth Ave., N., Minneapolis, MN 55441-5509, (800)533-1731

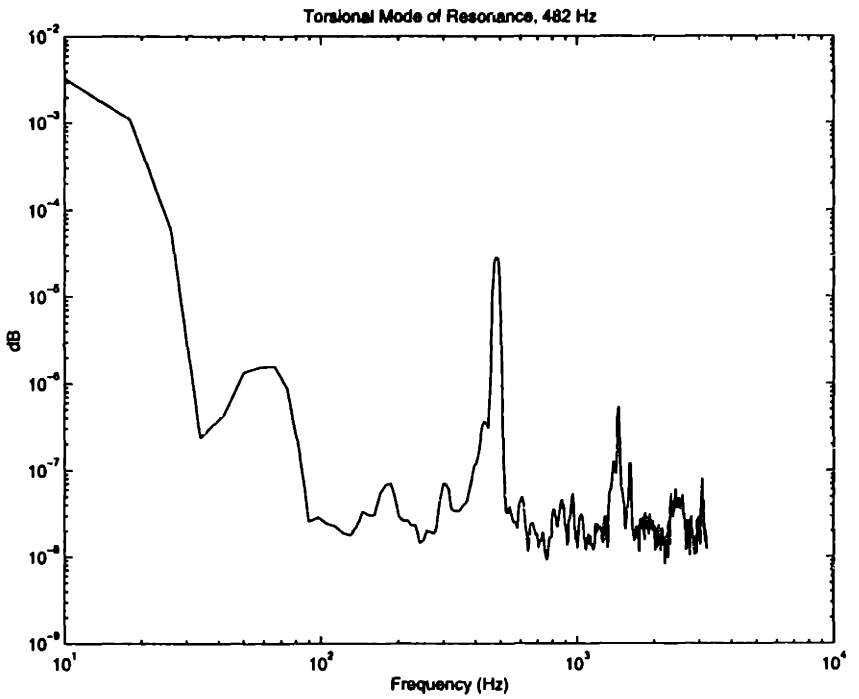

Figure 3-30: Power Spectral Density of tool arm position showing resonance at 482 Hz with ZeroMax coupling.

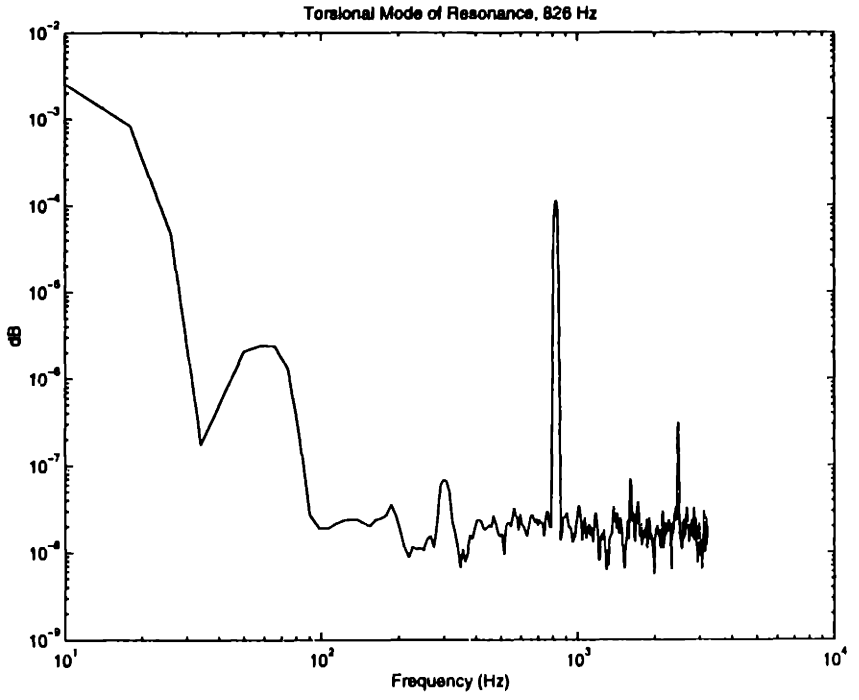

Figure 3-31: Power Spectral Density of tool arm position showing resonance at 826 Hz with modified ZeroMax coupling.

For the prototype RFTS axis, we are using a bellows-type coupling, the KR-65 from Gam Jakob [13]. Currently, it is installed on the prototype machine with the testbed bearings. The KR-65 is a one piece coupling, unlike the Zero-Max coupling. There is a single corrugation, essentially a fold in the coupling that allows it to bend, at each end of the coupling. The bellows allow for lateral and angular misalignments of 0.006" and 1°, respectively. In general, these couplings, while more expensive, have much higher torsional stiffnesses. They differ from the spring disc couplings in that the torsional rigidity comes from the entire coupling rather than from metal spring discs. The KR-65 has a quoted torsional stiffness $K_C = 48000$ Nm/rad. Again, assuming $K_{MS} = 40,296$ Nm/rad and $K_{TS} = 20,148$ Nm/rad, $K_T = 10434$ Nm/rad and the resulting $f_n = 921$ Hz. This prediction agrees well with the resonant frequency of 910 Hz that we measure on the prototype machine. Once the new bearing structure is installed and the tool arm shaft's diameter increases to 1", which increases K_{TS} to 60392 Nm/rad, f_n is expected to increase to approximately 1141 Hz.

Part of the work on the testbed involves trying to damp the torsional mode of resonance by adding damping to the Zero-Max coupling. To damp the flexing of the metal discs, we place Isodamp, a damping material from EAR, between the metal discs [14]. This helps damp the resonance, but separating the discs with the Isodamp material also makes them buckle under high torsional loads, such as when the tool arm is driven at high frequencies. Filling the coupling with either silicone or Moretight does not help appreciably. Moretight is commonly used as insulation around windows in houses. It also seems to be a good damping material, but we believe that it does not flex with the metal discs and thus does not damp the torsional mode of resonance.

Since the Gam Jakob coupling is a one piece coupling and the torsional rigidity comes from the middle shell, damping the Gam Jakob coupling by means of a constrained layer damping might be more effective. An example of this would be adding damping material inside a sheet of metal shim around the coupling. This would be the equivalent of adding damping material between the metal discs of the Zero-Max

[13]Gam Enterprises, Inc., 7333 W. Wilson Ave., Chicago, IL 60656,(800)841-1293

[14]E-A-R Specialty Composites, 7911 Zionsville Rd., Indianapolis, IN 46268-1650, (317) 692-1111

coupling, but in this case it should not affect the mechanical properties of the coupling. Another option is to actively damp the coupling, which will be the topic of future research on the testbed but is not covered in this thesis.

3.5 Overview of Rotary Sensors

One requirement of the RFTS is to find a high accuracy, high resolution, low inertia rotary sensor. Specifically, the requirements for the rotary sensor are,

- Angular accuracy on the order of 10 μrad. For a 100 mm rotary arm, positioning the tip to within 1 μm accuracy corresponds to the sensor having an accuracy of approximately 10 μrad.
- Angular resolution an order of magnitude greater than the accuracy, approximately 1 μrad.

At first, we considered using a rotary capacitive sensor for the RFTS axis. As an example, General Scanning uses a rotary capacitive sensor in their galvanometers [15]. These are limited-range sensors used in optical scanning, an application where the scanning motion is similar to the motion of the RFTS axis. The working principle of this sensor is that it measures the change in capacitance between the sensor's rotor and stator. To accomplish this, the sensor's rotor has a butterfly shape. Thus, as the rotor rotates with respect to the stator, the capacitance between the rotor and stator changes, giving us a means of measuring the angular position of the rotor. This type of sensor seems particularly attractive because the end of the tool arm shaft can be machined to the required shape. The sensor stator can then be a cap around the end of the shaft. In addition, this would add little or no inertia to the RFTS. Initial tests also showed that the sensor's resolution is close to our needs. However, one worry is whether we are be limited by a 16 bit A/D converter. As an example, over an angular travel of 20°, 16 bits of resolution would give us 5 μrad of resolution, which is most

[15] General Scanning Inc., 500-T Arsenal St., P.O. Box 307, Watertown, MA 02272, (617) 924-1010

likely too coarse for our application. Also, the sensor would not be an off-the-shelf item. While, developing the sensor would not be extremely difficult, we decided it would be easier to use a sensor with less development time associated with it.

Companies that make encoders with resolutions high enough for our application include, MicroE, Heidenhain, Hewlett-Packard, and Canon. Table 3.6 shows some of the characteristics of high-resolution encoders from these companies. Heidenhain makes standard optical encoders with a diffraction grating on the encoder disk. While its resolution is adequate, the encoder disk has a diameter of 200 mm, which is obviously too large for our application. MicroE, Hewlett-Packard, and Canon make laser encoders which also have diffraction gratings on the rotating disk. These encoders take advantage of diffraction effects to achieve high resolution. The intensity of the interference fringes, from passing a laser through the diffraction grating, modulate as the disk is rotated. Sine and cosine outputs are generated and interpolated to give the angular position of the disk. A more detailed explanation of laser encoders and conventional optical encoders is provided in [16].

Currently we are installing a high resolution encoder donated by MicroE onto the prototype machine. [16]. This work is primarily the work of another M.S. student, David Chargin. The MicroE encoder's diffraction grating has a 20 μm pitch, which gives a fundamental resolution of approximately 15000 counts per revolution. The sine and cosine waves can be used to interpolate the fundamental resolution by x4096 to give a final resolution of 0.1 μrad. From its specifications, the MicroE encoder appears to meet our requirements. The other encoders may also be suitable, but we are evaluating the MicroE encoder primarily because it is available and free of cost to the research project. The HP encoder is distinctive because the glass scale is only a section of a full disk and must be mounted at a specified diameter. While its resolution is excellent, 0.016 μrad, it might be difficult to mount accurately. The maximum speeds of all the high resolution encoders are low because of the time required for interpolation, but we should be high enough for our application.

[16]MicroE Inc., 130 A Street, Needham Heights, MA 02194, (617)455-1414

Encoder	Diameter (mm)	Resolution (μrad)	Max. Speed (RPM)	cost ($)
MicroE	50	0.1	289	3000
Heidenhain RON 800	200	.89	67	5900
HP E1710A	NA	0.016	212	5346
Canon X-1M	36	7	180	19000

Table 3.6: Comparison commercial high-resolution encoders.

	Diameter (mm)	Resolution (μrad	Max. Speed (RPM)	cost
Inductosyn	300	5	360	7000

Table 3.7: High-resolution inductosyn made by Farrand.

Inductosyns, made by Farrand, are another type of rotary sensor. Also noncontact sensors, they use inductive coupling between two windings to generate a sinusoidal signal [17]. The signal can be used to find angular position in a manner similar to optical encoders. The windings are printed onto the stator and rotor of the sensor much like circuits patterns are printed on printed circuit boards. The pitch of the windings determines the fundamental resolution of the Inductosyn. An AC excitation in one winding will induces a voltage in the second winding. The amplitude and phase of the induced voltage changes sinusoidally as the windings are rotated relative to one another. A second winding, 90° out of phase with the first winding, gives a cosine signal. Also similar to optical encoders, the sine and cosine signals can then be interpolated for finer angular resolution. One advantage of Inductosyns is that they are extremely rugged and resistant to harsh conditions such as dust and oil. Inductosyns are also covered in [16]. A disadvantage of Inductosyns is that to obtain high resolution requires a large rotor diameter, which leads to having a large rotary inertia. Presumably, this limitation comes from how small the pitch of the winding can be made. The high-resolution inductosyn we show in Table 3.7 has a diameter of 300 mm. Hence, for now it appears the best choice of rotary sensors are laser encoders such as the MicroE encoder that we will be using in the project.

[17]Farrand Controls, Div. Of Ruhle Companies Inc., 99 Wall St., Valhalla, NY 10595, (914) 761-2600

Chapter 4

Second-Generation Bearing Structure Design

In this chapter we describe the design and fabrication of the second-generation RFTS bearing structure. For the second-generation design, our goal is to bring all the components from the RFTS testbed and fix their location on the prototype machine. In the following sections, we first describe the second-generation design. Afterwards, we detail the fabrication of the second-generation bearing structure. The experience gained from building the bearing structure is useful when evaluating the design for a production machine.

4.1 Design of the Second-Generation Bearing Structure

The criteria of the bearing structure are,

- Allow for the kinematics of cutting a lens.
- Minimize the effect of machining and misalignment errors on the cutting accuracy of the RFTS, by properly referencing features on the bearing structure.
- Be structurally stiff and well-damped.

- Be easy to manufacture.

In terms of kinematics, the design of the bearing structure must allow the tool arm sufficient travel to cut all of the lens prescriptions. Minimizing machining and misalignment errors is also critical. Whereas in the testbed we wanted flexibility in locating the components of the RFTS, for the second-generation design we want all the components to be referenced accurately. In other words, we want to be able to place the components deterministically. For example, since the squareness of the tool arm shaft with respect to the machine base is important, we want that alignment to be within a specified geometric tolerance. In order for the structure to be stiff and well-damped, we want to insure the bearing housings are well-supported. This lead us to design the structure to be one piece, or monolithic. A monolithic structure also aids us in referencing features on the bearing structure. Ease of fabrication is also an issue. Since we want the bearing structure to be buildable within a reasonable time frame, we want to avoid a complex design that is difficult to manufacture. This also has implications on the future of the prototype machine. The simpler we make the design now, in terms of manufacturability, the more useful it becomes when evaluating the prototype machine's future as a production machine.

Figure 4-1 shows the second-generation bearing structure. Functionally, it is very similar to the testbed bearing structure. One major improvement is that the bearing housings are supported on two sides rather than being cantilevered as in the testbed bearing structure. In a conservative analysis, modeling each bearing housing as a beam, both sides of the housings are simply supported rather than being cantilevered. This makes the entire structure much stiffer. As described previously, two sets of back-to-back ABEC 9 bearings are housed in the top and middle levels of the structure. The servomotor, attached to a faceplate, bolts onto the ledges near the bottom level of the structure. Datum planes A,B,C, which are ground surfaces, are used to reference all of the machined features on the bearing structure. Datum A mates with the machine base and defines the squareness of all the structure's features, with respect to the Moore Tool surface plate. Datum B is the side datum plane and Datum C is the front datum plane. A relief is specified on Datum B such that the surface grinder

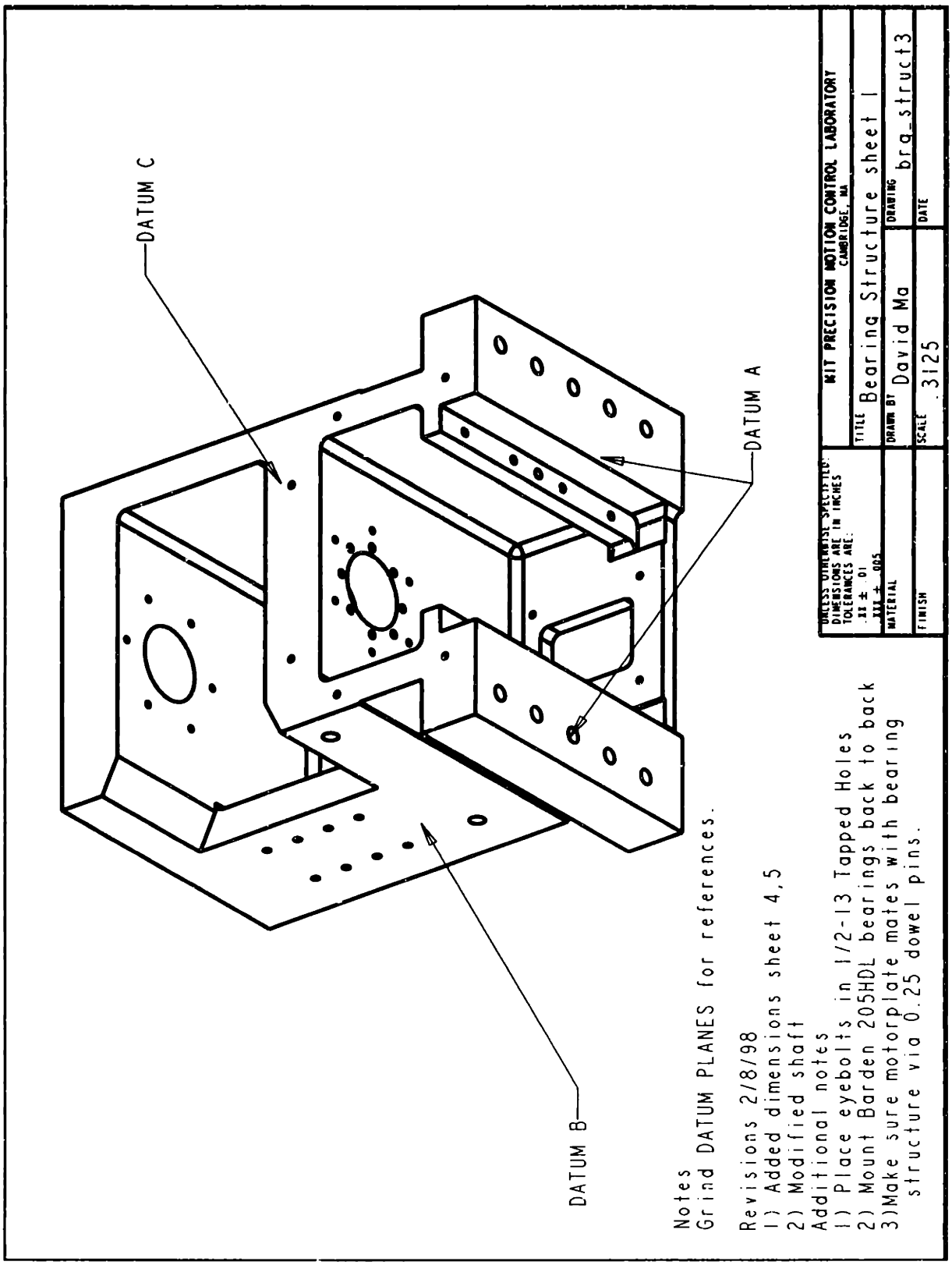

Figure 4-1: Drawing of the second-generation bearing structure.

that grinds the datum can clear the structure's feet.

Figure 4-2 shows the bottom view of the structure. The primary feature we show in this view is the bearing bore for the thrust bearings which has a diameter of 2.0472 ± 0.0001". As mentioned in the previous chapter, this is a slight interference fit on the outer races of the bearings. The axial clamp for the thrust bearings bolts into the eight, 1/4-20 tapped holes located on a 2.5" circle around the bore. Six, 10-32 tapped holes on a 3.5" circle around the bore can be used attach seals for the bearings. Should it become necessary, a fluid damper to damp vibrations in the vertical direction can be built. One possibility is to use the holes to bolt on a flat surface to be used as part of a squeeze film damper. The opposing part of the fluid damper would be attached to the tool arm shaft. Unfortunately, the holes were not actually machined by the machine shop. To compensate for this, we may epoxy a plate around the bearing bore with tapped holes to give us this extra functionality. The motor's faceplate bolts into the eight, 1/4-20 tapped holes on the ledges near the structure's feet. Dowel pins, press-fitted into the motor faceplate, slide into the two 0.251" reamed holes. This accurately locates the motor with respect to the tool arm shaft. The flexible coupling between the two compensates for minor misalignments. Figure 4-3 shows the axial clamp which helps constrain the thrust bearings in the vertical direction by clamping against the bearings' outer races. Buttonhead screws are used to bolt on the axial clamp. The heads of the screws are countersunk to reduce chance of interference with the flexible coupling.

Figure 4-4 shows the top view of the structure. This view shows the bearing bore for the floating bearings, which has a diameter of 2.0475 ± 0.0001". Since we want these bearings to be able to move within the bearing housing, the fit within the housing is looser than what is specified for the thrust bearings. Tapped holes on top of the bearing structure allow for components of a rotational sensor, such as the MicroE encoder readhead, to be bolted directly onto the structure. The entire structure bolts onto the Moore Tool surface plate via the five through holes on each foot.

Figure 4-5 shows cross-section of the structure. In this view we show the design of

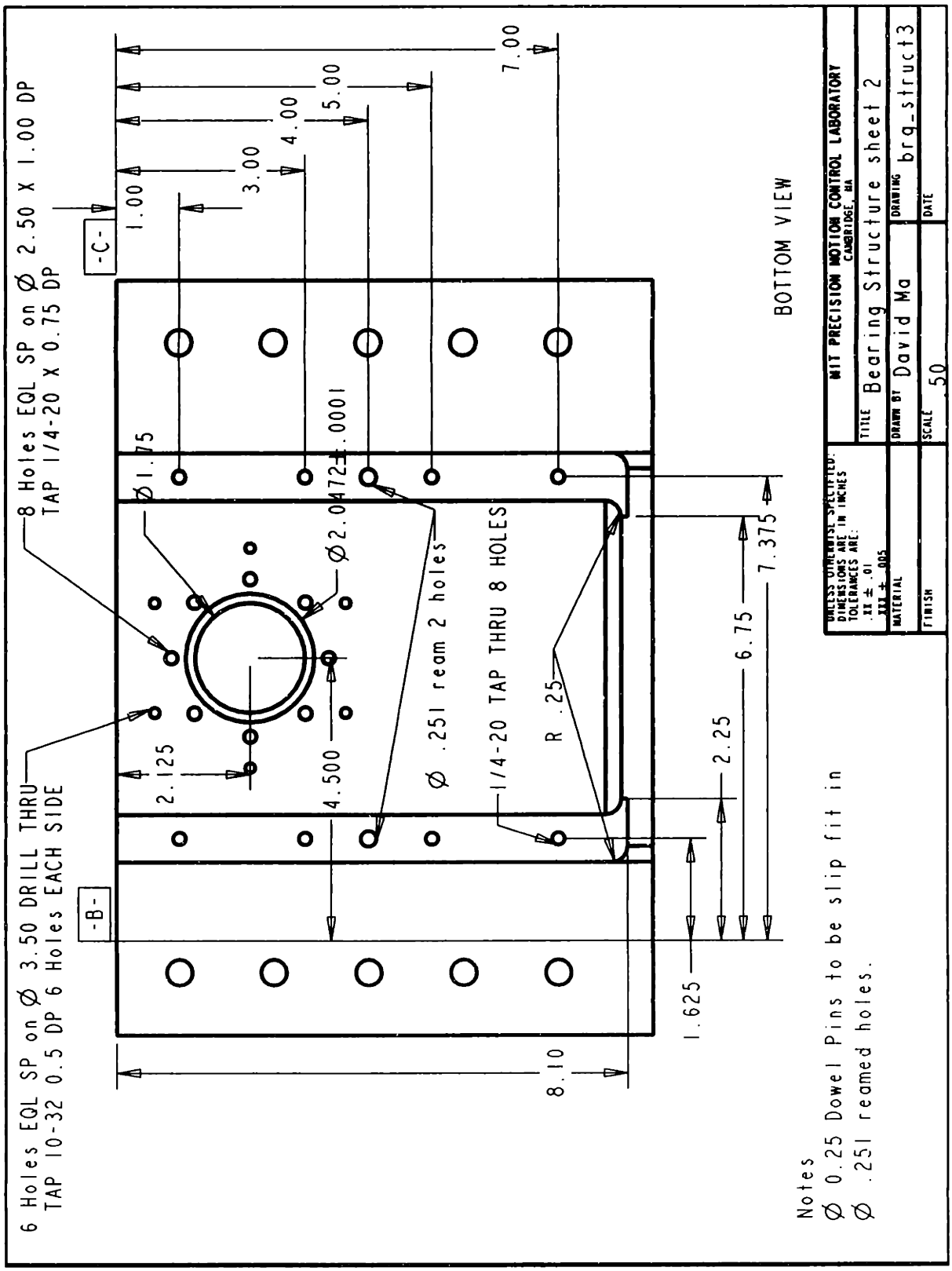

Figure 4-2: Bottom view of the bearing structure.

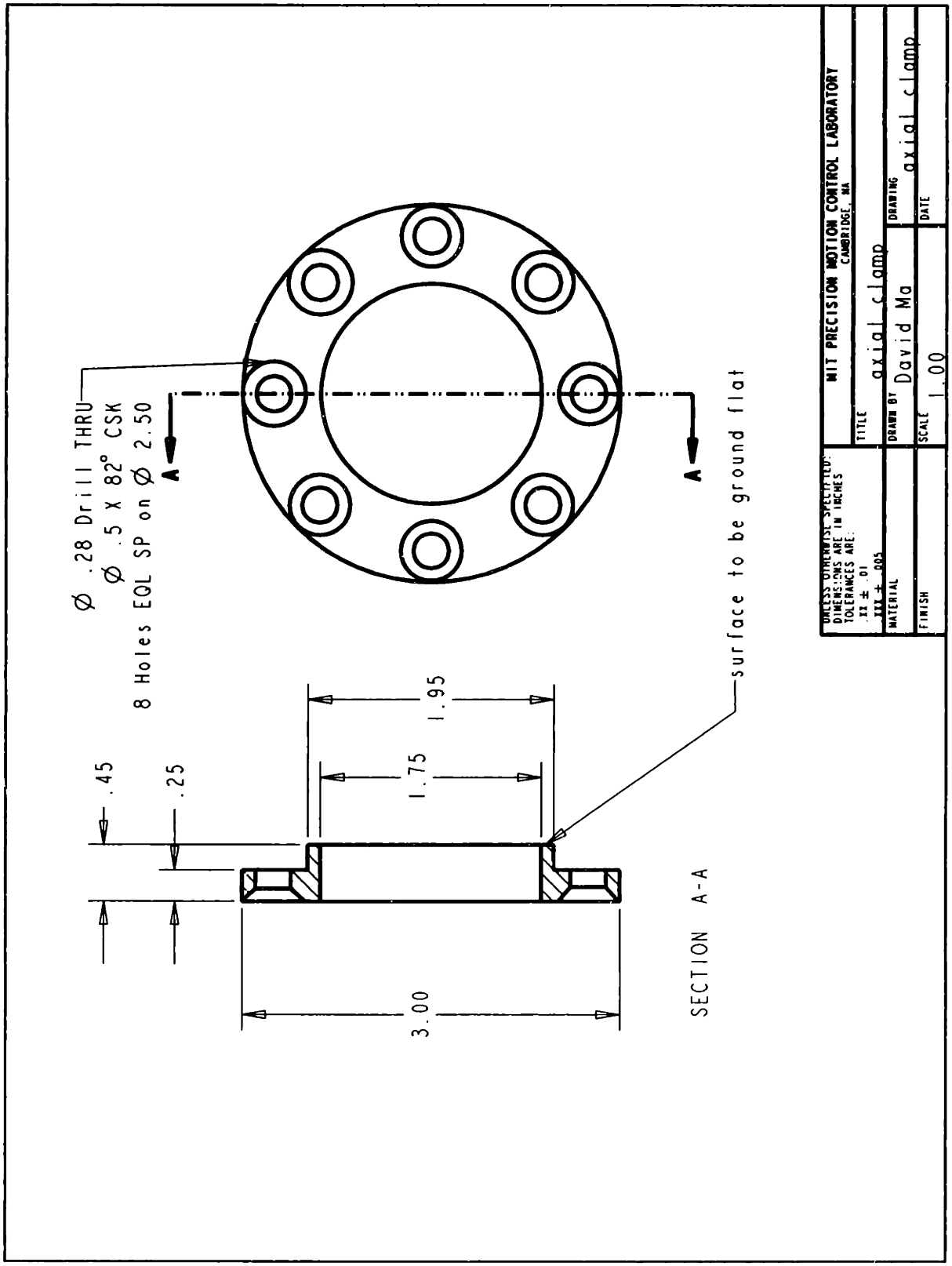

Figure 4-3: Drawing of the axial clamp for the thrust bearings.

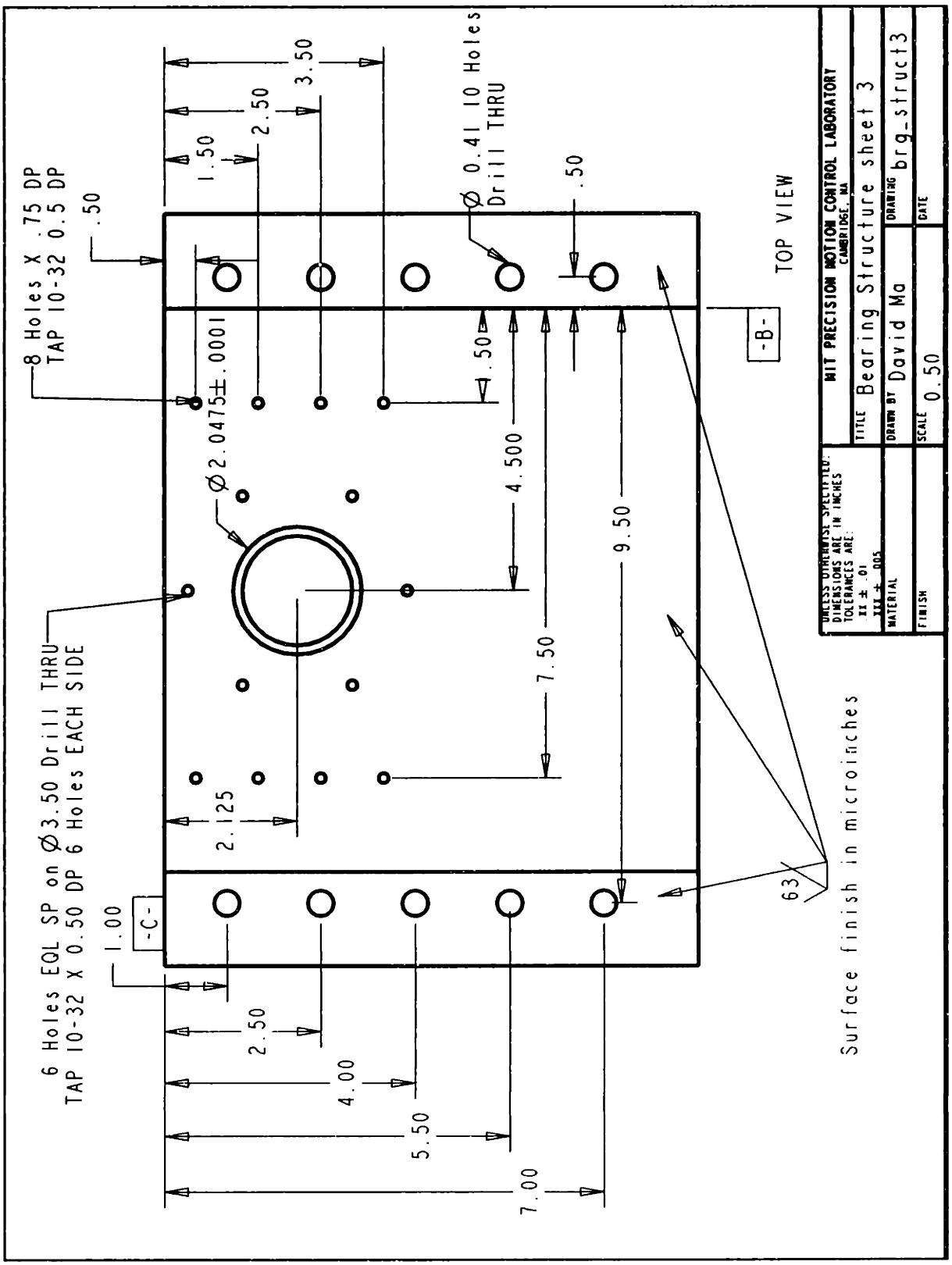

Figure 4-4: Top view of the bearing structure.

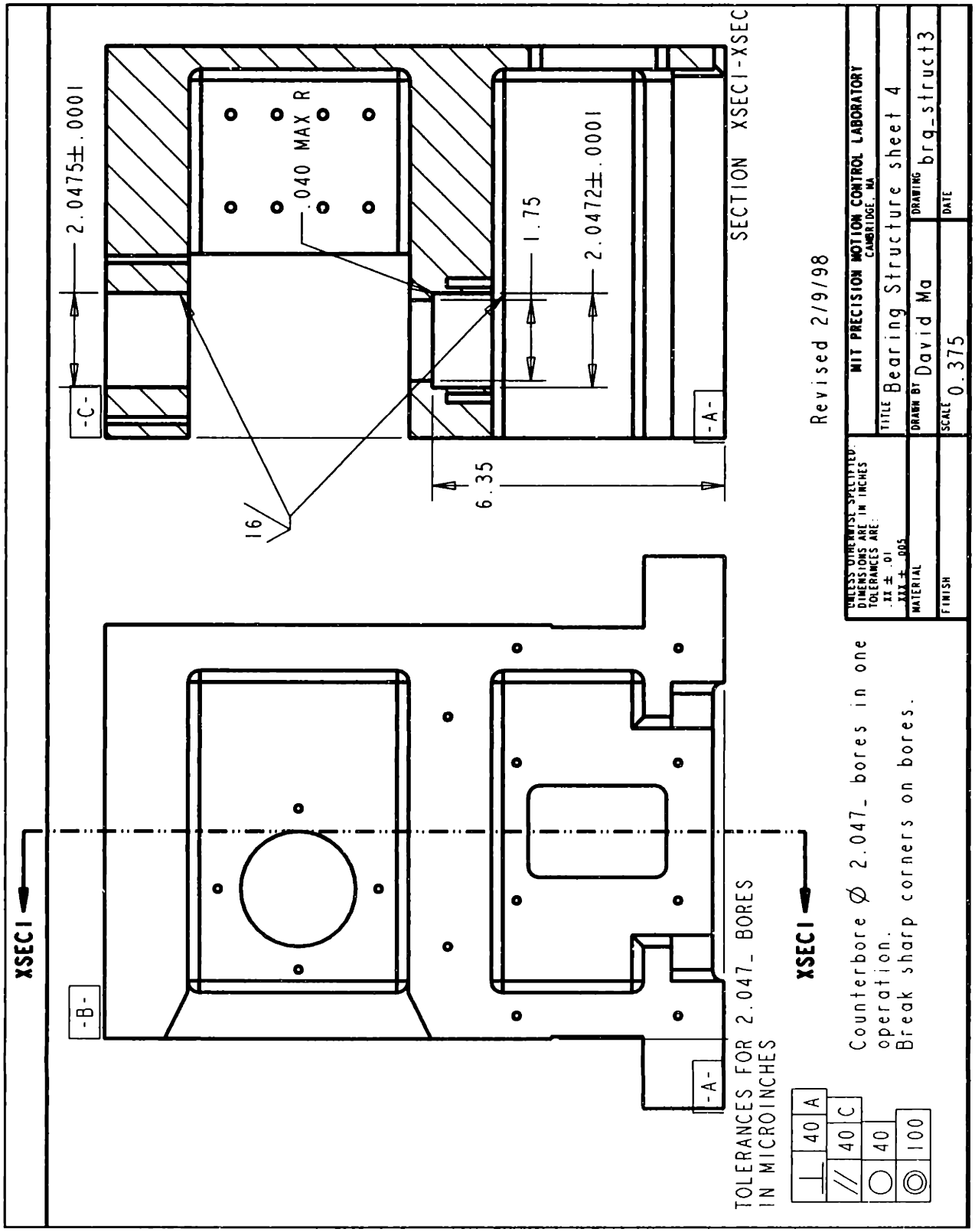

Figure 4-5: Cross-section of the bearing structure.

the bearing housings and their geometric tolerances. These tolerances can be found in a manufacturer's catalog, i.e. Barden. The shoulder inside the thrust bearing housing locates the entire bearing and tool arm shaft assembly with respect to the machine base. To aid in meeting the concentricity specification of 100 microinches, we counterbore the bearing housings in one operation. Therefore, the concentricity of the two bores is determined by the straightness of the jig borer's axes. For referencing and fixturing the structure during machining, we use the structure's datum planes. This is required in order to meet the squareness and parallelism tolerances of 40 microinches, because we specify the tolerances relative to the datum planes. The other tolerance specified is the roundness of the bearing bores, which is 40 microinches.

Figure 4-6 shows the front view of the structure. Six, 10-32 tapped holes on the front of the structure allow us to seal the bottom half of the bearing structure by bolting on a plate. Figure 4-7 shows the back view of the structure. The 2.5" diameter hole in the back plate allows us to insert a vacuum cleaner next to the tool arm to remove chips and dust during cutting. The rectangular hole near the bottom of the back plate gives us access to components inside of the structure, such as the flexible coupling, after the structure has been bolted onto the machine base. Both of these holes can be sealed by plates bolting into the 10-32 tapped holes. Figure 4-7 shows a side view of the structure. Two 1/2-13 screws protruding from each side of the bearing structure provide a means to easily move the structure. These screws are removed when the structure is fixtured to the base. The eight, 1/4-20 tapped holes on the side of the bearing structure are general-purpose holes. One possibility is to attach a LVDT sensor to the side of the structure as a probe for the lenses that we cut. The sensor can used to calibrate the position of the lens blank with respect to the RFTS, and to measure the lens after the cutting process. Eventually, the RFTS could also be programmed to perform these tasks. Then, it may be useful to have the LVDT as an independent verification of the measurements taken by the RFTS.

Figure 4-9 shows a drawing of the tool arm shaft. The important features are the bearing seats which have a diameter of 0.9843 ± 0.0001". As mentioned in the previous chapter, both bearing seats are intended to have a slight interference fit with the

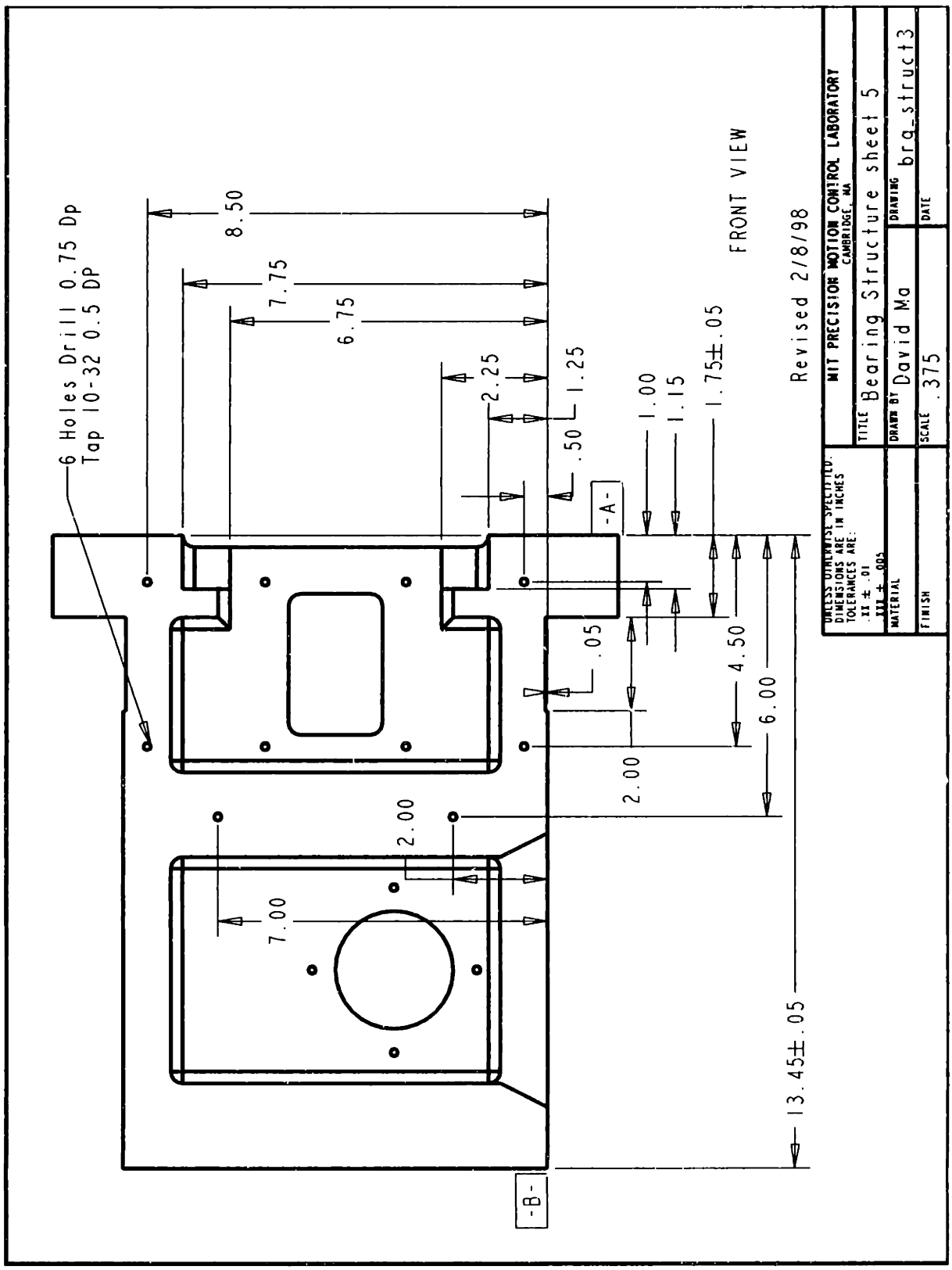

Figure 4-6: Front view of the bearing structure.

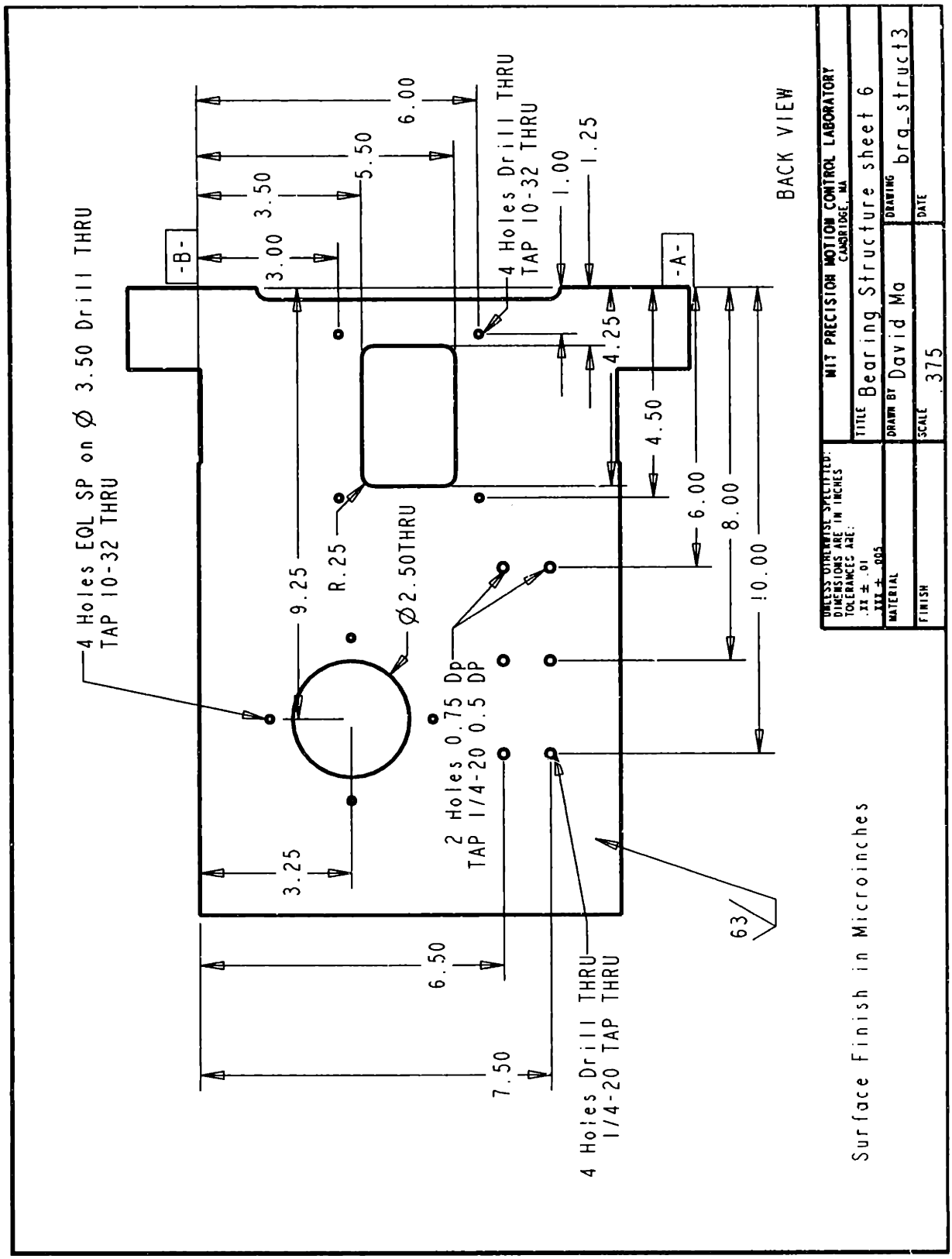

Figure 4-7: Back view of the bearing structure.

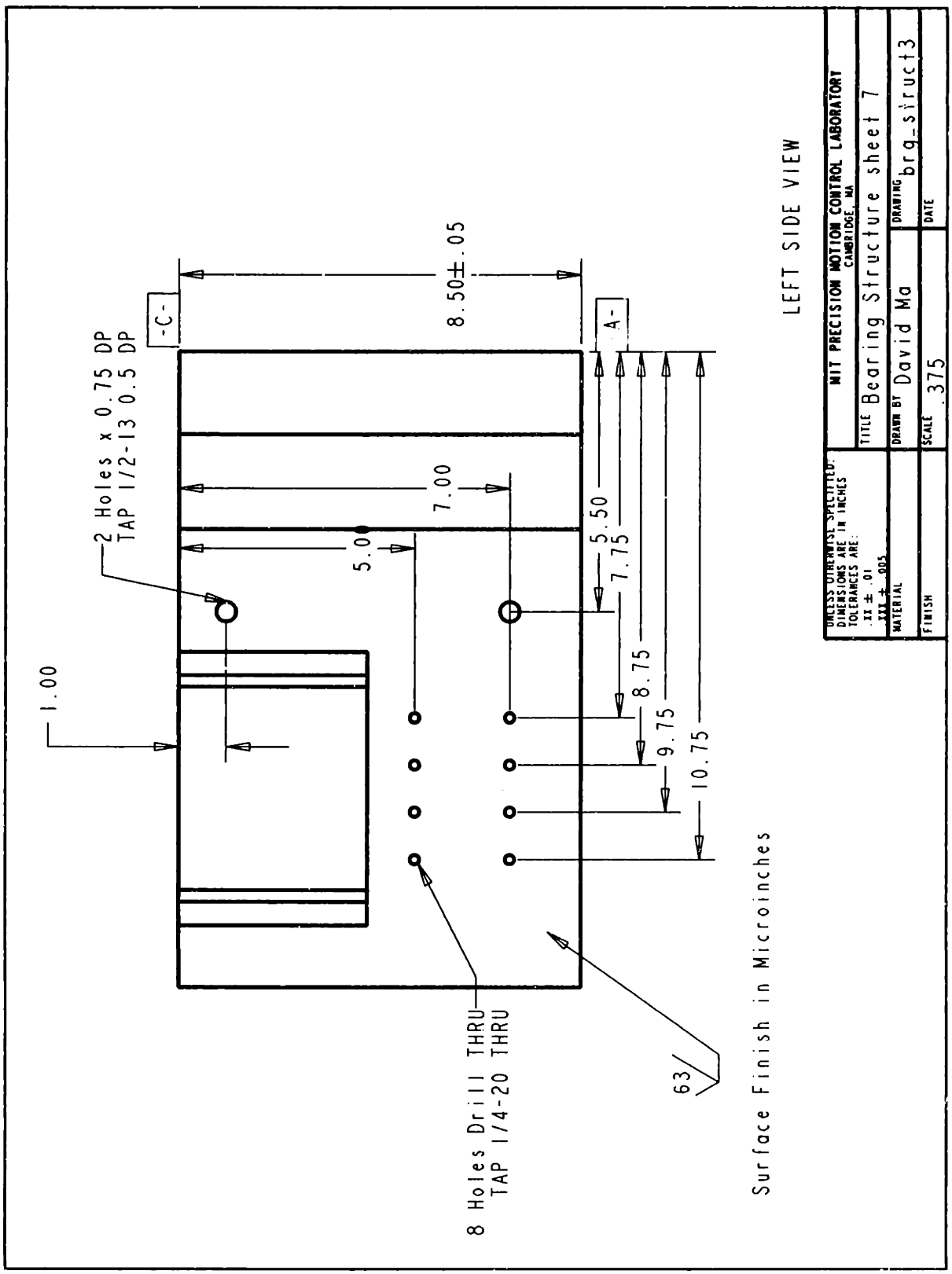

Figure 4-8: Side view of the bearing structure.

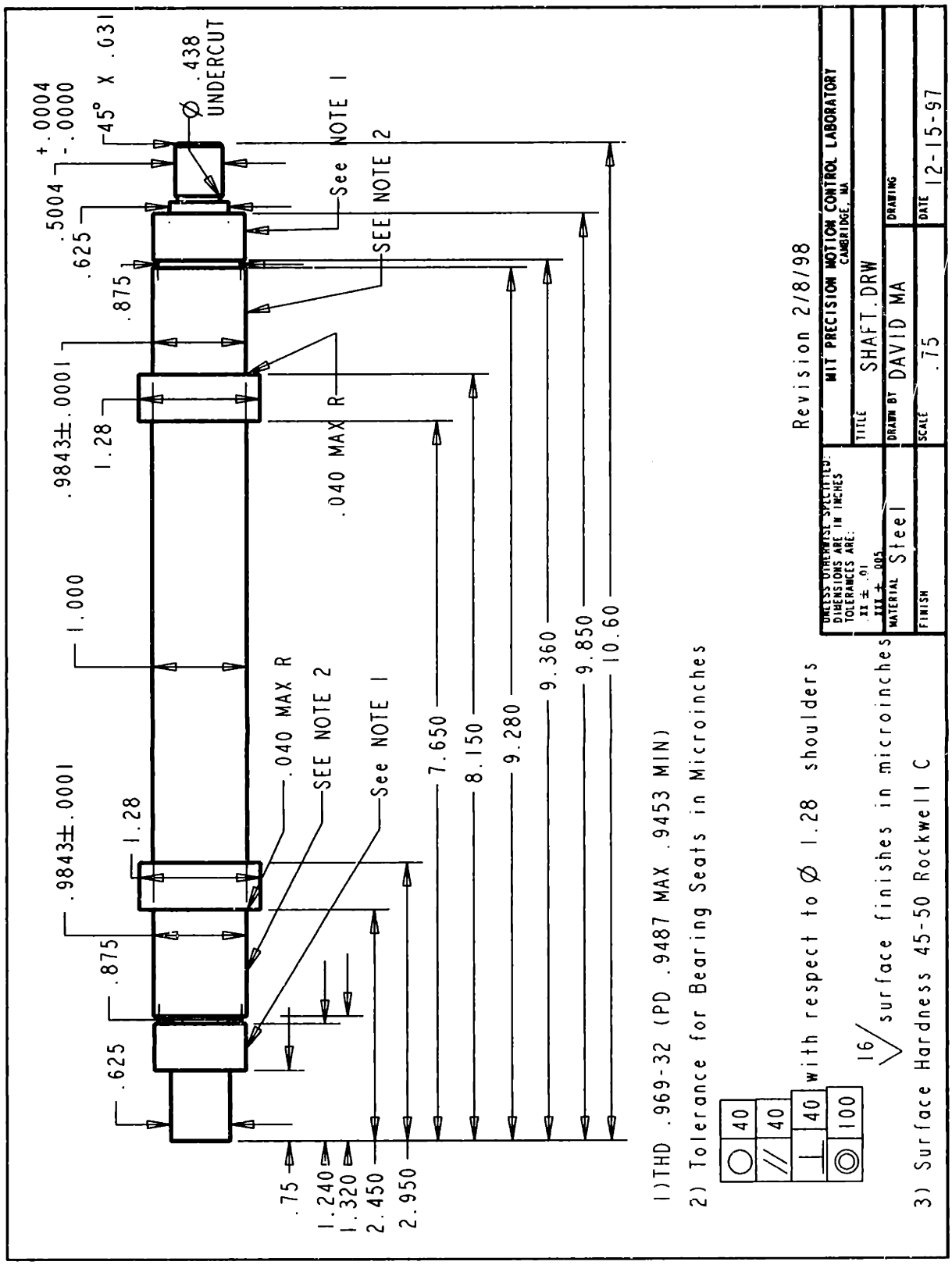

Figure 4-9: Drawing of the tool arm shaft.

bearings. Since we do not desire relative motion between the shaft and the bearings, they have the same specified fits as the outer races of the thrust bearings. As the bearings are mounted, they are press-fitted against the 1.28" diameter shoulders on the shaft. Thus, the squareness of the shoulders is an important geometric tolerance, which we specify to be square to within 40 microinches. The tolerance on the tool arm shaft's shoulders is equivalent to the tolerance on the shoulder in the thrust bearing bore. In terms of concentricity, roundness, and parallelism, the bearing seats have the same tolerances as the bearing bores. Next to the bearing bores, the tool arm shaft is threaded for a locknut. The locknut clamps the inner races of the bearings against the shoulder on the shaft. This clamping action by the locknut preloads the bearings. There is a slight undercut between the bearing seat and the threaded section of the shaft. This allows the face of the bearing to slightly protrude past the bearing seat, and to allow the locknut to be tightened against the bearing. The shaft end with a 0.625" diameter inserts into the flexible coupling, connecting the tool arm shaft to the servomotor. On the other end, features are added to fit the MicroE encoder onto the shaft. The entire shaft is heat-treated to surface harden the shaft to a Rockwell C hardness of 45-50.

Figure 4-10 shows a drawing of the motor face-plate, to which the motor is bolted. A flange on the motor's face inserts into the 2.187 +0.001" diameter hole. The motor bolts into the face-plate via the four, 1/4-20 tapped holes on a 3.50" square around the hole for the motor flange. Two, 0.25" diameter dowel pins are press-fitted into the 0.249" diameter reamed holes. As mentioned before, the dowel pins give the face-plate locational accuracy when it is bolted onto the bearing structure.

4.2 Bearing Structure Fabrication

With the design of the bearing structure finalized, the next issue is how to fabricate it. For this we consider three options: a bolted structure, a weldment, and a casting. Figures 4-11 and 4-12 show the form of the bearing structure before machining. It is clear that the structure could be fabricated by bolting individual plates together,

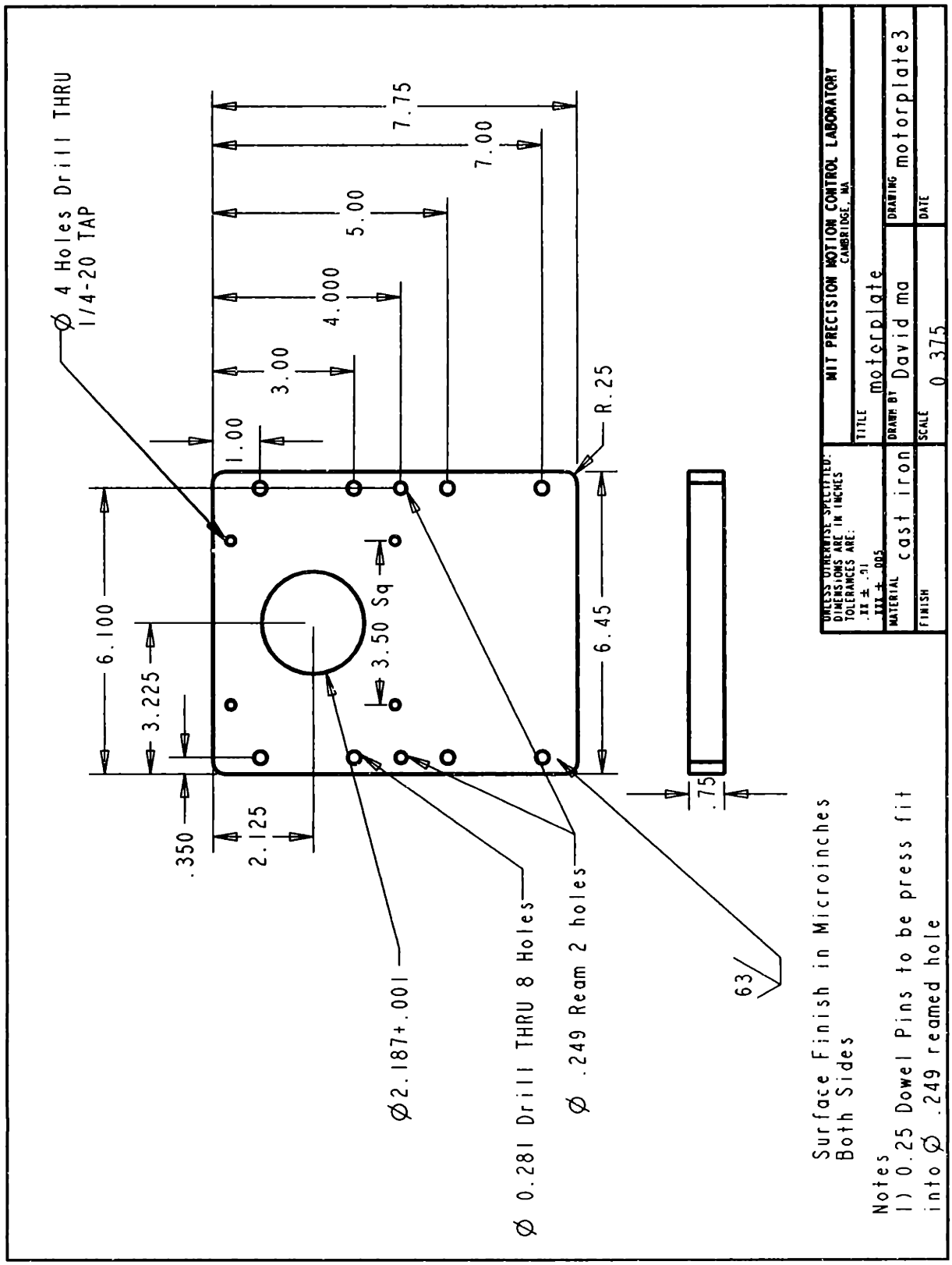

Figure 4-10: Drawing of the motor face-plate.

welding the plates, or by casting the entire structure as one piece. The first-generation bearing structure, used for the testbed, is bolted together. While it works well for testing the bearings, there are some concerns with bolting together the second-generation bearing structure. First, while unlikely, if the structure is ever unbolted, the concentricity of the bores is lost. Also, it is possible that over time the pieces of the structure can creep and shift with respect to one another. Finally, in order to insure that the joints are well-constructed, all the matings surfaces of the pieces would have to be ground flat and to the same dimensions before being assembled. This requires many secondary machining operations. The second option, a weldment, is a better candidate. After being welded together, the structure can be considered monolithic, and its components are less likely to creep over time. The individual pieces still have to be machined, but with less precision because the welding insures the joining of the individual pieces. However, in an evolutionary sense, a weldment is the step between a bolted structure and a casting which is by definition, monolithic. The question becomes whether a casting is economically feasible.

As a baseline, the MIT Central Machine Shop quoted the materials and labor for a weldment to be $1000. For casting the structure, a couple of options are lost foam casting and sand casting. In lost foam casting, a pattern of the structure is machined from polystyrene. Then, sand is packed around the pattern, and molten metal is poured in, vaporizing the polystyrene and leaving the metal casting. For sand casting a permanent model is made. For our purposes, a wood pattern is sufficient because we do not expect to cast many pieces. In the case of sand casting, the pattern is removed before the metal is poured into the sand mold. According to information from various foundries, lost foam casting apparently produces castings with slightly better dimensional accuracy and better surface finish. We were quoted 1/16" accuracy over one foot for lost foam casting, versus 1/8" accuracy over one foot for sand casting. However, one disadvantage with lost foam casting is that the pattern is lost during the casting. With conventional sand casting, many castings can be made from one wood model.

In the end, casting the structure is a surprisingly economical method of fabrication.

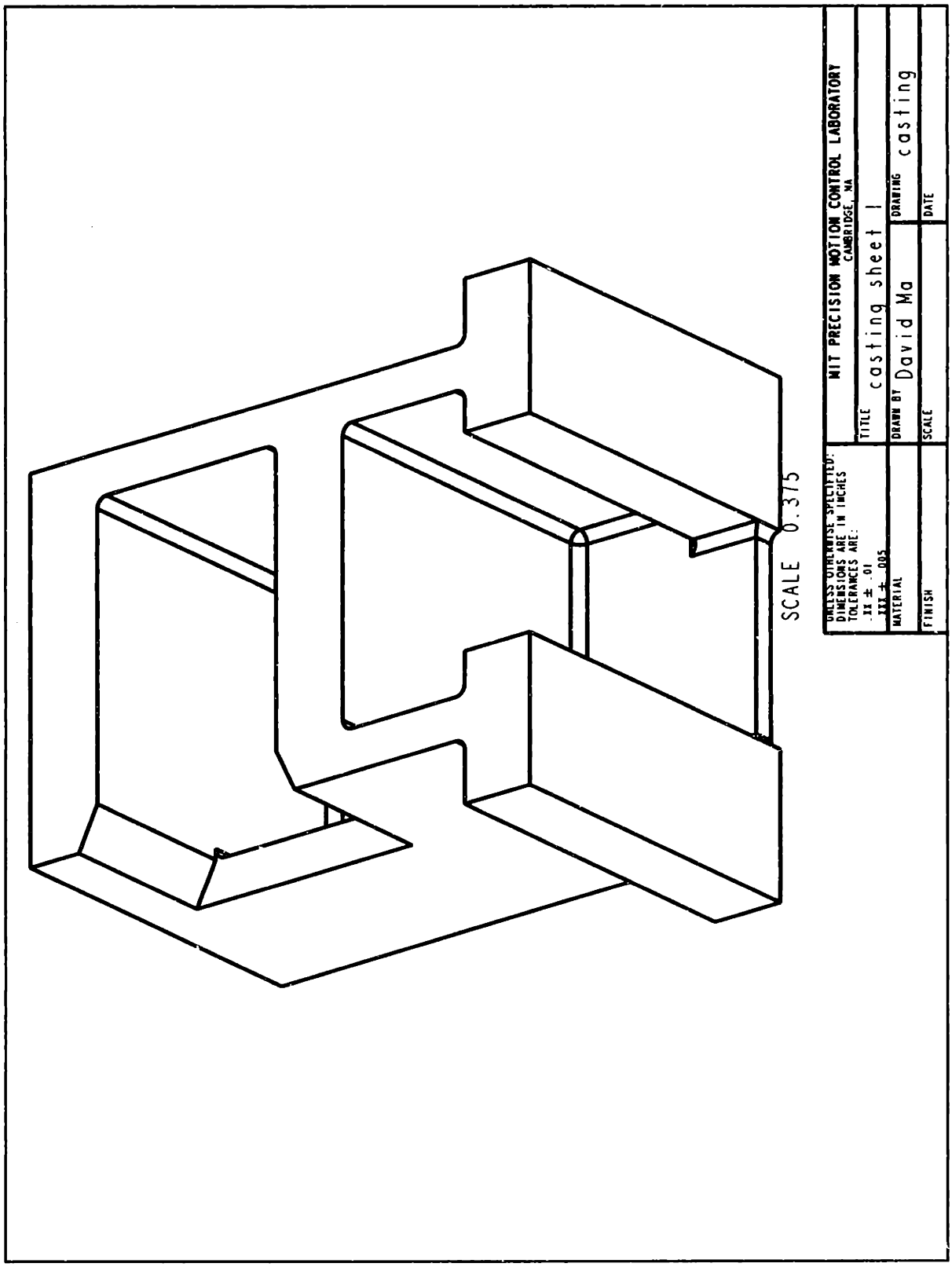

Figure 4-11: Form of the bearing structure before machining.

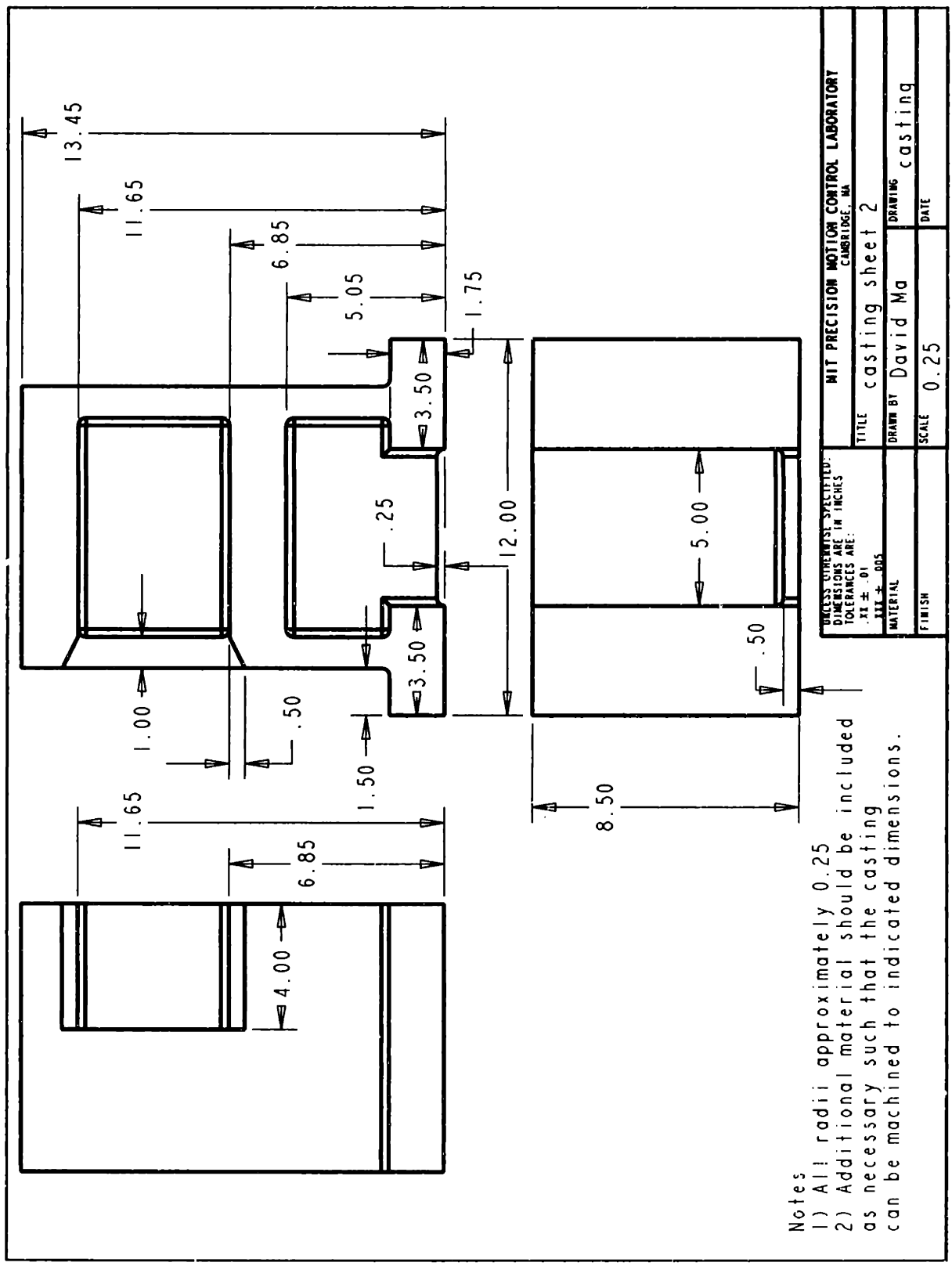

Figure 4-12: Dimensions of casting.

Quotes from two different foundries for lost foam casting were $306 and $600. For sand casting, the lowest quote was $460 for the pattern and $155 for each casting from Charlotte Brothers Foundry [1]. Compared to paying $1000 for the weldment, casting is a better design option and less expensive. Because of a shorter lead time and the ability to make additional castings quickly and cheaply, we decided to sandcast the bearing structure.

In Figure 4-12, we can see that all the inside corners of the structure have 0.25" radii fillets. While unnecessary for welded and bolted structures, they are required in castings to avoid sharp corners, which can become points of stress concentration. Also, additional material was specified on the outer dimensions of the casting so that we could machine the entire structure down to the indicated dimensions. The material for the casting is gray cast iron Class 30. Gray cast iron is typically used for machine tools because it has high natural damping. The Class 30 refers to the minimum tensile strength of the metal, in this case 30,000 psi/in^2. After casting, the structure then heat-treated to be stress-relieved.

Brookfield Machine undertook the machining of the casting. Their quote was $4305 for machining the bearing housing, the motorplate, the shaft, and installation of the bearings [2]. Finding a machine shop willing to machine the casting was difficult. Quotes ranged from Brookfield's quote of $4305 with a six week delivery time, to $8000 and a fourteen week delivery time from another shop. Some shops were simply unwilling to quote the job. In terms of the design of the bearing structure, the only difficult feature to machine is the counterboring of the bearing bores, which have a dimensional tolerance of ± 0.0001". Many of the shops we approached were unwilling to commit to hitting that tolerance. Another difficulty is that they must be done in one operation to insure the bores are as concentric as possible. The analogous dimensional tolerance on the shaft is much easier to hit via cylindrical grinding. We may be able to assume that once fixtures designed for the production machine are developed, machining the bearing bores will become more efficient.

[1] Charlette Foundry, 74 Mill River St., Blackstone MA, (508) 883-8850.
[2] Brookfield Machine, 62 Central St., West Brookfield MA 01585, (508) 867-3200

Another idea, suggested by Prof. Slocum, which may be considered in the future as an option for production, is to replicate the bearing bores [3]. In replication, the bearings and the shaft are cast into place with a no-shrink polymer. In order to do this, the grinding of the shaft and the installation of the bearings onto the shaft remains the same. However, instead of counterboring the bores to the dimensions of the bearings' outer races, the bores are machined slightly larger, by approximately 0.050". Then, the rotational axis of the shaft and the bearings is aligned square with Datum A. The axis also has to be aligned concentric with the axis of the oversize bores. Finally, the polymer is injected around the bearings and allowed to set. The advantage of this process is that the polymer takes the shape of the bearings and the bores around them. Therefore, not as much accuracy is needed when machining the bores around the bearings. Devitt Machinery, the company which built our air bearing linear slide, has significant experience in this. They replicate their bearing pads for their air bearings with a metal-filled epoxy, such as DWH 310FL [4]. It is also not difficult to test this process on a scaled down model, which would include a well-ground shaft, some inexpensive bearings, and a bearing housing with the oversized bearing bores machined into it.

4.3 Cost Breakdown for the RFTS Axis

Since the prototype may at some point may become a production machine, it is important to look at the cost so far in building the RFTS Axis. Clearly, the highest cost has been machining the bearing structure. However, in production this cost should decreasing significantly. Developing specialized fixtures might also increase the efficiency of the operation. Still, considering the accuracy and care required to machine the bores, replicating the bearings remains an attractive option.

[3]Professor Alexander Slocum is a Professor at MIT.

[4]Devitt Machinery Co., 4009-G Market St., Aston PA 19014, (610) 494-2900

Component	Cost ($)
Servo Motor	960
Power Amplifier	800
Motor Cables	400
Flexible Coupling	652
Bearings	428
Casting	615
Machining	4305
Encoder	3000
Tool	170
Total	11330

Chapter 5

Measuring Lens Form Error

A quantitative assessment of the form error in ophthalmic lenses currently produced is important for estimating the necessary cutting accuracy required of the prototype turning machine. Five cut and polished, -8 diopter lenses, spherical lenses with no cylinder power, have been measured with a Coordinate Measuring Machine (CMM) to determine the magnitude of the form error in the lenses after the lapping process. In addition, one cut but unlapped -8 diopter lens has also been measured to determine the magnitude of the form errors after the turning process. For each lens, the measured points on each lens can be fit with two different algorithms, a best-fit algorithm and a known-radius algorithm. For the best-fit algorithm, a Least Squares Fit is done allowing the radius of curvature of the predicted sphere to vary. For the known-radius algorithm, the measured points are fit to a sphere with a set radius predetermined by the desired optical power of the lens. A detailed survey of using Coordinate Measuring Machines for metrology is given in [10]. Some additional sources that cover using CMM's in coordinate metrology are [13] [3].

After the Least Squares Fit, the best-fit radii of curvature of the five lenses have a corresponding optical power range of $\pm$ 0.07 diopters. Fitting the data points to a sphere with a set radius is also useful, because it allows us to see the actual errors which occur in the lapping process. A similar analysis of the unpolished lens allows us to see the form errors due to machining inaccuracies.

5.1 Lens Measurement Procedure

5.1.1 Description of the coordinate measuring machine.

The CMM, from Brown and Sharpe, is basically a ruby-tipped probe positioned by 3 motorized axes traveling on air bearings [1]. When the probe tip is deflected upon touching the surface of the lens, the x, y, and z coordinates are registered by the computer. By taking a series of points, we can obtain a measurement of the lens shape. In our tests, we take a 4 cm x 4 cm grid of points spaced 4 mm apart, for a total of 121 points. The grid of the sample points is approximately centered on the vertex of the lens.

5.1.2 Lens fitting algorithm.

All of the lenses we measured have a power of eight diopters. For a spherical lens, the geometry of the lens is given by

$$R^2 = (x - x_o)^2 + (y - y_o)^2 + (z - z_o)^2, \tag{5.1}$$

where R is the radius of curvature, x, y, and z are the coordinates of a point on the surface of the sphere, and x_o, y_o, and z_o are the coordinates of the center of the sphere.

As we described in Chapter 2, the power of a ophthalmic lens is a function of the thickness of the lens, the Index of Refraction of the lens material, and the radius of curvature R. Therefore, there is not an exact relation between the radius of curvature of a lens and its optical power. The opthalmic industry has adopted a standard called tool power P. This standard allows us to assume a certain Index of Refraction and thickness of the lens, and then cut a radius of curvature R knowing only the power

[1] Brown & Sharpe Mfg. Co., Precision Park, 200 Frenchtown Rd., North Kingstown, RI 02852, (800) 648-4640

of the lens which is desired. This relation is given by

$$R = 530/P, \tag{5.2}$$

where R is in millimeters.

We have written a routine using Matlab to perform the Least Squares Fits of the lenses. For the best-fit algorithm, we use a starting vector $[R_{fit}\ x_o\ y_o\ z_o]$ which represents the "guesses" of the true radius of curvature and center of the sphere. Using eq. 5.1, a test radius R_{test} is generated for each CMM data point assuming the coordinates of the center of the sphere to be x_o, y_o, and z_o. Therefore, the error ϵ is $(R_{fit} - R_{test})$, and the squared error ϵ^2 is $(R_{fit} - R_{test})^2$. Matlab then performs a simplex search to minimize ϵ^2 by varying R_{fit}, x_o, y_o, z_o. For the known-radius algorithm, the procedure is the same as for the best-fit sphere algorithm, except that R_{fit} is a constant given by eq. 5.2.

5.1.3 CMM accuracy and repeatability

The CMM has a total measuring volume of 457 x 508 x 406 mm, with a stated repeatability of 3 μm, a volumetric accuracy of 10 μm, a linear accuracy of 5 μm, and a resolution of 1 μm. Some of the possible sources of inaccuracies in our measuring process include mechanical tolerances of the CMM, probe tip deflection inaccuracy, thermal effects from a uncontrolled temperature environment, and the data fitting algorithm. We can test the accuracy and noise level of the CMM by performing the Least Squares Fitting algorithm described above on a "perfect" gage ball with a known diameter of 19.0490 mm (0.75"). The gage ball is used to calibrate the CMM probe tip diameter and is perfect in the sense that variations in its form and surface finish are good enough to be undetectable by the CMM. Thus, any error in calculating the radius of curvature of the gage ball is assumed to be due to limitations of the fitting algorithm and the inaccuracies of the CMM. The variance of the residual errors from the Least Square Fit of the gage ball should be the variance of the errors in the measurement process σ_N^2. If we assume that the errors in the system are random,

the variance of the residual errors from the Least Squares Fit of the lens σ_R^2 is a linear combination of actual form error variance σ_A^2 and σ_N^2 [5]. After measuring the variance of the error in the system σ_N^2, by measuring the gage ball, the actual variance of the form error σ_A^2 is

$$\sigma_A^2 = \sigma_R^2 - \sigma_N^2. \tag{5.3}$$

This gives us a sense of whether or not the CMM's resolution and accuracy limits it from measuring the form error in our lenses. If σ_N^2 is the same magnitude as σ_R^2, then we cannot be certain if the error we are measuring is due to form error of the lens or inaccuracies in our measuring process.

We can also test the repeatability of the measuring process by taking a grid of sample points on a lens three times over the same sample space, and then comparing the results from the three Least Squares Fits with each other.

5.2 Results

To measure the accuracy of our procedure, we took 195 sample points of the gage ball with a known radius of curvature of 9.5245 mm. Ideally the probe tip diameter would be known before measuring the gage ball. However, the only method of establishing the probe tip diameter currently is to calibrate it with the same gage ball. The best-fit algorithm found the radius of curvature to be 9.5224 mm, a difference of 2.1 μm. The standard deviation σ_N was 1.1 μm. Now that we have a measurement of the inaccuracies in the system, we can find σ_A of the lenses with eq. 5.3.

The table below lists the Least Squares Fit radii and the corresponding powers for the six lenses after fitting the CMM data using the best-fit sphere algorithm. Also listed are the standard deviations σ_R and σ_A. Lens 6 is the unpolished -8 diopter lens. We can see that when trying to produce an -8 diopter lens with $R = 66.25$ mm, the powers of lenses actually produced range from -7.962 to -8.067 diopters. σ_A ranges from 2.6 μm to 3.8 μm. One interesting note is that lens 6, the unpolished lens, has a best-fit radius of curvature that is in the same range as the polished lenses. To see if this holds true for all unpolished lenses, more test lenses would have to be made.

Comparing σ_A and σ_R, we see that the difference between them is only 0.2μm. The inaccuracies in the system appear to be insignificant compared to the magnitude of the errors in the lenses. Therefore, we can be reasonably confident that the error we are measuring represents actual form error in the lenses.

Lens number	Radius of Curvature (mm)	Diopters	σ_R (μm)	σ_A (μm)
1	65.6928	8.067	4.0	3.8
2	66.5658	7.962	4.0	3.8
3	66.5031	7.969	3.2	3.0
4	66.4921	7.971	2.8	2.6
5	66.4912	7.971	3.9	3.7
6	65.9655	8.035	2.9	2.7

We also list below σ_R and σ_A from fitting the CMM data using the known-radius algorithm. From the table, we see that σ_A ranges from 6.8 μm to 9.4 μm. Again, after subtracting the inaccuracies in the measuring process, the standard deviation of the residual errors decreases only slightly, in this case by only 0.1 μm.

Lens number	σ_R (μm)	σ_A (μm)
1	8.3	8.2
2	9.5	9.4
3	7.2	7.3
4	6.9	6.8
5	7.3	7.2
6	8.0	7.9

To test the repeatability of our measurements, we measure a lens with a power of -6.25 diopters three times over the same sample-space and fit the data with the

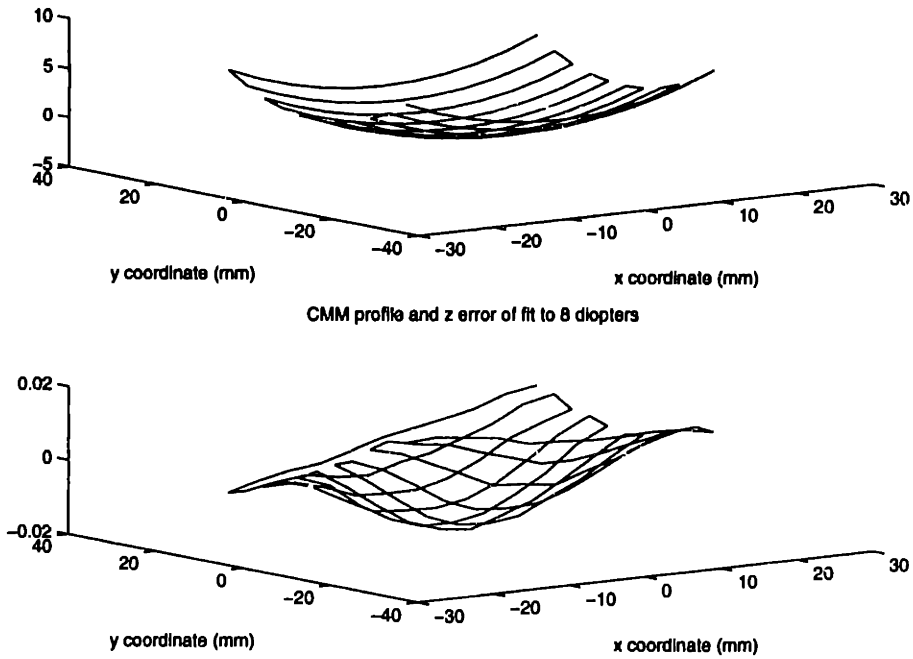

Figure 5-1: Lens surface and residual error plot for lens 1.

best-fit algorithm. Their σ_A's, shown below, and are within 0.4 μm of each other, which is small enough to be attributable to the inaccuracies in the system. Therefore, the measurements appear to be very repeatable.

Trial number	σ (μm)
1	1.8
2	2.1
3	2.2

5.2.1 Plots of the lens' surfaces and form errors.

Figure 5-1 shows a plot of the lens surface. Also shown is the error in the z direction for lens 1, after fitting the CMM data with the known-radius algorithm. To more clearly see the errors, we show a top view gray-scale of the error plot in Figure 5-2. A linear interpolation has been done to fill in the spaces between the sample points. Figure 5-3 shows the lens surface and the errors in the z direction for lens 6, the

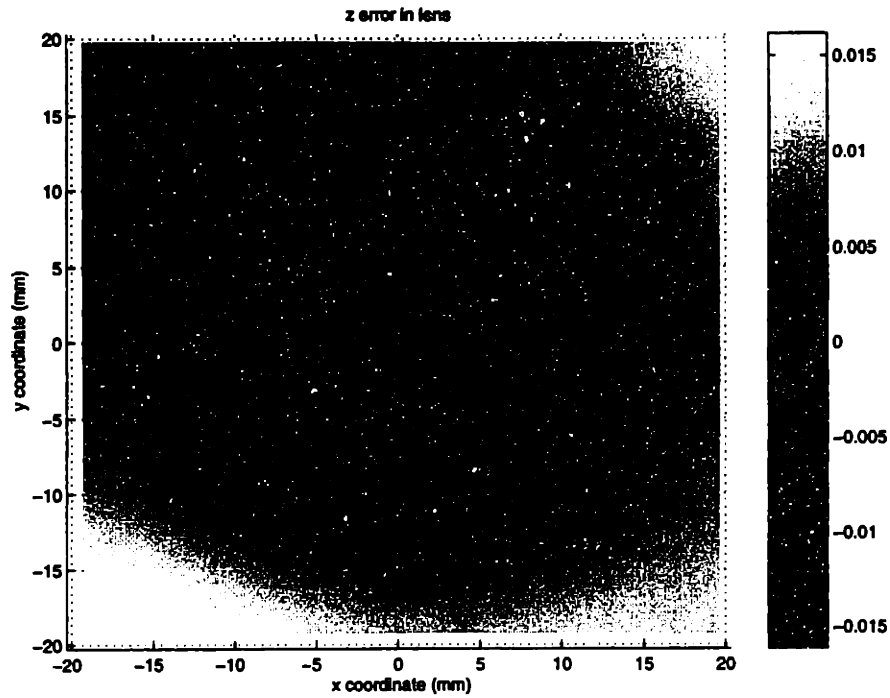

Figure 5-2: Top view of gray-scale error plot for lens 1. (cut and polished lens)

unpolished lens. Again, to more clearly see the errors, Figure 5-4 shows a top view gray-scale of the error plot. The plots are useful because they show the errors present after trying to make a lens with a radius of curvature $R = 66.25$ mm. The plots shown for lens 1, one of the polished lenses, are typical of the other four polished lenses. Lens 6 is the unpolished lens, and its error plot is clearly different from lens 1.

These plots show the type of form error in the lenses due to the lapping process in the case of lens 1, and the turning process, in the case of lens 6. We can see that for lens 1, the form error is very consistent. More material is being removed from the vertex of the lens, and the amount of material removed decreases away from the vertex. This may be due to the slurry in the lapping process being more concentrated at the vertex of the lens. Also, the errors seem to be fairly symmetric about the axis of rotation of the lens. During the lapping process, the relative motion between the lap and the lens is removing material equally around the lens's center. The magnitude of the error around the vertex of the lenses is on the order of $15 - 20$ μm. The distance from the center of the lenses to the edge of the error plots is approximately 20 mm.

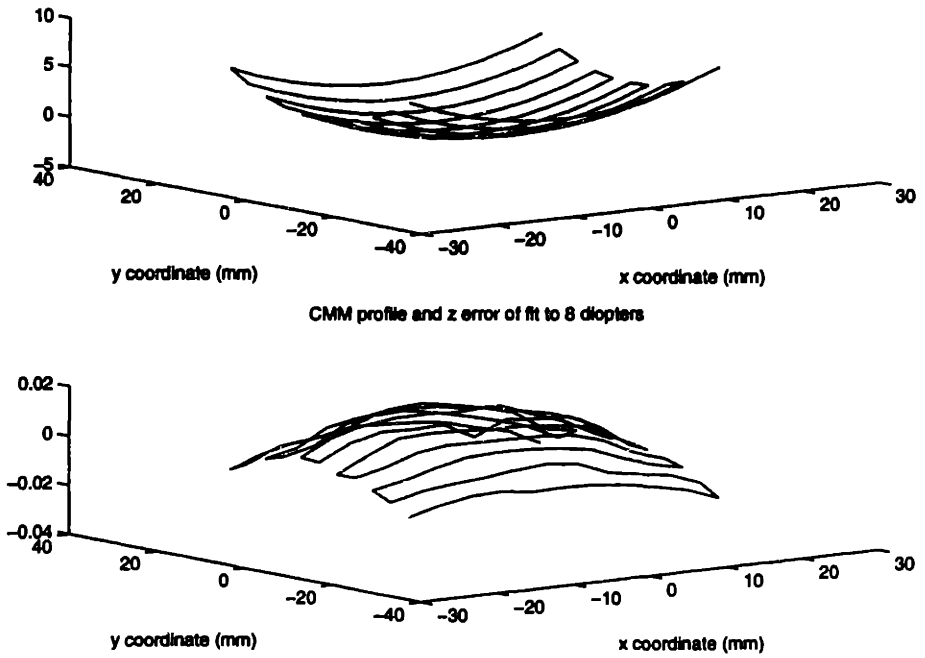

Figure 5-3: Lens surface and residual error plot for lens 6.

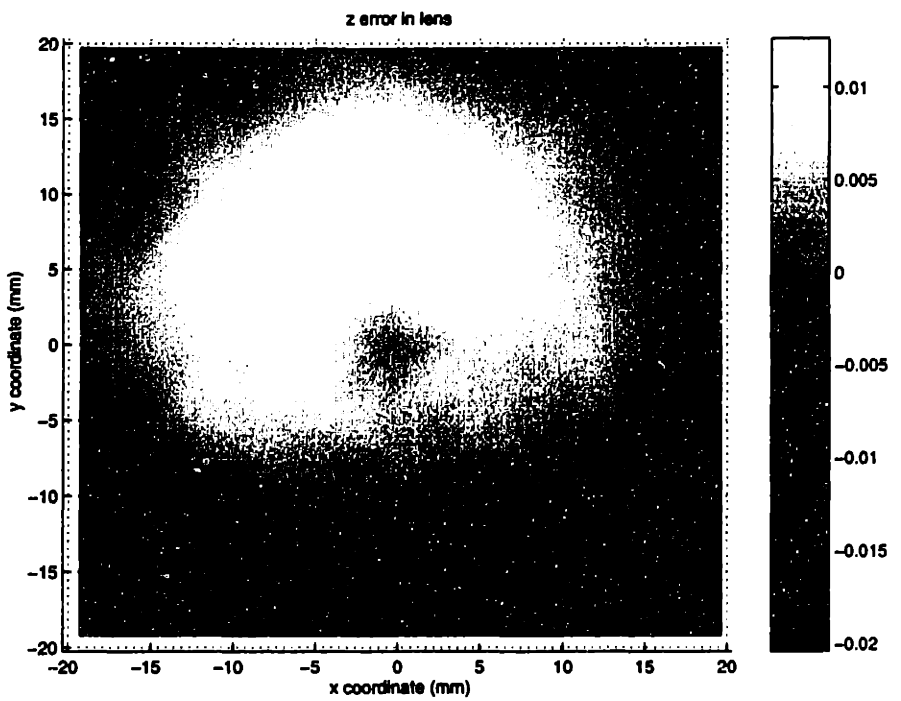

Figure 5-4: Top view of gray-scale error plot for lens 6. (cut lens without polishing

Over this distance, the magnitude of the error is typically 30 μm to 40 μm, for lenses 1-5. Therefore, the error gradient is approximately 1.5 to 2 μm/mm.

For lens 6, we can see that the form error is not as symmetric as the form error in the polished lenses. In fact, we can infer some information about the machining error from the error profile [14]. Referring to Steve Ludwick's work on error budgeting, a constant error in the position of the cross slide will lead to a rotationally symmetric error, and cross slide error at the spindle frequency will lead to asymmetric errors. The error profile shown in lens 6 appears to be a combination of the two. Higher frequency errors are more difficult to detect and would require taking more sample points at smaller intervals on the lens surface. At the very least, it appears we can detect errors which occur at the spindle frequency. It is also interesting to note that the magnitude of the errors in lens 6 are on the same order as the errors in lens 1. At certain points, the form error in lens 6 reaches 20 μm. This implies that the lapping process is not necessarily decreasing the magnitude of the form error, but is smoothing out the error and making the lens more uniform.

As noted in Chapter 1, the target accuracy of the prototype turning machine is 1 μm over 10 mm. Given that we are seeing an error gradients of at least 1.5 to 2 μm/mm over the finished lenses that we measured, this specification should be adequate for producing a lens that could be conformably lapped to the final shape and surface finish, eliminating the need for a hard lap.

Chapter 6

Control Implementation

In this chapter we describe some of the different control algorithms implemented on the RFTS testbed and the prototype machine. Some of the requirements of the RFTS that we address are,

- High servo bandwidth to cut nonrotationally symmetric lenses at high spindle speeds.
- High dynamic stiffness to reject disturbances such as cutting forces.
- Low tracking error during trajectory following to minimize cutting error.

The first requirement, a high servo bandwidth, comes from the need to cut toric lenses at high spindle speeds. To test the attainable bandwidth of the RFTS, PID control has been implemented with a bandwidth of 130 Hz. Currently, the bandwidth is limited by a torsional mode of resonance due to the compliances of the flexible coupling, the tool arm shaft, and the motor shaft between the motor armature and the tool arm. As discussed before, to cut a toric lens at a spindle speed of 3000 RPM, the fundamental frequency of the RFTS's trajectory is 100 Hz. Therefore, the servo bandwidth needs to be at least twice the spindle frequency in order for it to follow cutting trajectories. Since the cutting trajectory also contains higher harmonics of the fundamental frequency, we actually want a higher bandwidth to be conservative. Furthermore, we have shown in Chapter 3 that the RFTS's acceleration capability

is able to handle much higher frequency trajectories. Therefore, if we can set the RFTS's bandwidth high enough, cutting with spindle speeds of 4000 to 5000 RPM should be attainable.

During cutting, the RFTS encounters disturbance forces occurring at harmonics of the spindle frequency. These disturbance forces affect the attainable cutting accuracy and surface finish of the RFTS. In order to meet the second requirement stated above, high dynamic stiffness, we are experimenting with loop-shaping techniques to increase the dynamic stiffness of the servo loop. In our test case, the RFTS was approximately 50 times stiffer at a certain frequency with loop-shaping than without loop-shaping.

Feedforward control has also been implemented to reduce phase lag of the servo loop while following high frequency trajectories. Phase lag results in following error of the tool as it tracks a commanded trajectory. Initial results show that feedforward control has decreased following error of the RFTS by a factor of 4, at a spindle speed of approximately 1000 RPM. Initial tests for closing the PID loop and loop shaping have been done on the RFTS testbed, and feedforward control has been implemented on the prototype machine. As discussed in Chapter 2, the control algorithms are implemented by a DSP board from DSP Research, and the host computer is a Gateway 2000, 50 MHz 486 computer.

6.1 System Modeling

We are able to model the testbed system with reasonable accuracy if we assume the system is a lumped inertia, consisting of the inertias of the motor armature, the toolholder arm and shaft, and the two flexible couplings. The system gains are given below.

$J = 1.50 \times 10^{-3}$	Rotational inertia of the system (kg-m^2).
$K_S = 5.06$	Gain of the potentiometer (Volts/rad).
$K_A = 3$	Gain of the power amplifier (Amp/Volt).
$K_M = 0.74$	Motor constant (Nm/Amp$_{RMS}$).
$G_c(s)$	Controller Transfer Function.

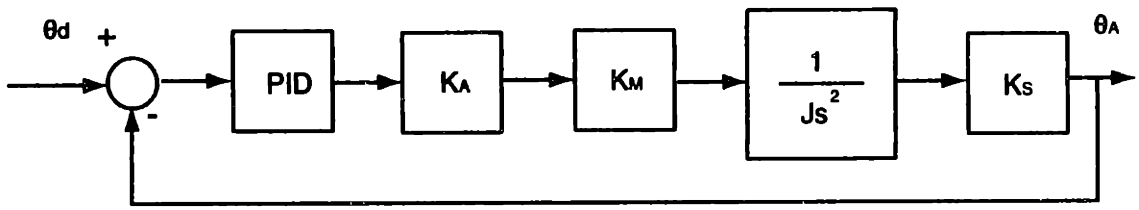

Figure 6-1: Block diagram of servo loop.

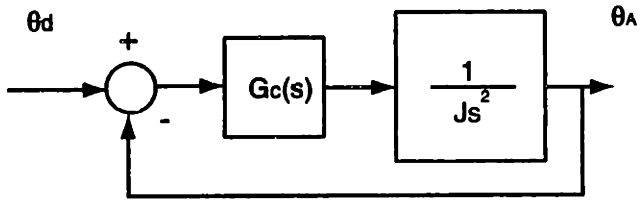

Figure 6-2: Simplified block diagram of servo loop.

The power amplifier is in torque mode rather than velocity mode, as it was in Chapter 3. Now, a voltage command to the amplifier results in a known current command and hence a known torque command. This is a cleaner utilization of the amplifier. It eliminates the velocity loop, which is closed by deriving velocity from the encoder feedback on the motor. It also makes modeling the system simpler, because now we can assume we are controlling an inertia, or double integrator. Figure 6-1 shows the block diagram of our model, which can be simplified as shown in Figure 6-2, where $G_c(s) = PID(s)K_AK_MK_S$. Now our plant is

$$\frac{1}{Js^2} = \frac{667}{s^2}, \tag{6.1}$$

and we can design a controller based on this model. At various points in time we will be breaking the position loop to inject disturbances and to implement feedforward control. Therefore, it helps to separate the inertia term from the other terms to help us keep track of the gains in the system. Figure 6-3 shows a schematic of the testbed layout for implementing the control algorithms.

To verify our model of the plant, we first measure the open-loop frequency response of the system. Figure 6-4 shows the open-loop frequency response, without feedback and the PID controller. For comparison, the predicted response of the system is also

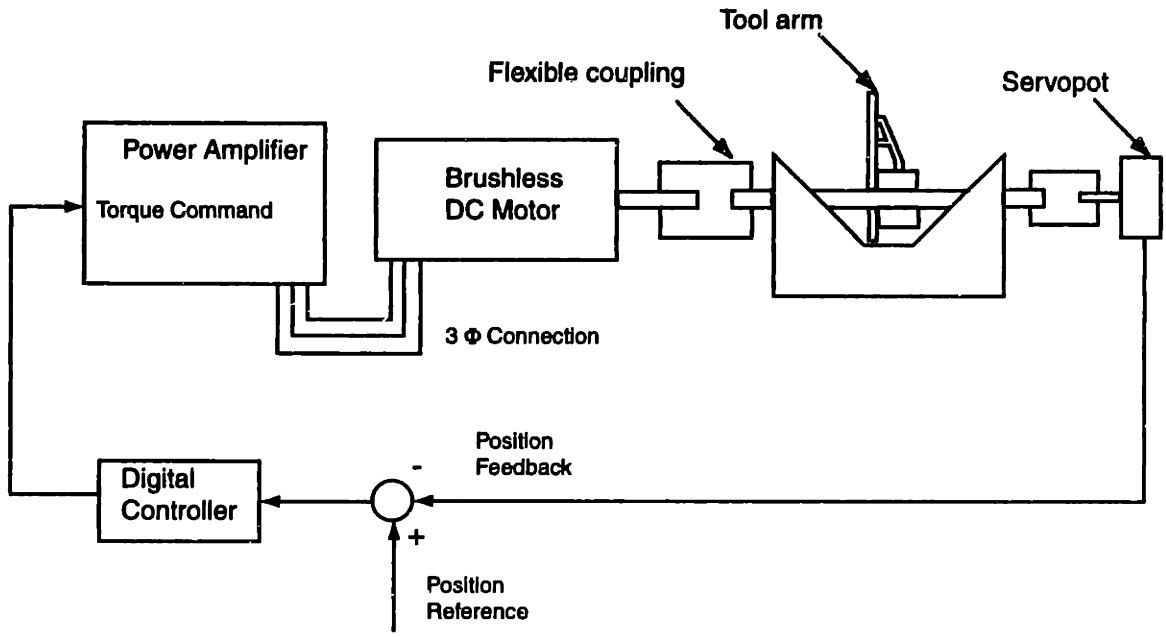

Figure 6-3: Schematic of the testbed.

shown. At low frequencies, the plant does not follow the commanded signals well and the output is much lower than predicted. This is believed to be due to frictional effects, because the system responds more accurately to higher amplitude commands where the velocities are higher and stiction has less of an effect. Another possibility is that the motor cogging, where the permanent magnets in the rotor are aligning with iron in the stator, is acting like a spring to pull the rotor to certain positions.

6.2 PID Control

To give us DC stiffness and bandwidth, we implement integral control with a phase-lead compensator G_c which has the following form in the continuous-time domain

$$G_c(s) = K_p \left(\frac{K_I s + 1}{s}\right)\left(\frac{K_D s + 1}{\alpha K_D s + 1}\right) \tag{6.2}$$

In this case, the controller gains are $K_p = 9200$ Nm/rad, $K_I = 0.01$ sec/rad, $K_D = 0.01$ sec/rad, and $\alpha = 0.05$. The difference equation for implementation in the discrete time domain can be found by a Zero Order Hold approximation with a sampling time

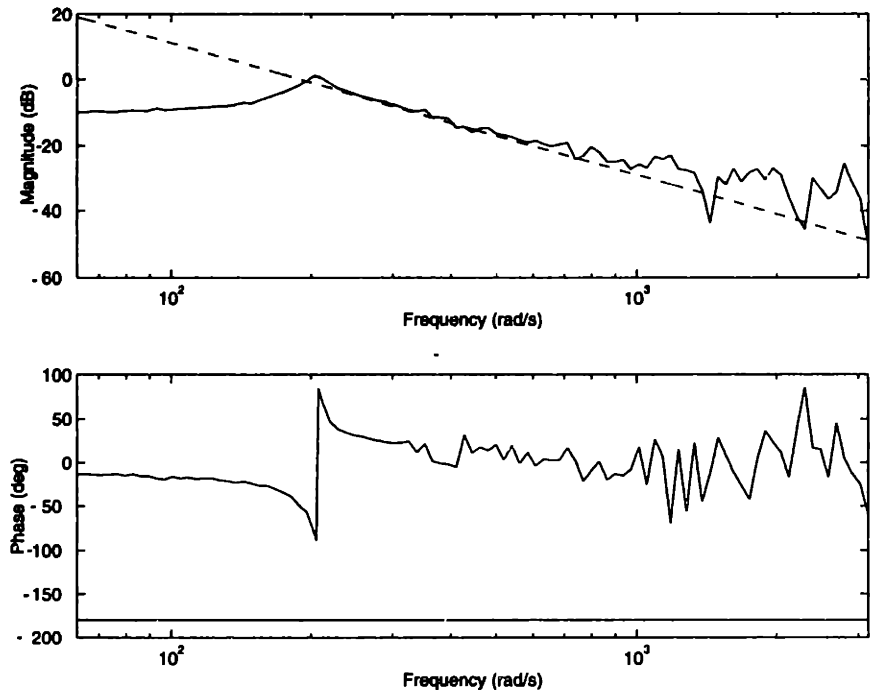

Figure 6-4: Open loop frequency response of the system.

T_s of 0.0001 seconds. This gives a discrete time controller $G_c(z^{-1})$ of

$$G(z^{-1}) = \frac{1836 - 3638z^{-1} + 1802z^{-2}}{1 - 1.819z^{-1} + 0.8187z^{-2}} \tag{6.3}$$

Figure 6-5 shows the predicted loop transmission frequency response with the PID controller. The crossover frequency ω_c is predicted to be 608 rad/s (96 Hz) and the phase margin PM at crossover is predicted to be 54°. With the PID controller designed above, the predicted and measured closed-loop frequency responses are shown in Figure 6-6. As shown, the closed-loop bandwidth is approximately 130 Hz. The torsional mode of resonance can be seen at approximately 5020 rad/s (800 Hz). In general, there are several approaches to dealing with the resonance in the system. Perhaps the most effective is to increase the damping in the system. As discussed in Chapter 3, previous efforts to damp the first coupling used, the Zero-Max SC-050, were unsuccessful. However, a constrained layer damper may be more effective with the Gam Jakob coupling. Another approach is transmission loop-shaping either by a notch filter or by placing poles before the resonance to attenuate the frequency

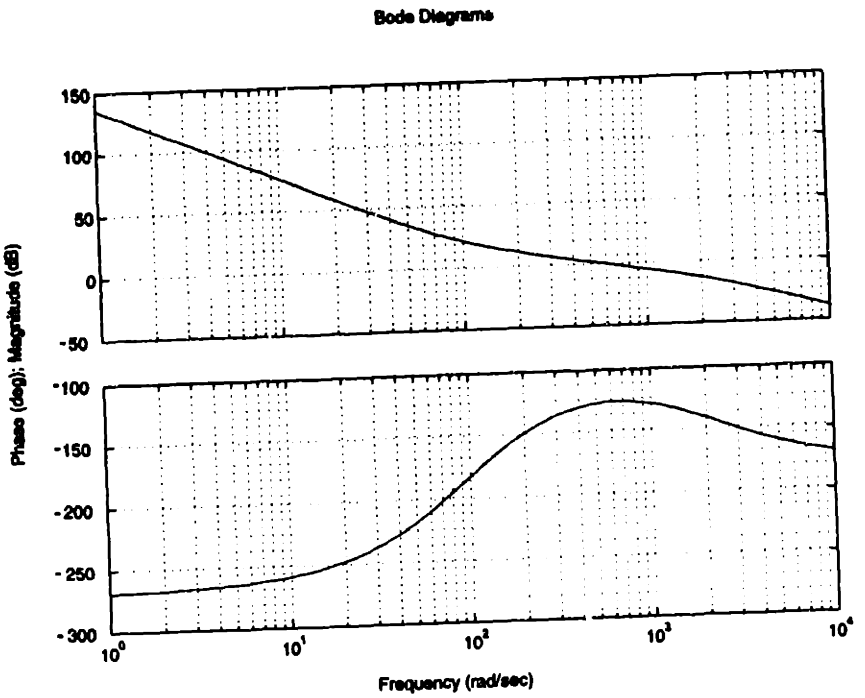

Figure 6-5: Loop transmission of plant with PID control.

response near the resonant frequency. In the prototype machine, we will continue to address this issue, but not as part of this thesis.

6.3 Loop-shaping to Increase Dynamic Stiffness

6.3.1 The Loop-shaping Controller

The dynamic compliance of the servo loop is the angular displacement θ of the shaft as a result of some disturbance torque $D(s)$. Typically with PID control, the integrator gives the servo loop a high degree of DC stiffness, and the dynamic stiffness within the bandwidth of the system is determined by the controller. At frequencies above the bandwidth of the servo loop, the dynamic stiffness is high because the inertia of the system acts as a low-pass filter, i.e. the response of the system to high frequencies is small. During operation, we know that most of the disturbances to the system will be from cutting forces and will come at harmonics of the spindle frequency. Therefore, while we desire high dynamic stiffness or low dynamic compliance at all frequencies, it is critical that the servo loop be stiff at certain known frequencies. In this section,

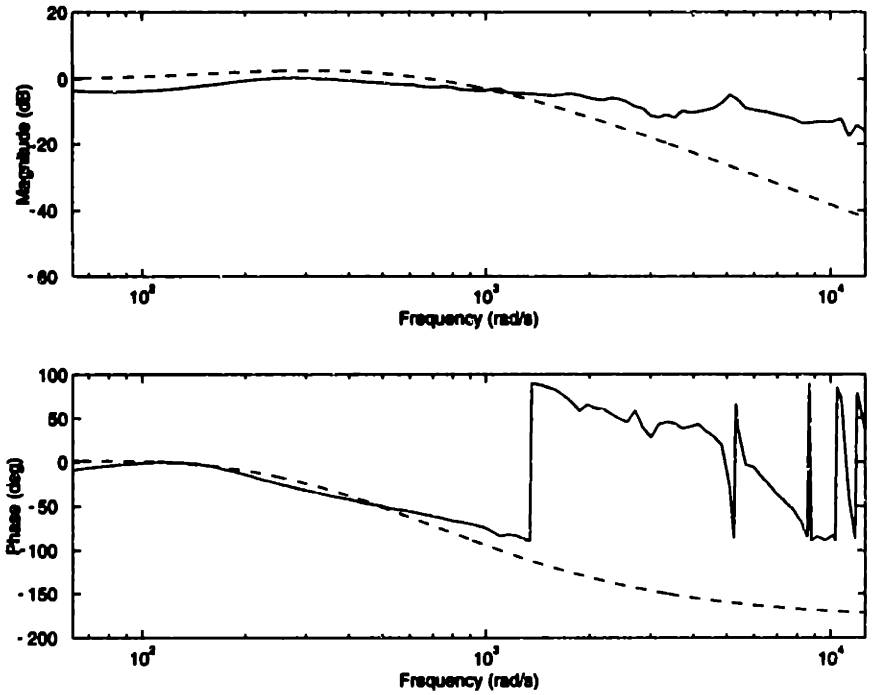

Figure 6-6: Closed loop frequency response with PID control.

we detail a method of increasing the servo loop's dynamic stiffness by shaping the loop transmission frequency response.

In our experiments, we inject a disturbance voltage $D(s)$ with a variable frequency between the output of the D/A and the power amplifier. In a block diagram, this is equivalent to introducing a disturbance between the control algorithm and K_A in Figure 6-7. In essence, the disturbance voltage becomes a torque disturbance after passing through the power amplifier and is a fair simulation of the effect of cutting forces on the servo loop. If $G(s)$ is $\frac{K_A K_M K_S}{Js^2}$ and the control algorithm is $G_c(s)$ = (PD with LoopShaping), then with the feedback shown in the block diagram, $\theta(s)$ is

$$\theta = G(s)\left[-D(s) - \theta(s)G_c(s)\right], \tag{6.4}$$

Rearranging, the transfer function between $\theta(s)$ and $D(s)$, the dynamic compliance, is then

$$\frac{-\theta(s)}{D(s)} = \frac{G(s)}{1 + G_c(s)G(s)}. \tag{6.5}$$

This is actually the negative dynamic compliance, but we will assume we are work-

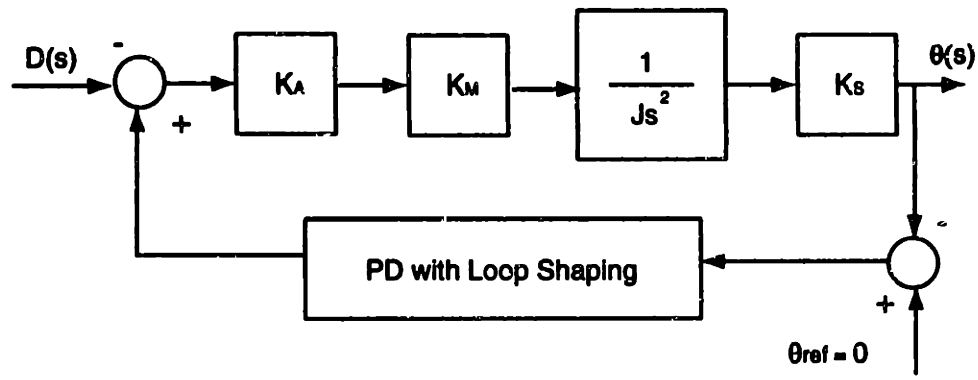

Figure 6-7: Block diagram of disturbance input.

ing with just the dynamic compliance and phase shift our experimentally measured frequency responses accordingly.

To stabilize the plant and to give us bandwidth in order to implement the loop-shaping, we first implement a phase lead compensator $PD(s)$ which has the following form in the continuous time domain

$$PD(s) = K_p \frac{K_D s + 1}{\alpha K_D s + 1}. \tag{6.6}$$

In this case, the controller gains are $K_p = 67$ Nm/rad, $K_D = 0.01$ sec/rad, and $\alpha = 0.05$.

For the loop-shaping, we add in series a controller G_L which has the form

$$G_L(s) = \frac{s^2 + 2k_r\zeta\omega_r + \omega_r^2}{s^2 + 2\zeta\omega_r + \omega_r^2}. \tag{6.7}$$

$G_L(s)$ can be thought of as a resonant pole pair at ω_r and a more strongly damped resonant zero pair at the same frequency. Here, ω_r corresponds to the expected frequency of the disturbances. We can get a stronger intuitive feeling for the effect of the controller by looking at the poles and zeros plotted on the Im(s) and Re(s) axis in Figure 6-8. Referring to Figure 6-8, we can see that increasing k_r forces the zeros to be more strongly damped. Decreasing ζ decreases the real part of the pole pair. Next, we look at the effects of varying k_r and ζ.

Design with the controller can be thought of as loop-shaping, and it is helpful to

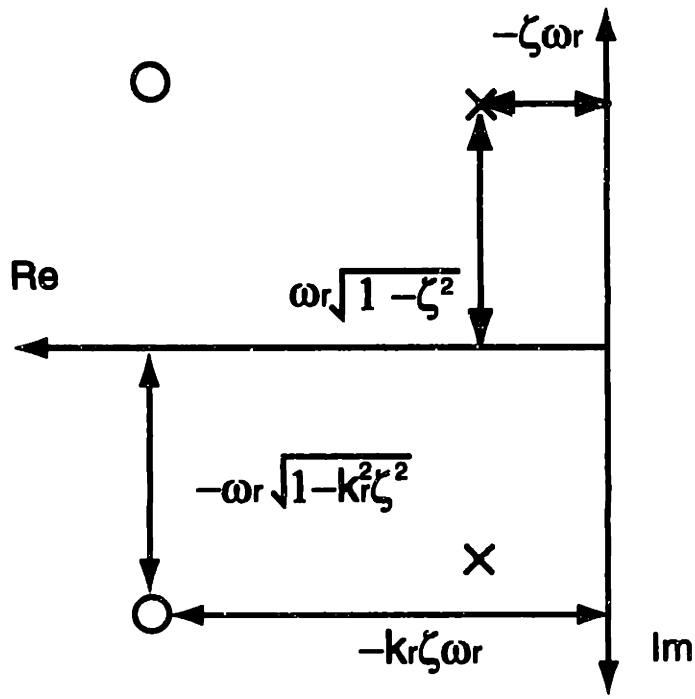

Figure 6-8: Plot of poles and zeros of loop shaping controller

consider the effects of changing the parameters of the controller on the loop transmission frequency response as well as the dynamic compliance. To begin, we simulate the loop transmission frequency response of the plant with the phase-lead compensator $PD(s)$ designed previously. The crossover frequency is predicted to be 550 rad/s (88 Hz), and the phase margin is 64°. Next, we select the loop-shaping controller gains to be, $w_r = 126$ rad/s (20 Hz) and $\zeta = 0.05$. Then, we analyze the effect of increasing k_r from 10 to 50 in increments of 10. The loop transmission frequency response is shown in Figure 6-9, and the effect on the dynamic compliance is shown in Figure 6-10. The system's loop transmission frequency response and dynamic compliance with only phase-lead compensation are also plotted as a reference. Referring to Figure 6-10, increasing k_r decreases the dynamic compliance at w_r. Specifically, $k_r = 10$ attenuates a disturbance by an additional 20 dB, while $k_r = 50$ attenuates a disturbance by an additional 34 dB. However, Figure 6-9 shows that we also quickly lose phase margin at ω_c as we increase k_r, which drives the system towards instability.

Loss in phase margin is minimized by decreasing ζ in the loop-shaping controller $G_L(s)$. As we decrease the real part of the resonant poles, we decrease the range

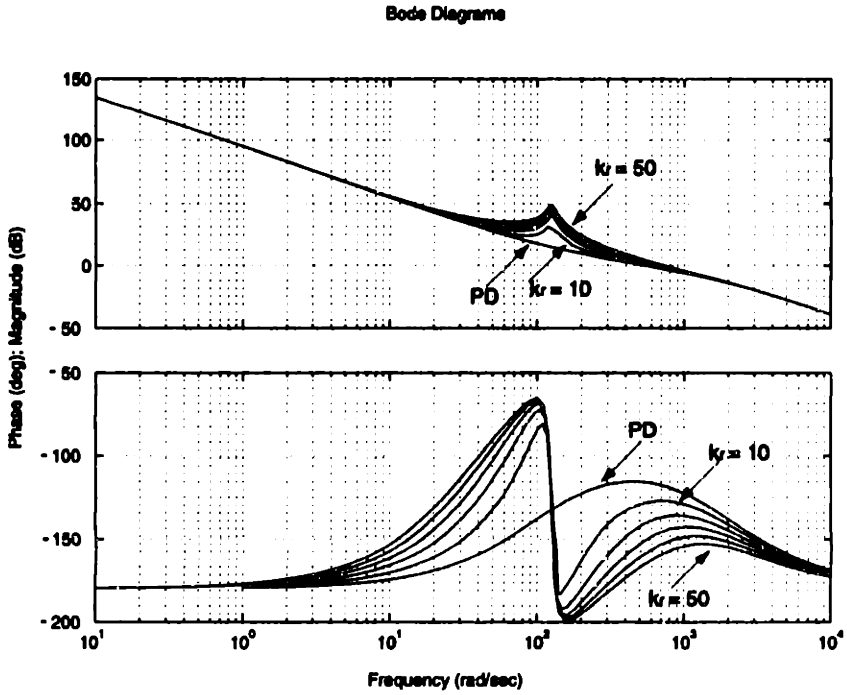

Figure 6-9: Effect of increasing k_r on the system's loop transmission frequency response.

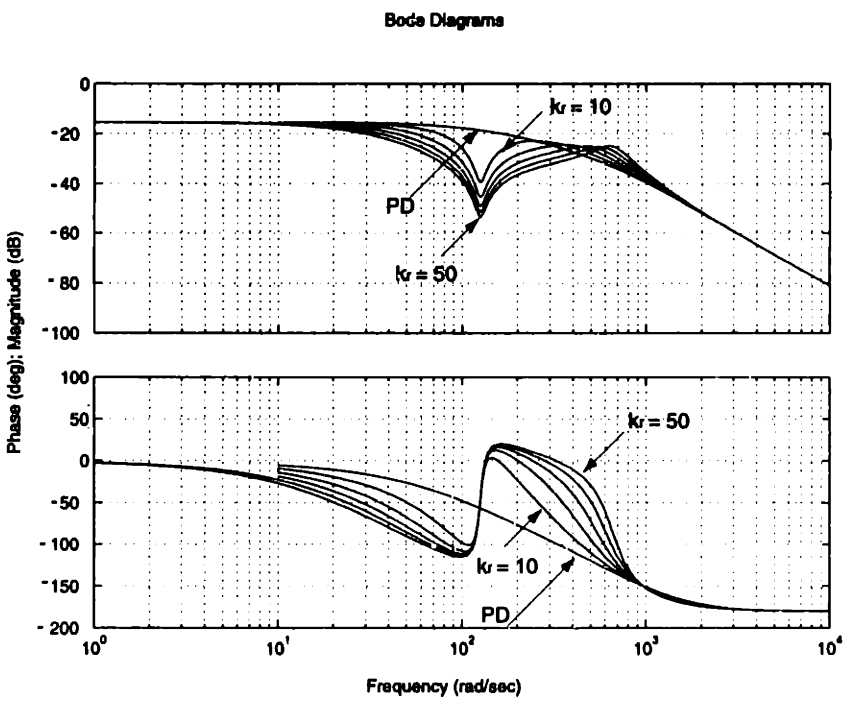

Figure 6-10: Effect of increasing k_r on the systems dynamic compliance.

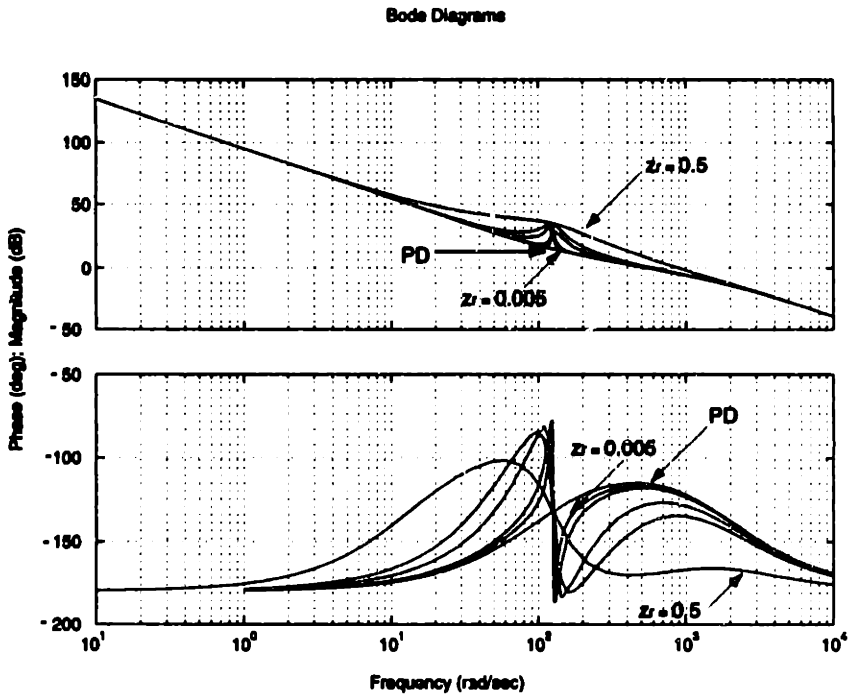

Figure 6-11: Effect of increasing ζ_r on the system's loop transmission frequency response.

of frequencies over which the phase change due to the controller resonance occurs. This allows us to recover phase margin more quickly. To see the effect of varying ζ, we again set $\omega_r = 20$ Hz and $k_r = 10$. Then, we vary ζ from 0.05 to 0.005 in 0.005 increments. The system's loop transmission frequency response is shown in Figure 6-11, and the effect on the dynamic compliance is shown in Figure 6-12. Again, the system's loop transmission frequency response and dynamic compliance with only phase-lead compensation are also plotted as a reference. Referring to Figure 6-11, we can see that by decreasing ζ we are able to limit the phase change to a small range of frequencies. Thus, most of the phase margin has been recovered at the point of crossover. The disadvantage in decreasing ζ can be seen in Figure 6-12. As ζ decreases, the range of frequencies over which the loop-shaping controller attenuates disturbances is reduced. For our application, the range of frequencies over which attenuation is needed is determined by how precisely the frequency of the disturbance input is known.

Given that any direct-drive system will have a limited servo bandwidth, the chal-

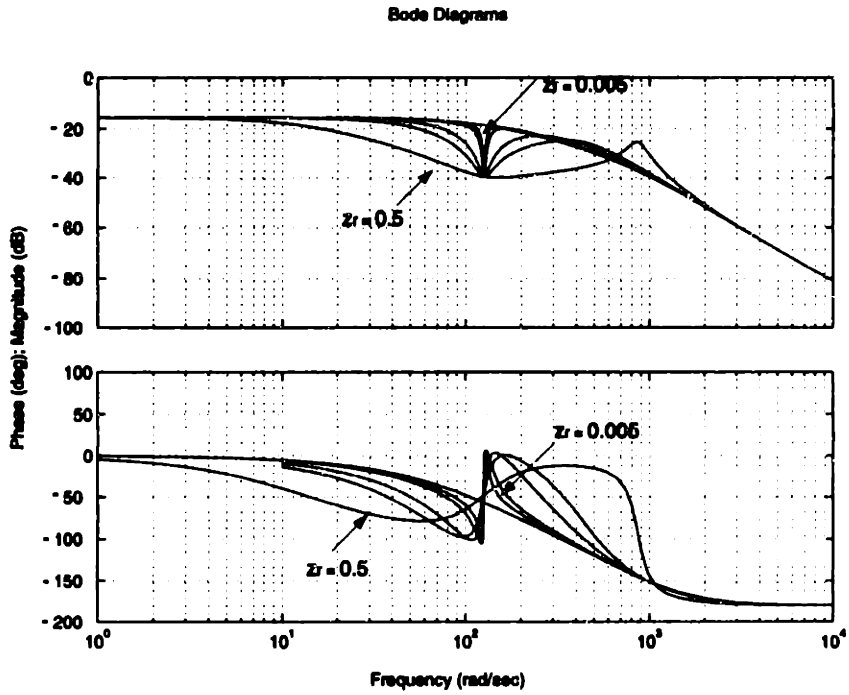

Figure 6-12: Effect of increasing ζ_r on the systems dynamic compliance.

lenge is to design a loop-shaping controller that will provide as much dynamic stiffness at a specified frequency as needed and maintain enough phase margin to keep the system stable.

6.3.2 Loop-shaping Controller Implementation

From the previous section, the controller G_c is the combination of the phase-lead compensator $PD(s)$ and the loop shaping controller $G_L(s)$

$$G_c(s) = PD(s)G_L(s) = K_P \frac{K_D s + 1}{\alpha K_D s + 1} \frac{s^2 + 2k_r\zeta\omega_r + \omega_r^2}{s^2 + 2\zeta\omega_r + \omega_r^2} \tag{6.8}$$

The phase-lead compensator is the same as in the previous section and the gains of the loop-shaping controller are $k_r = 30$, $\zeta = 0.001$, and $\omega_r = 251$ rad/s (40 Hz). The difference equation for implementation in the discrete time domain is found by a Tustin approximation with a sampling time T_s of 0.0001 seconds and prewarped at

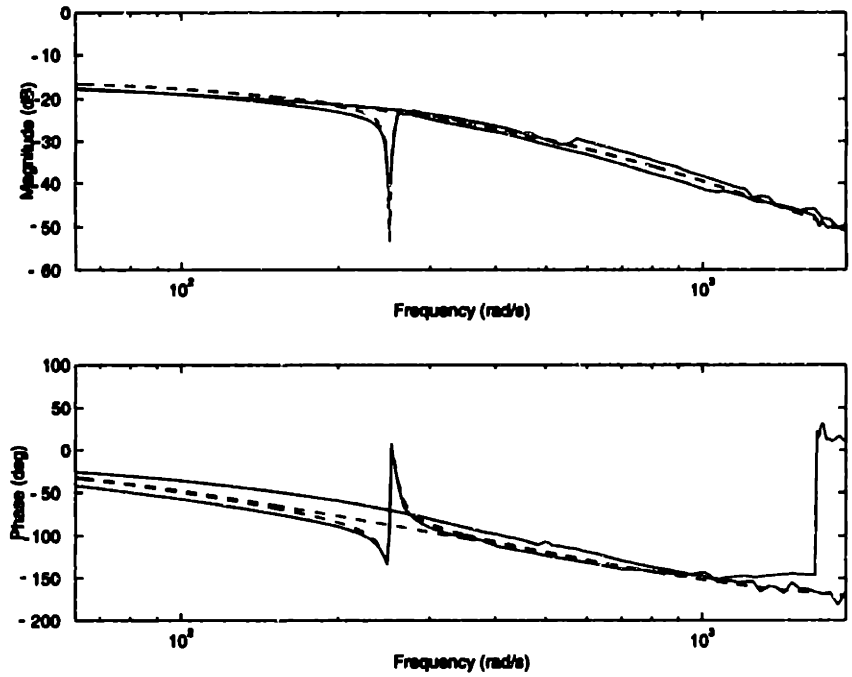

Figure 6-13: Measured and predicted dynamic compliance with and without repetitive controller.

w_r. This gives a discrete time controller $G_c(z^{-1})$ of

$$G_c(z^{-1}) = \frac{1225.15939 - 3660.66773z^{-1} + 3646.65661z^{-2} - 1211.14057z^{-3}}{1.0 - 2.81749z^{-1} + 2.63573z^{-2} - 0.81813z^{-3}}. \quad (6.9)$$

Figure 6-13 shows the measured and predicted dynamic compliance of the system with and without the loop shaping controller. Figure 6-14 shows the same frequency response over a much smaller frequency range, 39-41 Hz. The peak attenuation with the loop-shaping controller is approximately 54 dB. It also coincides very closely to 40 Hz. Compared to the dynamic compliance without $G_L(s)$, which has an attenuation of approximately 20 dB at 40 Hz, the loop-shaping controller decreases the dynamic compliance by an additional 34 dB. For a physical sense of the dynamic compliance, we can estimate the amount of disturbance torque introduced and compare it to the angular displacement measured through the potentiometer. Injecting a sinusoidal disturbance with a peak voltage of V_D, the peak disturbance torque T_D (Nm) is

$$T_D = K_A K_M V_D. \quad (6.10)$$

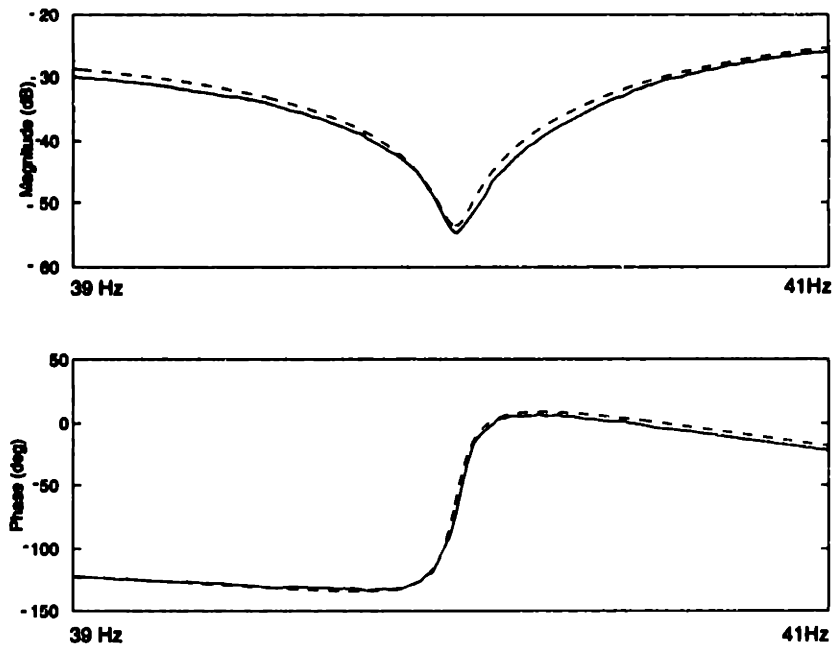

Figure 6-14: Measured and predicted dynamic compliance of loop-shaping controller 39-41 Hz.

The angular displacement θ (rad) corresponding to a voltage output of the potentiometer V_P is

$$\theta = \frac{V_P}{K_s}. \tag{6.11}$$

Rearranging to find the dynamic compliance we obtain

$$\frac{\theta}{T_D} = \frac{1}{K_S K_A K_M} \frac{V_P}{V_D}. \tag{6.12}$$

Therefore, we can estimate the dynamic compliance if we know the attenuation from V_D to V_P. The dynamic compliance of the phase-lead compensator alone, which attenuates a disturbance by approximately 20 dB (a factor of 10) at ω_r, is 8.9 mrad/Nm. For a 100 mm arm, this corresponds to a compliance of 0.89 mm/Nm at the tool. With the loop-shaping controller, which has an attenuation of 54 dB (a factor of 500) at ω_r, the dynamic compliance is 0.18 mrad/Nm. In this case, for a 100 mm arm the system has a dynamic compliance of 0.018 mm/Nm at the tool. The system with the loop-shaping controller combined with the phase-lead compensator has a dynamic

compliance approximately 50 times smaller than the system with only phase-lead compensation. Recall that cutting forces reach 25 N, or 2.5 Nm on a 100 mm arm, during a 2 mm cut in polycarbonate. During a roughing pass, this would result in a deflection of 0.045 mm at the tool, with $G_L(s)$ added to the control algorithm.

6.4 Feedforward Control

6.4.1 The Feedforward Controller

When tracking a sinewave under PID control, the actual trajectory that the rotary fast tool servo follows deviates from the desired trajectory by some amplitude error and with a phase shift. In particular, the phase shift increases as the frequency of the trajectory is increased. For trajectory following, particularly when cutting a toric lens, feedforward control can be used to minimize the amplitude and phase shift errors. The goal of feedforward control is to cancel the dynamics of a plant by multiplying it by its inverse so that there is unity gain between the command to the RFTS and the output. In the ideal case, there would also be no phase shift between the input and the output. Two references that cover the basics of feedforward control are [2] [12]. To simplify the trajectory following tests, we again make the assumption that the tool will be following a perfect sinusoid during cutting. The results though, can be applied to the actual cutting trajectories through Fourier analysis.

There are a number of different implementations of feedforward control, shown in Figure 6-15. In Figure 6-15, $\frac{1}{Js^2}$ is the inertia of the plant, G_c is the PID controller, G_{FF} is the feedforward controller, θ_d is the desired output and θ_A is the actual output. In case a), the feedforward controller is designed as the inverse of the closed-loop plant, and the block diagram reduces to

$$\frac{\theta_A}{\theta_d} = G_{FF}\frac{G_c}{Js^2 + G_c}. \tag{6.13}$$

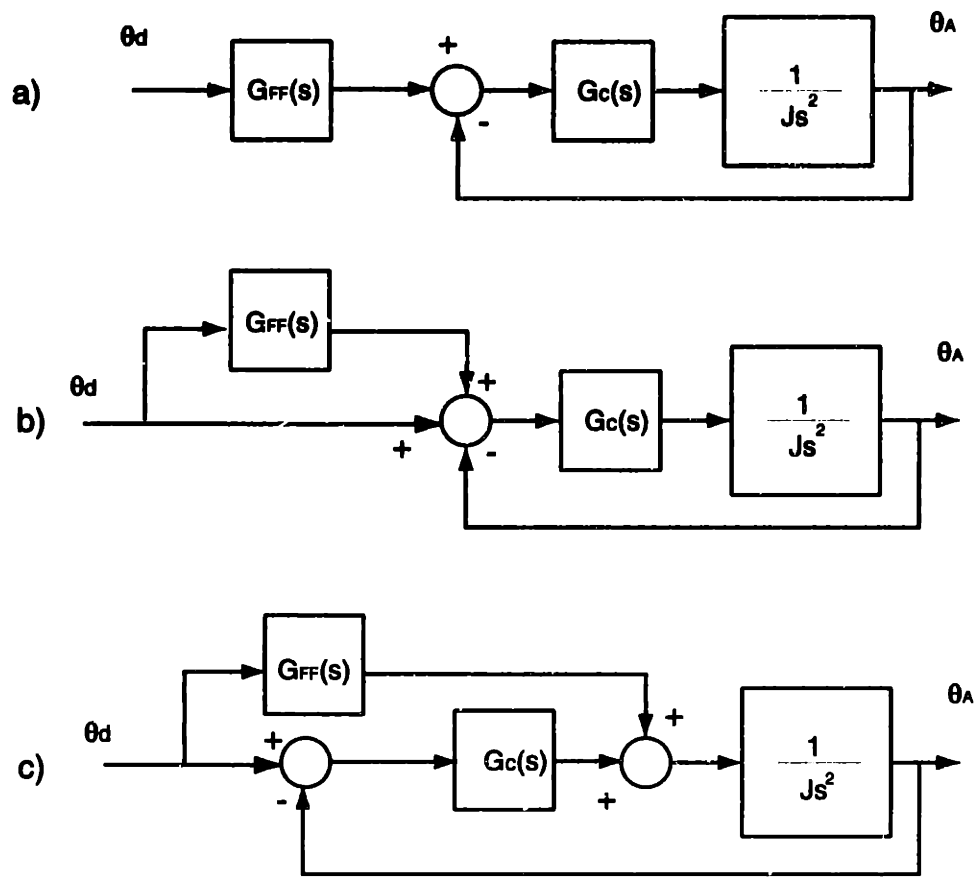

Figure 6-15: Implementation of feedforward control.

In order for there to be unity gain between θ_A and θ_d we must have

$$G_{FF} = \frac{\hat{J}s^2 + G_c}{G_c}, \tag{6.14}$$

where $\hat{J}$ is a model of the plant inertia. A digital implementation of this form, called Zero Phase Error Tracking Control (ZPETC), has been studied for trajectory following and noncircular turning in [21] [22].

In case b), the feedforward controller is $\frac{Js^2}{G_c}$ and θ_A is

$$\theta_A = \left(\theta_d - \theta_A + \frac{\hat{J}s^2}{G_c}\theta_d\right)\frac{G_c}{Js^2}, \tag{6.15}$$

which reduces to

$$\frac{\theta_A}{\theta_d} = \frac{\hat{J}s^2 + G_c}{Js^2 + G_c}. \tag{6.16}$$

In case c), the feedforward controller is Js^2 and θ_A is

$$\theta_A = \frac{G_c}{Js^2}(\theta_d - \theta_A) + \theta_d\frac{\hat{J}s^2}{Js^2}, \tag{6.17}$$

which reduces to

$$\frac{\theta_A}{\theta_d} = \frac{\hat{J}s^2 + G_c}{Js^2 + G_c}. \tag{6.18}$$

We are still investigating the best implementation of feedforward control and how to best tune parameters of the controller.

For the next section, the feedforward controller of case a) and c) are developed. In the discrete-time domain, the feedforward controller in case a) is represented in Figure 6-16. The closed-loop system is the plant under PID control, where $\frac{A_c(z^{-1})}{B_c(z^{-1})}$ is the closed-loop transfer function with a time delay of z^{-d}. As described earlier, the feedforward controller is the inverse of the closed loop system. The command input $\theta_d(k+d)$ is d steps ahead because of the delay z^{-d} in the system. If there were uncancellable poles in the system, roots of $A_c(z^{-1})$ outside the unit circle, then the plant could not be stably inverted [21]. Now the control input to the closed-loop

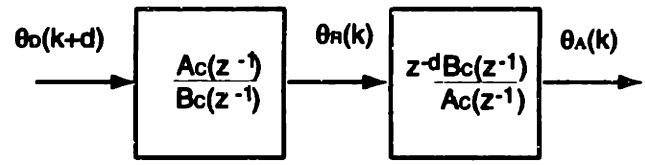

Figure 6-16: Discrete implementation of feedforward control.

transfer function becomes

$$\theta_R(k) = \frac{A_c(z^{-1})}{B_c(z^{-1})}\theta_d(k+d). \tag{6.19}$$

This form of feedforward control, when implemented, has been sensitive to modeling errors of the plant. The original command $\theta_d(k+d)$ is lost, because the feedforward filter is in series with the command. Therefore, the error that the feedback loop acts on is $\theta_R - \theta_A$. If there is any error in our model, the feedforward filter will not cancel the plant perfectly, and the command to the plant θ_R will not drive the system to position θ_d. In other words, there will be a steady-state error. Also, because of the placement of G_{FF}, the form of the feedforward filter depends on the feedback controller $G_c(s)$, as seen in eq. 6.14. Thus, whenever the feedback controller's parameters are adjusted, the feedforward filter has to be changed as well.

In case c), the s^2 term in the feedforward term is difficult to implement because it requires infinite gain at high frequencies, similar to the case of derivative control without phase lead compensation in PID control. To attenuate the gain at high frequencies, we can place additional poles in G_{FF} such that their phase lags do not effect the dynamics of the feedforward filter in the bandwidth of the system.

For our implementation, the feedforward filter $G_{FF}(s)$ is in the form

$$G_{FF}(s) = \frac{\hat{J}s^2}{(K_{FF}s+1)^n}, \tag{6.20}$$

where $\hat{J}$ is our estimate of the system inertia, 1.67×10^{-3} kg-m^2, K_{FF} is the pole location, and n is the number of poles. Since we are now working on the prototype machine, the inertia of the system has changed slightly from the testbed system

inertia. This is primarily because adding the Gam Jakob KR-65 coupling has slightly increased the inertia of the system. Next, we select $K_{FF} = 1.59 \times 10^{-4}$ and $n = 8$, which places the eight poles at 6283 rad/s (1 kHz). The discrete-time feedforward controller $G_{FF}(z^{-1})$ can be found by a ZOH approximation with a sampling time $T_s = 0.0001$ s,

$$G_{FF}(z^{-1}) = \frac{a(z^{-1})}{b(z^{-1})} \tag{6.21}$$

where

$$\begin{aligned} a(z^{-1}) &= 2.439z^{-1} + 62.23z^{-2} + 40.71z^{-3} - 193.6z^{-4} \\ &\quad +11.82z^{-5} + 68.7z^{-6} + 7.672z^{-7} + 0.0674z^{-8}; \\ b(z^{-1}) &= 1 - 4.269z^{-1} + 7.973z^{-2} - 8.508z^{-3} + 5.675z^{-4} \\ &\quad -2.423z^{-5} + 0.6464z^{-6} - 0.09854z^{-7} + 0.006573z^{-8}. \end{aligned}$$

While $n = 8$ may seem to be a large number of poles, the feedforward filter requires significant attenuation at high frequencies. The predicted frequency response of $G_{FF}(z^{-1})$ is shown in Figure 6-17. We can see that even with 8 poles at 6283 rad/s, the filter gain is still 15 dB at the Nyquist frequency 31400 rad/s (5 kHz). For low frequencies, the feedforward filter's frequency response looks like a inverted mass Js^2. Starting at 6282 rad/s, the attenuation is -120 dB/decade. If we desire a closed loop bandwidth under PID control of 628 rad/s (100 Hz), we can see the phase shift from the additional poles remains small for frequencies up to 628 rad/s.

6.4.2 Feedforward Control Implementation

Feedforward control has been implemented on the prototype turning machine. The PID controller has the same form as in eq. 6.2. In this case, the gains are $K_P = 6400$ Nm/rad, $K_D = 0.1$, $\alpha = 0.05$, and $K_I = 0.1$. The only change from the PID controller implemented on the testbed is that the proportional gain K_P has been lowered. This is because the noise level in the RFTS axis has increased in the prototype machine's

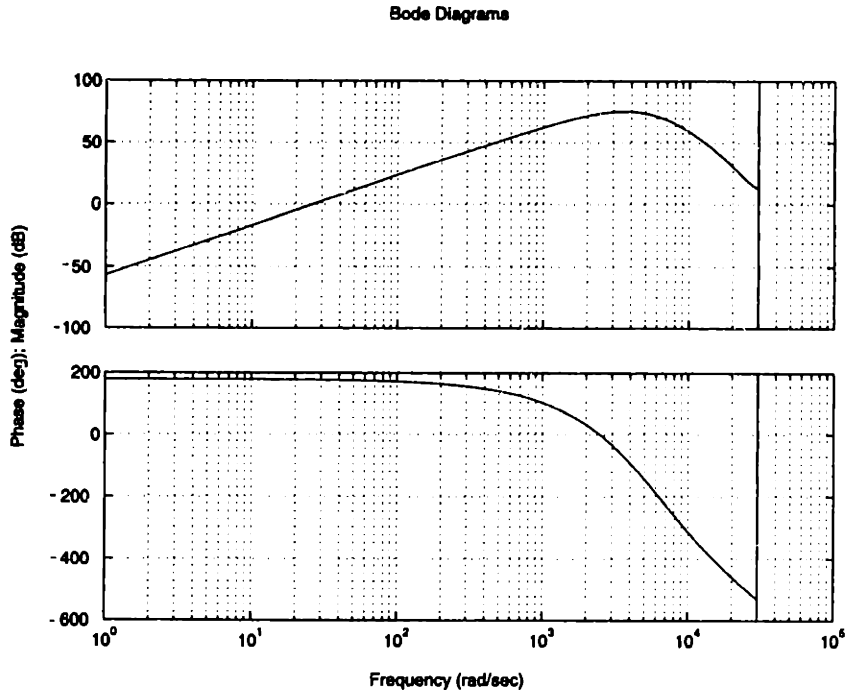

Figure 6-17: Frequency response of the feedforward filter.

new environment. Currently, we are working on proper shielding and grounding of the components. Figure 6-18 shows the predicted and measured closed-loop position frequency response of the RFTS under PID control. The bandwidth of the frequency response is approximately 628 rad/s (100 Hz). Figure 6-19 shows the predicted and measured closed-loop position frequency response of the RFTS axis under PID and feedforward control. For frequencies below 300 rad/s (48 Hz), the magnitude of the frequency remains close to 0 dB, unity gain. At higher frequencies, the magnitude begins to rise, up to 4.5 dB at 1000 rad/s (160 Hz). This may be due to modeling inaccuracies. If our plant model $\hat{J}s^2$ does not exactly cancel the plant $\frac{1}{Js^2}$, then the error would be more noticeable at higher frequencies due to the s^2 term. After preliminary tuning of the feedforward filter, we have adjusted the plant model to $\hat{J} = 1.76 \times 10^{-3}$ kg-m^2. Figure 6-19 is the response for the adjusted $\hat{J}$. Figure 6-20 compares the measured closed-loop position frequency responses of the RFTS, with and without feedforward control. At 300 rad/s, the phase shift of the RFTS's trajectory with feedforward control is only $-13°$. Without feedforward control, the RFTS's trajectory lags by $-47°$ at 300 rad/s.

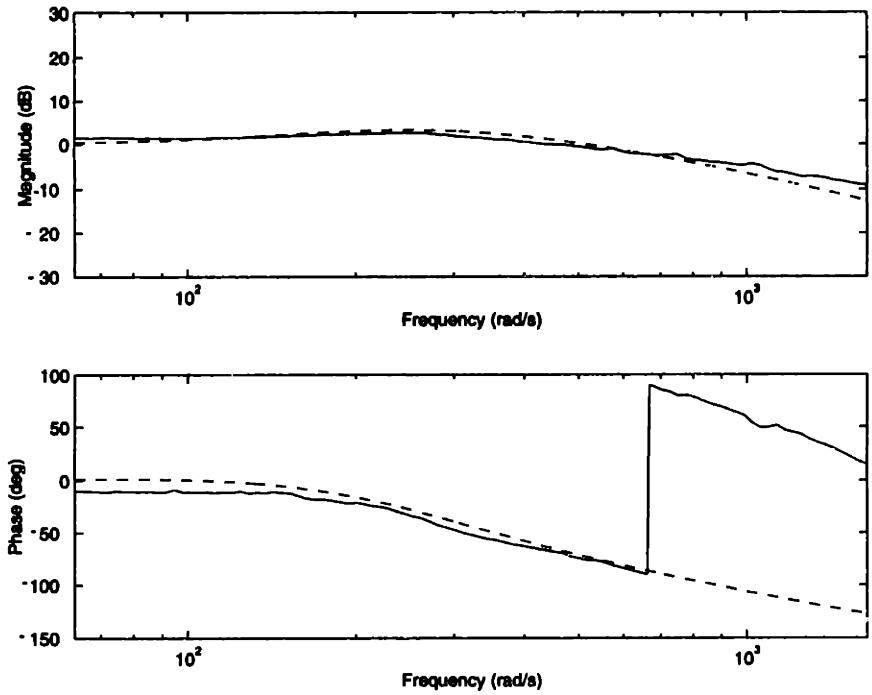

Figure 6-18: Measured and predicted closed-loop position frequency response under PID control.

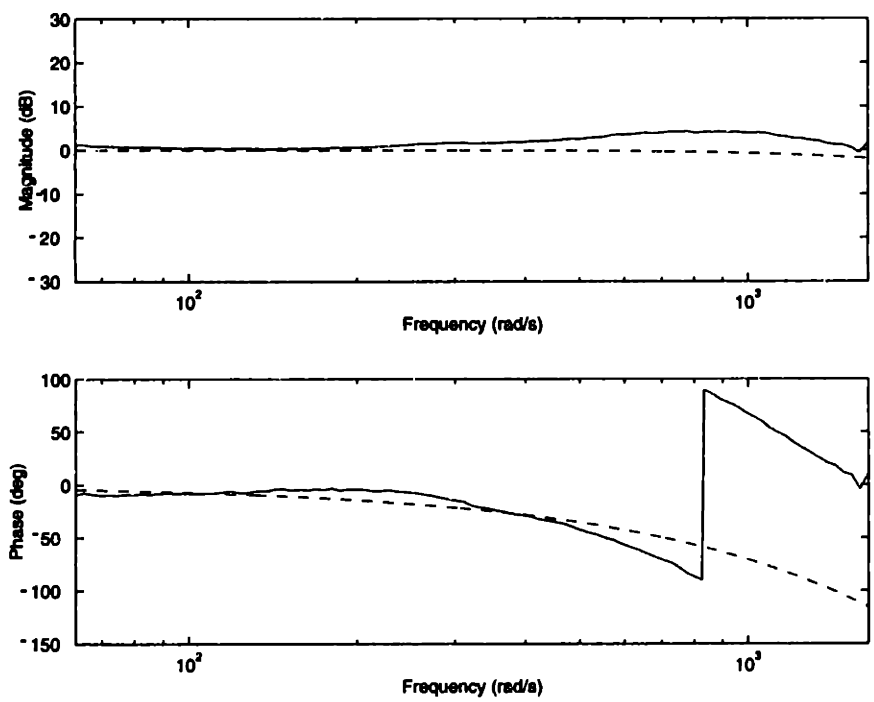

Figure 6-19: Measured and predicted closed-loop position frequency response under PID and feedforward control.

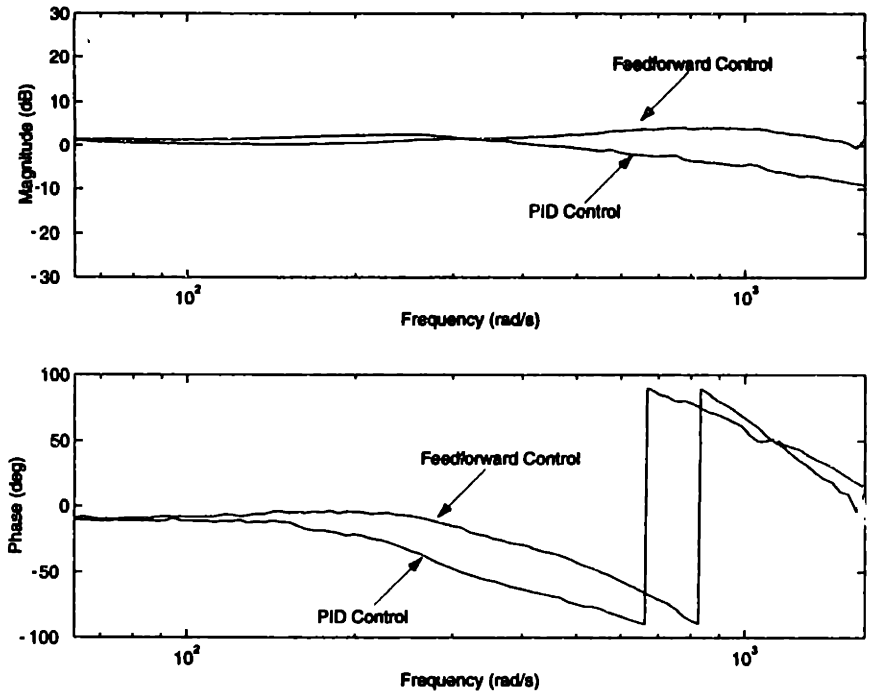

Figure 6-20: Measured closed loop position frequency responses with and without feedforward control.

Figure 6-21 shows the RFTS, without feedforward control, tracking a 30 Hz sinewave with an amplitude of 0.01 rad. Figure 6-22 shows the RFTS tracking the same trajectory with feedforward control added. A tool frequency of 30 Hz corresponds to a spindle speed of 900 RPM. In Figure 6-21 we can see that the amplitude error and the phase shift of the measured trajectory are significant. The peak error is 4.1 mrad and the standard deviation of the error is 2.5 mrad. In Figure 6-22, feedforward control has greatly reduced the amplitude error and the phase shift of the measured trajectory. The peak error 1.4 mrad and the standard deviation of the error is 0.70 mrad. Feedforward control has reduced the tracking error by a factor of 4.

For a 100 mm tool arm, an error of 1 mrad corresponds to 100 μm. Most of this tracking error seems to occur at the peak of the trajectory where the contour that the RFTS traces seems to be asymmetric. This could be due to static friction, because at the peak of the trajectory, the velocity of the tool is zero or very small as it reverses direction. The largest error comes just after the reversal of direction. Along the trajectory where the velocities are higher, the tool tracks the commanded trajectory

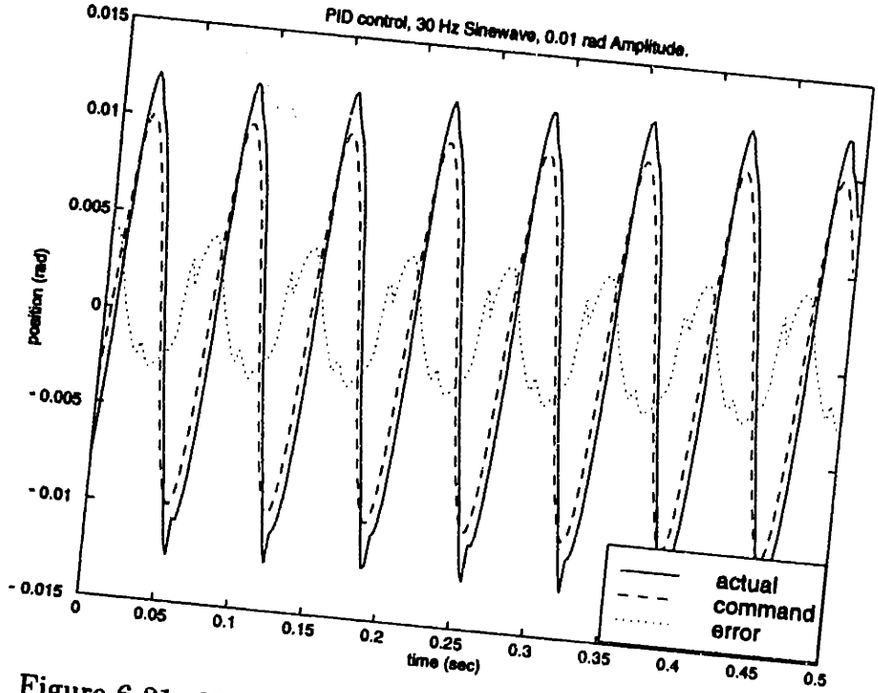

Figure 6-21: 30 Hz sinewave without feedforward control.

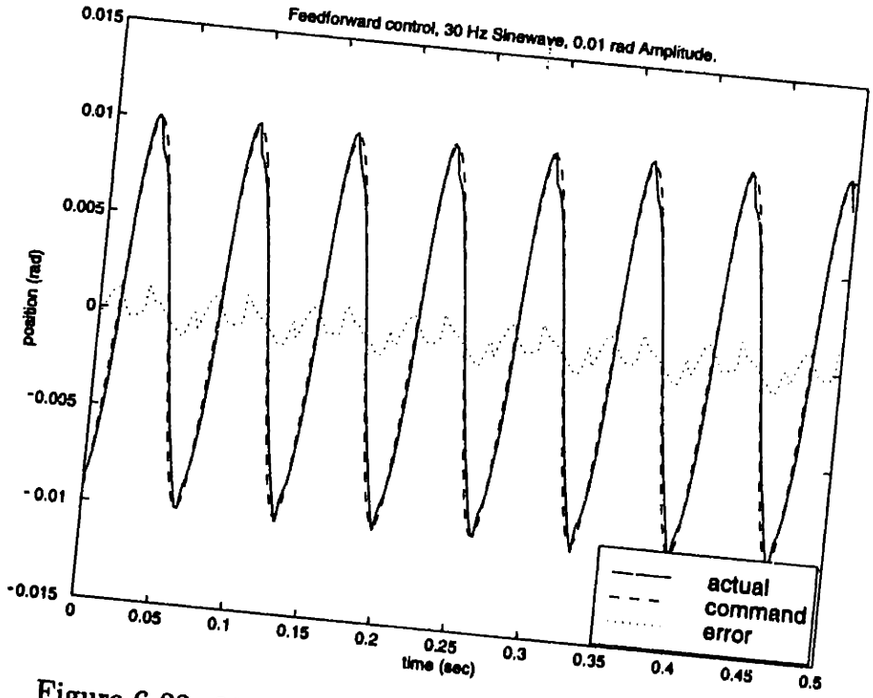

Figure 6-22: 30 Hz sinewave with feedforward control.

very well. Therefore, to reduce the tracking error, friction compensation may have to added in the future. The tracking error of the RFTS can also be decreased with a more accurate model of the plant. As mentioned before, modeling inaccuracies start affecting the amplitude error more at higher frequencies, because of the $\hat{J}s^2$ term in the feedforward filter. Some amount of preliminary tuning has been done to reduce the tracking error. Although, we are finding that gross inaccuracies in modeling are relatively easy to tune, however small inaccuracies are more difficult.

Chapter 7

Conclusions and Suggestions for Future Work

In this thesis we have described the design and implementation of a rotary fast tool servo (RFTS) axis for an ophthalmic lens turning machine. My research these past two years has focused specifically on selecting and benchmarking the performance of different components on a testbed for the RFTS axis. This work then led to the fabrication of a second-generation RFTS axis that will be installed on the prototype turning machine. One of the underlying themes of this research is to try to predict the performance of components and then testing them to verify their performance. The strategy behind this approach is that we wanted to work through the details of the mechanical design on a testbed, and have the design finalized before building the second-generation RFTS axis.

In terms of individual components, we have discussed the selection of the servo motor, the tool arm bearings, the flexible coupling, and the rotary sensor. After comparing motors from various motor manufacturers, we have shown that motors with high torque-to-inertia ratios and low armature inductance are needed to drive the RFTS. In general, DC brushless motors have the highest torque-to-inertia ratios of conventional servomotors. However, among the DC brushless motors we surveyed, some have unacceptably large armature inductances. Driving these motors at high accelerations and commanding high frequency trajectories risks saturating the power

amplifier. By properly selecting the servo motor, the RFTS can be used to cut lenses at high spindle speeds. For example, we have shown that the Aerotech DC brushless motor is capable of high torque outputs at frequencies up to 300 Hz.

Future work on this subject includes integrating the tool arm shaft into the servo-motor. This will eliminate the flexible coupling between the motor shaft and the tool arm shaft. It will also eliminate the bearings in the motor, which are less accurate than the ABEC-9 bearings. In the current project, if the motor bearings influence the cutting accuracy of the RFTS, it may be necessary to replace the current motor bearings with higher precision bearings.

Another issue is the selection of bearings for the tool arm shaft. In order to meet the desired cutting accuracies, we require the bearings to have submicron error motions and submicron deflections under cutting forces. We have shown that precision ABEC-9 ball bearings have the necessary stiffness, accuracy, and resolution for our application. ABEC-9 bearings are the highest accuracy bearings currently available and are more expensive than typical precision ball bearings. However, when compared to the cost and development time associated with designing and building custom air or hydrostatic bearings, ABEC-9 bearings appear to be extremely economical.

One problem with the bearings that is still unresolved is the machining of the bearing bores. In the current design, the bearing bores are the most difficult features to make and hence the most costly. With the expertise of a company familiar with mass production, fixtures and jigs may bring down the cost of machining the bores. As mentioned before, replicating the bores is an attractive option because it would make the bearing bores a relatively low accuracy feature. As a manufacturing process, this idea still needs to be tested. Specifically, aligning the tool arm shaft and bearings before casting them in may be difficult.

Selecting a proper flexible coupling has proven to be difficult. Currently we are using a Gam Jakob, bellows-type, flexible coupling. For now, it appears to be the best off-the-shelf solution available. The torsional mode of resonance will hopefully be pushed above 1 kHz when all the components are installed on the prototype machine. More work needs to be done to determine how to best damp the coupling whether by

passive or active means.

As far as measuring the error in the lenses, a methodology has been established to measure the form error in spherical lenses down to the micron level. When we come close to meeting our target accuracy specifications, a methodology will be needed to measure the lenses on a sub-micron scale. Also, a means to measure toric lenses, where the form errors are the largest, needs to be found.

The control algorithms implemented so far have been the beginning of continuing work on the RFTS. To achieve higher bandwidths, the torsional mode of resonance needs to be moved higher and/or better damped. A high resolution encoder, donated by MicroE, is being installed on the RFTS axis. This should aid us by reducing the noise injected into the system through the servopot. We have also shown how the dynamic stiffness of the servo loop can be increased by loop shaping techniques. In our tests, the servo loop's dynamic stiffness has been increased by a factor of 50 for certain frequencies. Feedforward control has also been implemented to reduce the phase lag of the RFTS while tracking high frequency trajectories.

In conclusion, we have shown that the rotary fast tool servo concept has the potential to make significant contributions to the field of machining nonrotationally symmetric parts, in this case ophthalmic lenses. First, in terms of acceleration capability, rotary fast tool servos are capable of much higher accelerations than linear fast tool servos. The prototype RFTS has a tangential acceleration of approximately 50 g at the tool. Conventional linear fast tool servos, in machines used to cut eyeglass lenses, have acceleration capabilities of well under 10 g. With higher acceleration comes the capability to machine lenses at higher spindle speeds and feedrates to increase throughput. Second, when we consider the negligible vibrations from the reaction force of accelerating the tool during cutting, the RFTS has another significant advantage over conventional linear fast tool servos. Third, in terms of cutting accuracy, we have shown that with careful mechanical design we should be able to meet the specified cutting accuracy of 1 μmm over 10 mm of the lens's surface. Thus far, we have carefully tested such components as the bearings in terms of accuracy and stiffness. As we design new components, such as the new tool arm, stiffness and

accuracy will continue to be benchmarked and verified. Eventually, cutting lenses more accurately may eliminate the need to use a hard lap to polish the lenses. This would significantly decrease the cost of making ophthalmic lenses by reducing process time and reduce the size of the lens-making operation. Finally, the end goal of the project is to build a machine that not only meets the target specifications, but is also capable of becoming a production machine. Another promising aspect of the RFTS is that the design is simple enough to be built using only off-the-shelf components. Therefore, taking the prototype design and turning it into a production machine is a straightforward path.

Bibliography

[1] Ansi/asme b89.3.4.m, 1985. Standard on rotational axis.

[2] Basics of motion control. *Machine Design*, pages 132–134, April 1995.

[3] P. Bourdet, C. Lartigue, and et. al. Effect of data point distribution and mathematical model on finding the best-fit sphere to data. *Precision Engineering, vol. 15, No. 3*, pages 150–157, Jul 1993.

[4] L. Chaloux. Toric contact lenses on demand. *Optical World*, pages 32–34, February 1996.

[5] J.L. Devore. *Probability and Statistics for Engineering and the Sciences.* Brooks Cole, 1982.

[6] R. Donaldson and P. Patterson. Design and construction of a large vertica-axis diamond turning machine. In *SPIE's 27th Annual International Technical Symposium, Aug. 21-26*, pages 62–75, 1983.

[7] S. Duke-Elder and D. Abrams. *Ophthalmic Optics and Refraction.* The C.V. Mosby Company, 1970.

[8] C.J. Evans and R.J. Hockens. Self-calibration: Reversal, redundancy, error separation, and 'absolute testing'. In *Annals of the CIRP Vol. 45/2*, pages 617–634, 1996.

[9] T. Harris. *Rolling Bearing Analysis.* John Wiley and Sons Inc, 1991.

[10] R.J. Hocken, J. Raja, and et. al. Sampling issues in coordinate metrology. *Manufacturing Review, Vol. 6, No. 4*, pages 282–294, December 1993.

[11] R. Kingslake and I. B. Lueck. *Applied Optics and Optical Engineering*, chapter 6. Academic Press, 1965.

[12] B. Kuo. *Automatic Control Systems.* Prentice-Hall, 1995.

[13] T.R Kurfess, D.L. Banks, and et. al. Statistical metrology. In *Proceedings of the 1994 International Mechanical Engineering Congress and Exposition Nov 6-11 1994 v 55-2 1994 Chicago, IL*, pages 961–967, 1994.

[14] S.J. Ludwick, D.C. Ma, and Trumper D.L. In *A Rotary Arm Based Turning Machine for Ophthalmic Lenses.* Accepted for 1998 ASPE Conference.

[15] D. Malacara. *Handbook of Lens Design.* Marcel Dekker, 1994.

[16] A.H. Slocum. *Precision Machine Design.* Prentice Hall, 1992.

[17] R.J. Smith and R.C. Dorf. *Circuits, Devices and Systems.* John Wiley and Sons Inc., 1992.

[18] S.T. Smith and D.G. Chetwynd. *Foundations of Ultraprecision Mechanism Design.* Gordon and Breach Science Publishers, 1992.

[19] W.J. Smith. *Modern Optical Engineering.* McGraw Hill, 1990.

[20] D.C. Thompson and R.R. Donaldson. Design and performance of a small precision cnc turning machine. *Annals of the CIRP, Vol. 35, No. 1*, 1986.

[21] M. Tomizuka. Zero phase error tracking algorithm for digital control. *Journal of Dynamic Systems, Measurement, and Control, Vol. 109*, pages 65–68, 1987.

[22] M. Tomizuka and M.S. Chen. Tool positioning for noncircular cutting with lathe. *Journal of Dynamic Systems, Measurement, and Control, Vol. 109*, pages 176–179, 1987.

[23] M. Weck, H. Ozmeral, and et. al. A new hybrid concept for a long stroke fast-tool-servo system. In *Proceedings of the Annual Meeting of the ASPE*, pages 211–214, 1995.